LAWRENCE
LIVERMORE
NATIONAL
LABORATORY

LLNL-TH-648062

Imaging of Phase Objects using Partially Coherent Illumination

F. L. Ravizza

December 26, 2013

Disclaimer

This document was prepared as an account of work sponsored by an agency of the United States government. Neither the United States government nor Lawrence Livermore National Security, LLC, nor any of their employees makes any warranty, expressed or implied, or assumes any legal liability or responsibility for the accuracy, completeness, or usefulness of any information, apparatus, product, or process disclosed, or represents that its use would not infringe privately owned rights. Reference herein to any specific commercial product, process, or service by trade name, trademark, manufacturer, or otherwise does not necessarily constitute or imply its endorsement, recommendation, or favoring by the United States government or Lawrence Livermore National Security, LLC. The views and opinions of authors expressed herein do not necessarily state or reflect those of the United States government or Lawrence Livermore National Security, LLC, and shall not be used for advertising or product endorsement purposes.

This work performed under the auspices of the U.S. Department of Energy by Lawrence Livermore National Laboratory under Contract DE-AC52-07NA27344.

IMAGING OF PHASE OBJECTS
USING
PARTIALLY COHERENT ILLUMINATION

by

Frank L. Ravizza

Copyright © Frank L. Ravizza 2013

A Thesis Submitted to the Faculty of the

DEPARTMENT OF OPTICAL SCIENCES

In Partial Fulfillment of the Requirements

For the Degree of

MASTER OF SCIENCE

In the Graduate College

THE UNIVERSITY OF ARIZONA

2013

LLNL-TH-648062

STATEMENT BY THE AUTHOR

Disclaimer

This document was prepared as an account of work sponsored by an agency of the United States government. Neither the United States government nor Lawrence Livermore National Security, LLC, nor any of their employees makes any warranty, expressed or implied, or assumes any legal liability or responsibility for the accuracy, completeness, or usefulness of any information, apparatus, product, or process disclosed, or represents that its use would not infringe privately owned rights. Reference herein to any specific commercial product, process, or service by trade name, trademark, manufacturer, or otherwise does not necessarily constitute or imply its endorsement, recommendation, or favoring by the United States government or Lawrence Livermore National Security, LLC. The views and opinions of authors expressed herein do not necessarily state or reflect those of the United States government or Lawrence Livermore National Security, LLC, and shall not be used for advertising or product endorsement purposes.

ACKNOWLEDGEMENTS

This work was performed under the auspices of the U.S. Department of Energy by Lawrence Livermore National Laboratory under Contract DE-AC52-07NA27344.

I wish to acknowledge and thank the following contributors to this work:

Michael Nostrand	James Folta	Paul Wegner
Michael Johnson	Robert Bishop	Laura Kegelmeyer
Marcus Monticelli	John Peterson	Brian Hackel
James Fair	Larry Platz	Timm Wulff
Ruth Hawley	Glenn Larkin	Joshua Senecal
Pamela Whitman	Michael Flegel	Brian Hackel
Daniel Mason	Tom Milster	Naresh Mehta
Selim Elhjad	Chirstopher Stolz	David Hopkins

DEDICATION

This work is dedicated to my parents, Doug and Mallie Ravizza, for gifting me life and opportunity.

TABLE OF CONTENTS

CHAPTER 1. Introduction....10
1.1 Fratricidal Phase Object Screening....11
1.2 Mapping Tool Development....12
1.3 Linescan Phase Differential Imaging....14
1.4 LPDI Phase Object Detection....15
1.5 Modeling and Simulation of LPDI....18
CHAPTER 2. Background....20
2.1 Schlieren Imaging....22
2.2 Phase Contrast Microscope....24
2.3 Hoffman Modulation Contrast Microscope....25
2.4 Differential Inference Contrast Microscope....26
CHAPTER 3. The FPO Screening Process....28
3.1 FICS Screening Process....30
3.2 FOAQual Analysis....31
3.3 FICS Tool....32
3.4 FADLiB Coating Flaw Mapping....37
3.5 LPDI Camera....39
3.6 LPDI Linear Image Sensor....40
3.7 LPDI Motion Control....41
3.8 LPDI Illumination Source....42
3.9 Image Analysis and Hit List Ranking....44
3.10 Phase Shifting Diffraction Interferometry....47
CHAPTER 4. Spatial Coherence and Imaging....51
4.1 The Phasor Describes Light Oscillation....52
4.2 Spatial Coherence and Illumination....53
4.3 Spatial Coherence in Imaging Systems....59
4.4 The Köhler Illumination System....59
4.5 Spatial Coherence of the Köhler Illumination....61
4.6 LPDI and the Köhler System....63
4.7 Purpose of LPDI Image Simulation....64
4.8 LPDI Image Simulation....65
CHAPTER 5. Coherent Image Simulation....67
5.1 Derivation of Physical Optics based Imaging....67
5.2 Coherent Imaging Model....68
5.3 Plane Wave Field....70
5.4 Object Transmittance Function....71
5.5 Field Transmitted through the Object....72
5.6 Imaging as a Spatial Filtering....72
5.7 The Transfer Function....73
5.8 Linear Shift Invariance....74
5.9 Lens Aberrations....75
5.10 Transfer Function Shift....76

5.11 Image Irradiance 77
5.12 Coherent Image Simulation Example 77
CHAPTER 6. Partially Coherent Image Simulation 82
6.1 Partially Coherent Image Irradiance 82
6.2 SVD Speeds Computation 83
6.3 Plane Wave Spatial Frequency Distribution 84
6.4 Polychromatic Plane Wave Distribution 86
6.5 Obtaining the Eigenterms Numerically 88
6.6 LPDI Linescan Blurring 89
CHAPTER 7. LPDI Image Simulation Results 90
7.1 Simulation Inputs 90
7.2 LPDI Image Simulation Parameters 91
7.3 Gaussian Phase Objects 93
7.4 Gaussian Phase Object Imaging Simulation 94
7.5 Gaussian Bump Comparison Discussion 98
7.6 FPO Flaw Set 99
7.7 Measured LPDI Images 103
7.8 Simulated Images 104
7.9 Flaw Set Results Discussion 107
CHAPTER 8. Discussion 109
8.1 Examination of LPDI Eigenterms 109
8.2 Singular LPDI Transfer Function 111
8.3 Heuristic Phase Extraction 112
CHAPTER 9. Conclusion 115
Appendix A Mathematics 116
Appendix B MATLAB™ Code 120
Appendix C Gaussian Bump Fabrication 121
Appendix D First LPDI Image 122
References 123

LIST OF FIGURES

Figure 1.1: LPDI imaging system configuration.....15
Figure 1.2: Illustration of the LPDI phase object detection.....17
Figure 2.1: Diagrams of four types of phase object imaging systems.....21
Figure 2.2: Prototype Schlieren imaging system for phase object screening 24
Figure 3.1: FPO screening process performed by FICS 30
Figure 3.2: Integrated FICS2 system mounted to cleanroom subfloor.....34
Figure 3.3: Photo of FICS2 system integrated around a large travel XY-stage.....35
Figure 3.4: Reverse table showing LPDI and PSDI cameras 36
Figure 3.5: Forward table showing PSDI fibers and LPDI illumination source.....36
Figure 3.6: Photograph of the FICS2 operator console and control software.....37
Figure 3.7: The FADLiB detects sol-gel coating flaws as a reflectance variance 38
Figure 3.8: MTFs of two Rodenstock large format camera lenses used for LPDI 40
Figure 3.9: Photographs and micrographs of the LPDI image sensor.....41
Figure 3.10: Microscope image of the Scott Lightline apertures.....44
Figure 3.11: Microscope image of the Schott Lightline fiber core 44
Figure 3.12: Optics Inspection software displaying analyzed oWFL LPDI image 46
Figure 3.13: Pmax vs. FOAQual failure probability 47
Figure 3.14: Two-fiber PSDI measures the flaw's transmitted amplitude and phase 49
Figure 4.1: The phasor on the complex plane describes wave oscillation.....53
Figure 4.2: Double pinhole interferometer demonstrating spatial coherence.....57
Figure 4.3: Köhler illumination system source and object conjugate planes 61
Figure 4.4: LPDI imaging system model for partially coherent imaging.....66
Figure 5.1: The imaging system model 69
Figure 5.2: Point source and plane wave coordinate axes 70
Figure 5.3: Example coherent imaging system transfer function.....74
Figure 5.4: Fast plane wave, low NA (f/16) yields low contrast dark-field image.....78
Figure 5.5: Fast plane wave, high NA (f/5.6) yields high contrast dark field image 79
Figure 5.6: Slow plane wave, low NA (f/16) yields high contrast bright-field image 79
Figure 5.7: Slow plane wave, high NA (f/5.6) yields low contrast bright-field image 80
Figure 6.1: Continuous and discrete (sampled) plane wave distributions 85
Figure 6.2: Plane wave distributions for three types of power spectrums.....87
Figure 7.1: LPDI map of 2" Gaussian bump test sample showing 8 sites.....93
Figure 7.2: PSDI measured phase Gaussian objects 94
Figure 7.3: Measured LPDI image of Gaussian bumps.....95
Figure 7.4: Simulated LPDI images of Gaussian bumps.....96
Figure 7.5: Gaussian bump line profiles, Measured vs. Simulated.....97
Figure 7.6: P-V opd vs. P_{max} & Ratio for Gaussian bump objects.....99
Figure 7.7: PSDI measured flaw phase (opd) 100
Figure 7.8: Flaw Horizontal (ZX) and Vertical (ZY) OPD Profiles 101
Figure 7.9: Measured flaw images 104
Figure 7.10: Simulated flaw images.....105
Figure 7.11: Horizontal profiles of measured and simulated flaw images 106

Figure 7.12: Flaw P_{max}, Measured vs. Simulated 107
Figure 8.1: First four eigenmatrices of an LPDI system with a rectangular pupil 110
Figure 8.2: First 50 eigenvalues and non-zero part of the eigenmatrices 111
Figure 8.3: Simulated image of Flaw A produced from a single TF 112
Figure 8.4: LPDI image of a Continuous Phase Plate (CPP) 113
Figure 8.5: CPP phase maps as measured by Interferometry (left) and LPDI (right) 114

ABSTRACT

Screening high-power laser optics for light intensifying phase objects that cause laser-induced damage on downstream optics is critical to sustaining laser operation. Identifying such flaws on large-apertures is quite challenging since they are relatively small and invisible to conventional inspection methods. A Linescan Phase Differential Imaging (LPDI) system was developed to rapidly identify these flaws on large-aperture optics within a single full-aperture dark-field image. We describe a two-step production phase object screening process consisting of LPDI mapping and image analysis, followed by high-resolution interferometry and propagation based evaluation of the downstream damage potential of identified flaws. An image simulation code capable of modeling the LPDI partially coherent illumination was used to optimize its phase object sensitivity.

CHAPTER 1. INTRODUCTION

Flaws on optics in high-power laser systems can intensify light on downstream optics and cause laser-induced damage (LID)—a phenomenon termed *fratricide* ("to kill brother") since the flaw in effect damaged a neighboring optic.[1-5] Once initiated, laser damage can grow on subsequent exposure of high-power light until reaching a catastrophic critical dimension that forces replacement of the entire high-cost optical component.[6-8] Therefore, fratricide and subsequent damage growth limit sustainable laser operation and increase operational cost.

Transparent flaws that modulate the phase of the light are a special class of defect called *phase objects*. Phase objects can appear on the surface of optics as microscopic bumps, pits, or coating defects; or in the bulk material as index inhomogeneities. Transparent phase objects have greater probability of causing fratricide than opaque *amplitude objects* because phase objects can concentrate light into a small region, like a lens—whereas amplitude objects tend to scatter light into a large solid angle. However, obscurations can generate sufficient intensification to trigger fratricide via Arago spot or nonlinear imaging.[9, 10]

Although the vast majority of phase objects are benign, they are an especially problematic type of flaw since they are typically invisible to conventional inspection methods because they do not scatter light into a broad direction. Thus, identifying the problematic *fratricidal phase objects* (FPO) among many benign phase objects compounds the difficulty of the inspection challenge. Therefore, specialized imaging

diagnostics are required to inspect optics for phase objects and to determine their fratricide threat.

Once installed in the laser system, FPOs are virtually impossible to identify since in situ damage inspection diagnostics are optimized to detect laser damage, a strong amplitude object.[11, 12] Fratricidal phase objects are particularly insidious when they persist in the beam path, unidentified—continuing to inflict damage on multiple optics. Even if in-situ diagnostics detect a potential FPO, associating it with a damage event (or vice versa) can be ambiguous because LID can also occur due to intrinsic material precursors[13-15] or contaminants[4]. Therefore, it is critical to screen optics for FPOs prior to their installation and use in a high-power laser system.

1.1 Fratricidal Phase Object Screening

Screening for FPOs is especially challenging because the phase objects of interest are small in comparison to the large-optic apertures that contain them. For example, the phase and lateral dimensions of a typical FPO may vary between 50 and 1,000 nm OPD, and 0.05 and 5 mm across. By comparison, the optics undergoing inspection have rather large apertures of 400 x 400 mm^2 and thicknesses varying between 10 and 45 mm. Detection and characterization of such small phase objects within such large optic volumes in high-volume production requires a two-step screening process: 1) low-resolution full-aperture mapping, followed by 2) high-resolution small field-of-view characterization.

Step 1 requires a special imaging system since it must detect phase objects by transforming a phase modulation in the object plane into an irradiance modulation in the

image plane. An image segmentation algorithm then reports potential FPOs detected in the image within a *hit list* map by listing their coordinate on the optic in a standard coordinate system, defined by the edge of the optic or *fiducial* markings outside the clear-aperture. Due to process time constraints, only the detections with the highest probability of causing fratricide are sampled for high-resolution characterization, typically fewer than 100 flaws per inspected optic.

In Step 2, flaws in the hit list are aligned within a 4mm FOV of a high-resolution interferometer that records the transmitted amplitude and phase of the individual flaws, which is then analyzed to determine the pass or fail result of each individual high-resolution flaw image. The pass or fail result of the entire optic is determined by aggregating these individual flaw results, i.e. if one flaw fails, then the entire optic fails. Failing flaws can be reworked to *mitigate* their fratricide threat before installing the optic, either by applying a physical *mitigation* protocol[16-18] to the flaw itself, or by *spot blocking*[19] that location in the laser system before firing a high-power shot.

1.2 Mapping Tool Development

To meet the required FPO screening process throughput for National Ignition Facility (NIF)[20] final optics[21], a new type of imaging system called *Linescan Phase Differential Imaging* (LPDI) was developed in 2007 to perform the phase object mapping required for Step 1. Ravizza et al. introduced this FPO screening process at the SPIE Laser Damage conference in 2009.[22] The LPDI system detects phase objects within a full-aperture image as bright spots against a dark background—a type of image referred to as a *dark-field* since the object signal appears in the image against a dark background.

In general, imaging systems produce dark-field images using an optical spatial filter designed to pass only the light perturbed by objects of interest to the detector, while blocking the background illumination. What is unique about LPDI is it employs an intrinsic spatial filter that is highly sensitive to phase objects created between a linear illumination source aligned off-axis with respect to a linear image sensor. Shifting the illumination source off-axis with respect to the lens and sensor causes the majority of the background illumination to fall outside the numerical aperture (NA) of the imaging lens to produce a dark-field image. Phase objects in the optic however, diffract a significant fraction of the illumination into the lens NA for detection by the linear image sensor. Linescan imaging is necessary to maintain the spatial filtering properties created by the source-sensor alignment—which in effect, applies the same spatial filter across the entire optic aperture, thereby recording an image with uniform phase object sensitivity.

LPDI spatial filtering is "intrinsic" since it is inherent to the source-sensor geometry owing to their mutual linear shapes and relative alignment. Other types of dark-field imaging systems (described in Chapter 2), require additional spatial filtering optical components (e.g. lenses, apertures, filters, masks) to enhance phase object contrast and generate a dark-field image. The intrinsic spatial filtering of LPDI is notable because it greatly simplifies optical system complexity by eliminating optical components that potentially contribute noise. The name *Linescan Phase Differential Imaging*, originates from the observation that the LPDI image signal is proportional to the first derivative of the object's phase in the line-scanning axis.

1.3 Linescan Phase Differential Imaging

The LPDI imaging system as shown in Figure 1.1 consists of three principal components: 1) an off-axis linear light *source*, 2) the *optic* undergoing inspection, mounted to a linear translation stage to execute linescan imaging, and 3) a camera containing a conventional camera *lens* and linear image *sensor*. The camera assembly incorporates a mechanical apparatus to focus the lens on the optic and source, and to align the sensor to the lens image plane and optical axis—such that the linear image sensor is coplanar with the image plane, and bisected by the lens optical axis. The lens optical axis defines the LPDI system z-axis. The long axes of the source and sensor are parallel to the system y-axis. The 1D sensor records a 2D image of the optic using a technique called *linescan imaging* by translating the optic across the camera in synchronization with each linear exposure (*linear frame*), such that a 2D image is constructed from a series of linear frames.

During an LPDI scan, the optic translates along the x-axis at constant speed such that it travels one pixel length (in object space) per linear frame. The illumination source behaves as a linear array of spatially incoherent point sources with infinite extent in the y-axis and point source like extent in the x-axis and emits quasimonochromatic light in the visible spectrum. Source brightness is set such that the peak signal of its blurred spot recorded on the image plane represents 75% of the sensor's exposure saturation when the lens is focused on the object plane.

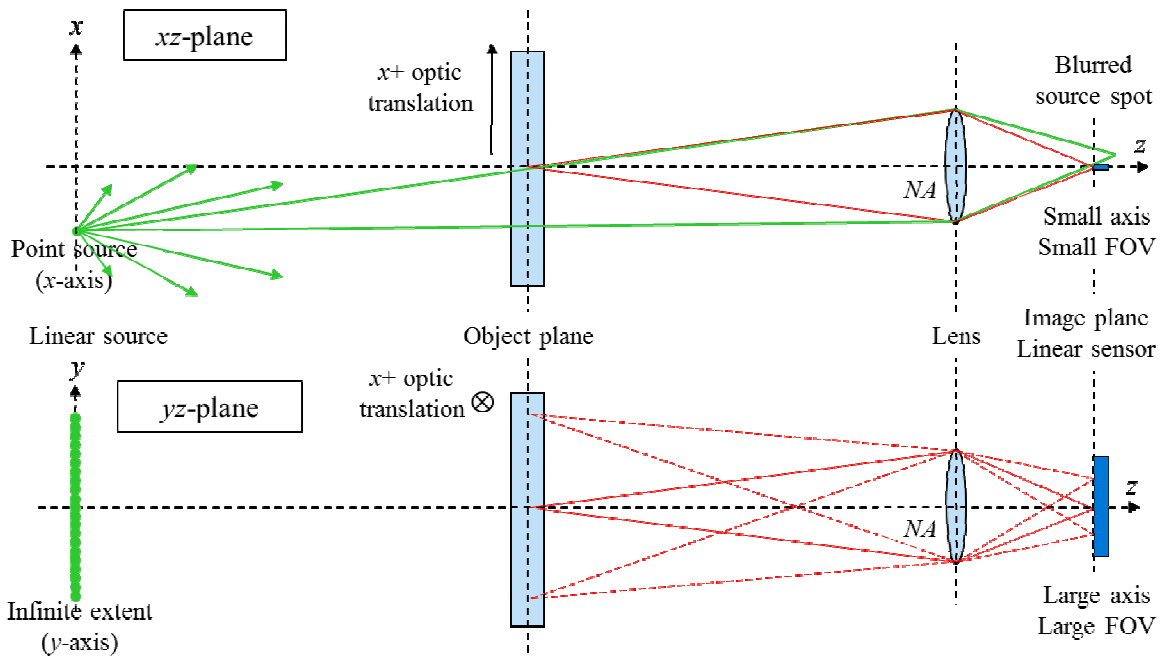

Figure 1.1: LPDI imaging system configuration

The LPDI system from left-to-right, consists of a linear illumination source, illustrated here as a linear array of point sources infinitely long in the *y*-axis, the optic undergoing inspection mounted to a linear translation stage, and a camera containing a lens and linear image sensor. Red rays represent the marginal rays of the lens, while green rays represent light emitted by the point sources, which produces a rectangular blurred spot on the image plane. The NA defines the effective FOV of the camera as governed by the size of the sensor, which is small in the *xy*-plane and large in the *yz*-plane. During linescan imaging, the optic translates vertically in the *xy*-plane and into the page in the *yz*-plane.

1.4 LPDI Phase Object Detection

The alignment of the source relative to the sensor is central to how LPDI detects phase objects. Thus, how LPDI detects phase objects shall be described conceptually in that context. First, consider the LPDI system in Figure 1.1 imaging only air (no object). Imagine the blurred rectangular spot on the image plane produced by the out of focus linear source. Now visualize this rectangular spot shifting across the image plane and the linear sensor as the source is translated along in the *x*-direction. As the blurred spot passes over the sensor, the integrated sensor signal is observed to increase, then decrease.

Now envision positioning the source directly on-axis such that the integrated sensor signal is maximized. This on-axis alignment serves as an explicit reference point from which to shift the source off-axis a fixed repeatable distance. Shifting the source off-axis causes the integrated sensor signal to decrease, since a dimmer region in the spot will lie over the sensor. Now a transparent test optic is inserted in the object plane to scan it for phase objects. Doing so will likely shift the position of the spot due to refraction through the optic, so the source is realigned back to the on-axis condition, defined as 75% of sensor saturation. Now the source is intentionally shifted off-axis such that the integrated sensor signal drops to 5% of saturation. This 5% sensor signal level represents the image background. Each time a new optic is measured the source is realigned according to this criterion.

Illustrated below in Figure 1.2, are two different optics imaged by LPDI. Optic A contains a phase object, specifically a bulk index inhomogeneity, while Optic B is a pristine optic composed of flawless material. After aligning the source off-axis at the 5% background level both optics are imaged as described in Section 1.2, by translating the optic in the *x*-axis (vertical direction in Figure 1.2). When the bulk index inhomogeneity in Optic A arrives to the NA cone of the imaging lens, the phase object will diffract some fraction of light into the lens NA, thereby recording a signal in the image above the 5% background level at the pixels corresponding to that location in the optic. Optic A however, contained pristine material. Therefore, the detector did not receive a signal because a flaw did not diffract any illumination into the lens NA. The image of Optic A instead appears as a constant 5% background level within the clear aperture.

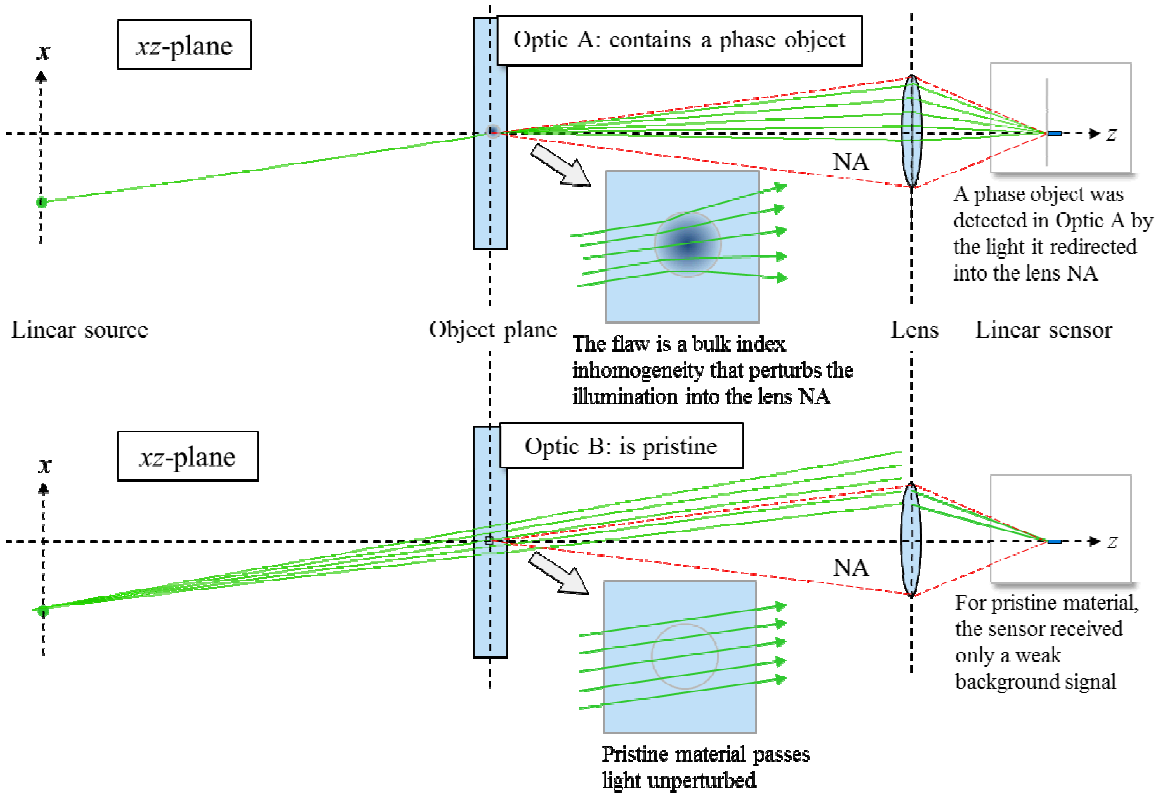

Figure 1.2: Illustration of the LPDI phase object detection

Both views above show the *xz*-plane of an LPDI system imaging two different optics: Optics A (top) contains a phase object, while Optic B (bottom) is flawless. LPDI detected the flaw in Optic A since the flaw perturbed light into the lens NA and onto the image sensor. However, since Optic B was pristine, light simply passed through, most of it falling outside the lens NA. The ray fan appearing to emit from the flaw in Optic A and be collected by the lens illustrates the concept of *NA coupling*. The ray fan emitting from the source in Optic B is broader to illustrate that the sensor received a small background signal (5% of sensor saturation).

To summarize, the LPDI system records a signal when a flaw in the optic diffracts some fraction of the illumination into the camera NA, and *NA coupling* refers to the overlap condition between the solid angles representing the light diffracted by the flaw, and the lens NA. Therefore, an LPDI system is optimized for FPO detection by tuning the imaging parameters governing this NA coupling condition. We note that amplitude objects may also appear in the LPD image, but will have much lower relative signal

compared to phase objects since amplitude objects scatter light into a much larger solid angle, which results in lower NA coupling. Thus, in general, an LPDI system is less sensitive to amplitude objects, and when properly optimized, phase objects are well discriminated from amplitude objects in the image.

Note that the boundaries of the optic will be clearly visible in the LPDI image, since the optic edges represent a very large phase difference. In addition, any out-of-focus structure inherent to the illumination source may be visible in the image background, as will any object motion following errors (e.g. stage oscillations) during linescan imaging that perturb the source-sensor geometry. If these motion errors are significant, they will disrupt their delicate alignment and alter the NA coupling condition for optimal FPO sensitivity. Imaging optics that grossly refract the illumination and change the background signal as they are linescan imaged (e.g. wedged or lens optics), require translating the source parallel to the optic during a scan to maintain the background level at 5% of saturation by tracking the gross refraction of the source.

1.5 Modeling and Simulation of LPDI

The original intent of the linescan imaging method employed by LPDI was to detect phase objects in a bright-field image. However, misalignment of the source during initial testing unexpectedly produced a dark-field image (see first LPDI image in Appendix D). Surprisingly we later discovered that this dark-field imaging mode detected phase objects with superior sensitivity compared to the originally envisioned bright-field configuration. Thus, discovery of LPDI was thanks to a fortunate error. Soon after its discovery, an LPDI system applied to FPO screening was commissioned for production,

but with an incomplete theoretical understanding of how it worked. This would later haunt us in early 2012 when efforts to commission a second production LPDI system were met by considerable difficulty. Despite ostensibly sharing identical components and geometry, the new and old systems measured phase objects with different sensitivities. Thus, these system differences required reconciliation before we could conclude commissioning of the second system. Consequently, a more advanced LPDI imaging model was developed.

In this Thesis, we describe this advanced LPDI imaging system model, developed to simulate its partially coherent illumination to generate simulated images of real phase objects from measured phase maps. We begin with a review of four different types of phase object imaging systems in Chapter 2. In Chapter 3, the production FPO inspection tool will be described. In Chapter 4, we explain the concept of spatial coherence in imaging systems and setup the LPDI model, which is detailed in Chapters 5 and 6. The LPDI image simulation accuracy is then evaluated by comparing simulated images to measured images in Chapter 7. Chapter 8 follows with a discussion of the LPDI simulation.

CHAPTER 2. BACKGROUND

Phase objects are difficult to identify because conventional imaging systems render phase objects with poor contrast. This problem has led to the development of specialized imaging systems that seek to detect and measure phase objects by transforming a phase modulation in the object plane into an irradiance modulation in the image plane that detectors can record. Interferometry is a sub-class of phase object imaging commonly used for quantitative phase measurement of phase objects. However, interferometers generally lack the required spatial sensitivity needed for full-aperture FPO screening, as described in Chapter 1.

Spatial filtering is another phase object imaging technique, which is appropriate for FPO screening because it is possible to image large apertures while achieving the required phase object sensitivity. Spatial filters in imaging systems work by filtering light according to its spatial or angular properties prior to the detector. Spatial filters detect phase objects because amplitude and phase objects perturb light into very different directional distributions. When back illuminated, amplitude objects tend to scatter light into a large solid angle and out of the lens NA, thus they appear as if they attenuated the irradiance on the image plane, hence the term *amplitude object*. Phase objects on the other hand, generally perturb light into a much narrower solid angle. Thus, we can detect phase objects by integrating a spatial filter into an imaging system, designed to pass only light within a narrow spatial distribution characteristic of phase objects. In Chapter 1, LPDI phase object detection was explained using the same spatial filtering concept. Other

types of phase object imaging systems enhance phase object contrast through interference. However, we distinguish these from interferometry because they generally do not yield quantitative phase information about the object.

Many types of phase object imaging systems have been designed to exploit the unique way in which phase objects perturb the spatial distribution of light. In this Chapter, we describe four of these phase object imaging systems. As illustrated below in Figure 2.1, they are the Schlieren Camera, Phase Contrast Microscopy, Contrast Modulation Microscopy, and Differential Interference Contrast microscope. Of them, only the Schlieren Camera is suitable for FPO screening since the other three are designed for microscopy, so they lack the required FOV for full-aperture FPO screening.

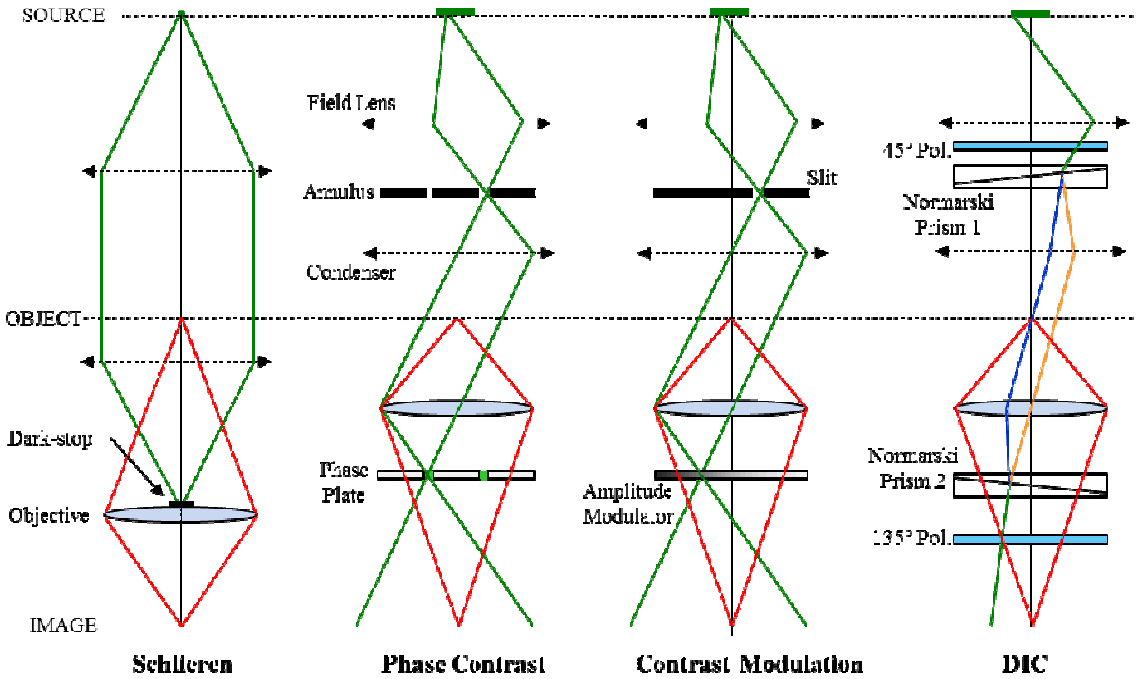

Figure 2.1: Diagrams of four types of phase object imaging systems

Illustrated above are four types of phase object imaging systems. They are, from left-to-right: **Schlieren**, Phase Contrast Microscopy **(PCM)**, Hoffman Contrast Modulation **(HCM)**, and Differential Interference Contrast (**DIC**). All systems contain three common

planes: 1) source, 2) object, and 3) image. Red rays represent the marginal ray path of the objective lens, while green rays represent the illumination light path. In the **Schlieren** system, collimated light transmitted through the object is focused onto an opaque spatial filter "dark-stop" placed near the objective pupil. The dark stop is a spatial filter designed to transmit only light perturbed by flaws in object while blocking background illumination. In **PCM**, an annular illumination field is transmitted through the object and then phase-shifted (+/-90°) by an annular phase plate located near the objective pupil, which phase shifts only the background light, causing it to interfere with light diffracted through phase objects in the sample. **Contrast Modulation** operates on a similar principal to the Schlieren system, but illuminates the object with collimated light from an oblique angle produced by an off-axis slit. An amplitude modulator located near the objective pupil then modulated the amplitude of light transmitted through the object according to its direction as deviated by phase gradients in the object. In **DIC**, a Nomarski prism generates a pair of sheered birefringent images. Since each image passed through a slightly different part in the object, they experience slightly different optical paths lengths. Thus, when recombined by a second Nomarski prism, these two images interfere according to the object's phase gradient, giving phase objects the appearance of 3D structures.

2.1 Schlieren Imaging

Schlieren imaging (or Schlieren photography) is a spatial filtering method invented by German physicist August Toepler in 1864 to study the motion of waves in a fluid using a knife edge spatial filter.[23] Appropriately, its name "Schlieren" is derived from the German word "schliere" meaning streak. A basic Schlieren system back illuminates the object with collimated light. After passing through the sample, this collimated background illumination is spatially filtered by focusing it onto a "dark-stop" located near the camera lens pupil. An opaque disk called a "dark-stop", functions as a high-pass spatial filter by blocking the background illumination while passing light diffracted by phase objects, thus producing a dark-field image. A dark-stop may also pass light scattered by amplitude objects, so phase object discrimination may be unaccepted when imaging optics that also contain amplitude objects. Thus, a band-pass filter

constructed as a transparent annulus that passes light diffracted into a narrow angular distribution may detect phase objects more effectively.

In the Schlieren system, collimated light is generated by placing a point source at the front focal point of a collimating lens. A second lens, called the *spatial filter lens*, focuses this collimated light onto the spatial filter plane. This intermediate focal plane is often referred to as the *Fourier plane* because the spatial filter lens performs an optical Fourier transform of the object by relaying its frequency components onto this plane. Once transformed into frequency space, the object's spatial frequency components are filtered by an amplitude or phase mask. Thus, virtually infinite types of spatial filters are possible in a Schlieren type imaging system.

Schlieren systems do have a few drawbacks. One, the apertures of the collimating and spatial filtering lenses must be as large as the optic to illuminate its entire clear aperture with collimated light. Such lenses are bulky and costly when designed for a full-aperture screening tool. Two, these lenses must also be capable of producing a tight focal spot, which further increases manufacturing cost. Three, these lenses must also be free of defects themselves, since defects on the illumination optics may project themselves (out-of-focus) onto the image plane and contribute noise. Therefore, to screen large-aperture optics for FPOs, costly high-quality lenses are required to image an optic in a single exposure. These drawbacks highlight the advantages of LPDI, since it can mimic the spatial filtering attributes of a Schlieren system, without the use of collimating or spatial filtering lenses. A prototype Schlieren system was constructed for FPO screening in 2007 prior to the development of LPDI. A photograph of this system is in Figure 2.2.

Figure 2.2: Prototype Schlieren imaging system for phase object screening

Photograph showing prototype testing in the NOVA laser switchyard in 2007 of a Schlieren imaging system constructed to screen large aperture optics for phase objects. The system consisted of a pair of 1.2m focal length, 0.8m diameter lenses extracted from the NOVA 1ω output sensor diagnostic. A green point source (right tripod) is produced by a pinhole back illuminated with light delivered by a fiber optic bundle from a halogen lamp and narrow-band filtered at ~550nm. This pinhole source is placed at the front focal point of the first lens to collimate the light between the two lenses, which is where the object is inserted. The second lens focuses the collimated light transmitted through the object onto a dark-stop placed in front of the entrance pupil of a 180 mm focal length camera lens mounted to a 4x5" technical view camera (left tripod). A digital scanning back then records the resulting irradiance pattern on the image plane. These large lenses contained defects that limited phase object sensitivity.

2.2 Phase Contrast Microscope

Dutch physicist Frits Zernike invented the Phase Contrast Microscope (PCM) in 1920 to study living cells.[24-28] Because cells are strong phase objects, they were previously invisible to conventional microscopes unless stained. Staining usually kills the

cell. Therefore, PCM led to the discovery of important biological processes like cell division, which earned Zernike the Nobel Prize in physics in 1953. Phase Contrast Microscopy enhances phase object contrast by illuminating the sample with an off-axis annular illumination field at an oblique angle with respect to the object plane. After passing through the sample, light can do one of three things: 1) continues in the same direction unperturbed as background light, 2) diffract through a phase object in the sample, or 3) scatter through an amplitude object. Zernike's technique enhances phase object contrast by phase shifting the background light by +90° (or -90°) using an annular phase plate located near the objective pupil and shaped to mask only the background light. Phase shifting the background light causes interference between the background light and the light diffracted by phase objects in the sample, thereby enhancing phase object contrast.

2.3 Hoffman Modulation Contrast Microscope

The Hoffman Modulation Contrast microscope was invented by Robert Hoffman in 1975[29]. Like Zernike's Phase Contrast Microscope, the Hoffman Modulation Contrast microscope illuminates the sample with oblique incident light using a linear slit aperture instead of an annulus. An amplitude modulator located near the pupil enhances phase object contrast in the image. The amplitude modulator is constructed as an amplitude mask with linearly varying opacity across the pupil designed to modulate the amplitude of light transmitted through the sample according to its diffracted angle. Phase objects in the sample are thus amplitude modulated, since they diffract the illumination into a steeper or shallower angle, which passes through a different region on the

amplitude mask. Therefore, phase objects in the sample are transformed into a corresponding irradiance modulation in the image plane.

LPDI operates on a similar principal to Hoffman Phase Modulation Contrast. However, instead of an amplitude mask in the pupil to modulate the amplitude of transmitted light according to its diffracted angle. The small NA of the LPDI pupil itself directly modulates the light transmitted through phase gradients in the objects according to its diffracted angle. However, LPDI is able to amplitude modulate phase objects without a complex illumination optical system, which allows it to image very large-aperture optics.

2.4 Differential Inference Contrast Microscope

Georges Nomarski invented the Differential Interference Contrast (DIC) microscope in the 1950s.[30] DIC illuminates the sample with a pair of phase correlated, but orthogonally polarized and spatially separated illumination fields produced by a 45° polarizer and birefringent Nomarski prism, which is a modified Wollaston prism. After transmitting through the object, these orthogonally polarized illumination fields in effect produce a pair of birefringent images displaced (or *sheered*) a distance roughly equal to the spatial resolution of the microscope objective. The birefringent image pair is then recombined spatially and in the same state of polarization using a second Nomarski prism followed by a 135° polarizer. After passing through the second Nomarski prism, the image pair is aligned such that they overlay directly on top of each other. Because the two birefringent light fields passed through slightly different parts in the object, they experience slightly different optical path lengths according to phase gradients in the

object. Thus, these two light fields interfere on the image plane according to their relative phases, thereby enhancing phase object contrast in the resultant image. In DIC, phase objects can appear as three-dimensional objects. In general, DIC renders phase objects with superior contrast compared to PCM. However, DIC has drawbacks since it employs a relatively complex optical system and is most effective on phase objects with relatively small phase gradients.

CHAPTER 3. THE FPO SCREENING PROCESS

The production FPO screening process requires a team of highly trained technicians, using an integrated set of custom hardware and software, executing a sequence of optimized procedures. The screening tool itself is called the Flaw Identification and Characterization System (FICS), and is sited within the Optics Processing Facility (OPF), a class 100 cleanroom located in a separate building near the NIF. The OPF processes new and *recycled* optics in high-volume (up to 60 per week) by cleaning and coating their surfaces with an anti-reflective sol-gel film, and by applying a chemical treatment to the final two fused silica NIF optics in each beamline to enhance their surface damage resistance since they are exposed to the most harmful 351 nm light. Since FPOs can originate during many phases of an optic's life, including during manufacturing at the vendor, during OPF processing, and even while in use on the laser itself—all final KDP and fused silica NIF optics are screened for FPOs by FICS prior to their installation in the beamline. During manufacturing, FPOs can be created by impurities in the material by forming bulk index inhomogeneities[31], or during surface finishing (polishing or KDP diamond turning) by introducing surface bumps or pits. In the OPF, FPOs can develop on the surface during chemical processing or AR coating.[1, 18] On the NIF laser, FPOs can be generated as shallow pits created by laser ablation of particulate surface contaminants.[32]

Following the initial installation of optics in the NIF in early 2010, approximately 80% of the optics screened by the FICS have been *recycled*. The optics recycling process

removes damaged optics from the beamline for *mitigation* prior to the damage site reaching a catastrophic dimension that forces replacement of the entire optic. Optics are removed from the beamline when the size of its largest damage site approaches ~0.5 mm across as interfered by scattered edge light collected by an in situ damage inspection camera called the Final Optic Damage Inspection system (FODI).[12] Recycling an optic involves cleaning, recoating, and FPO screening, followed by application of mitigation protocols in the Optics Mitigation Facility (OMF)[33] to damage sites between 0.05 and 0.800 mm in diameter, and any potential FPOs identified by FICS. The intent of the damage mitigation protocol is to arrest the growth of LID by ablating away damaged fused silica material using a series of tightly focused carbon dioxide laser spots. Mitigation replaces the light absorbing damaged material responsible for growth, with a benign conical surface pit called a Rapid Ablation Mitigation (RAM) cone. The shape of the RAM cone is engineered to avoid causing fratricide itself. Since each cone obscures only a small fraction of the NIF beam (<0.0025% per 2 mm diameter RAM cone) the introduction of a few hundred RAM cones per optic has minimal impact on laser performance. Any downsides posed by RAM cones are outweighed greatly by the benefits of the Recycle loop process since it permits the NIF to sustain high-power operation while reducing operation cost by extending the lifetime of optics. Consequently, when combined with FODI, OPF, and OMF—the FPO screening process is an essential part of the optics recycle loop.

3.1 FICS Screening Process

The Flaw Inspection and Characterization System (FICS) tool performs the two-step screening process described in Chapter 1 using a complementary set of three imaging diagnostics:

1) Linescan Phase Differential Imaging (LPDI): a phase object image-mapping tool sensitive across a broad class of phase objects

3) The Full Aperture Diffuse Light Box (FADLiB): another image-mapping tool that supplements LPDI by detecting sol-gel coating flaws

2) The Phase Shifting Diffraction Interferometer (PSDI): an interferometer used to characterize the flaws identified by LPDI and FADLiB in transmission

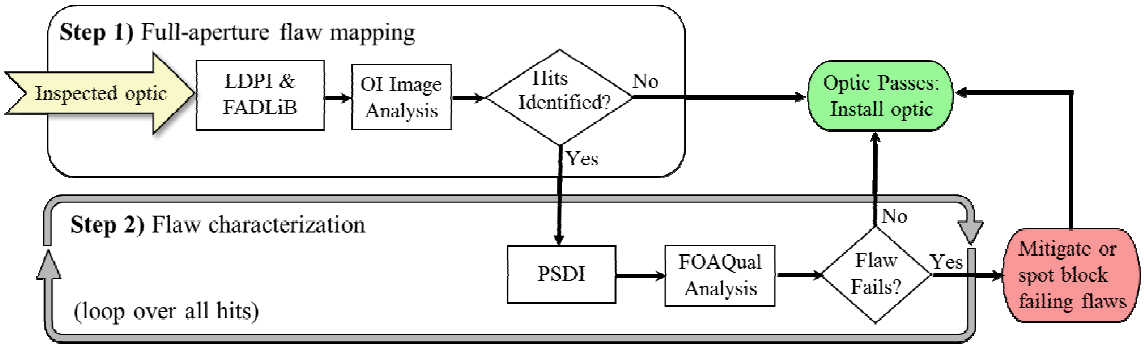

Figure 3.1: FPO screening process performed by FICS

In Step 1, the LPDI and FADLiB images are uploaded to a database through a custom website called LoCoS (Location Components and State) for image analysis by the Optics Inspection software (OI). The OI software reports image analysis metrics of individual defects identified in the image to a database. The metrics rank order the worst defects for characterization in Step 2.

In Step 2, the LPDI and FADLiB hit list coordinates are downloaded from the database and loaded into the FICS control software. A large-travel stage drives each flaw on the optic to within the FOV of the PSDI camera. The PSDI is an interferometer that measures the amplitude and phase of each flaw on a 12.3 x 12.3 mm^2 CCD located ~200mm downstream of the optic. The amplitude and phase on the CCD is then focused by numerically propagating the field back to the optic using a custom software called LiteProp. LiteProp outputs the focused amplitude and phase maps for analysis by another propagation code called FOAQual (Final Optics Assembly: Qualification), which models the fratricide potential of each flaw map within the NIF optical system.[34, 35] The FOAQual software automatically reports any flaw on the optic that failed analysis to the database through LoCoS. Production managers then assign the appropriate corrective action to each failing flaw via the LoCoS web interface. Most failing flaws are mitigated by a RAM cone (the preferred corrective action)—otherwise they are *spot blocked* in the laser beam according to their coordinate on the optic.

3.2 FOAQual Analysis

The FOAQual propagation based flaw analysis code, created by Naresh Metha and Michael Nostrand, is based on the Prop92[34] non-linear laser propagation code that incorporates nonlinearity optical effects (second/third harmonic generation, self-focusing, and non-linear imaging, etc.) to produce downstream fluence (J/cm^2) and irradiance maps (W/cm^2) from which two damageability metrics are calculated. The first metric is the surface damage initiation density $\langle N \rangle_{max}$, and the second is the peak-irradiance in the bulk material I_{pk}, used to predict self-focusing induced bulk *filamentation* damage.[36,

37] These two damageability metrics are assigned failure thresholds for each downstream optic.

The metric $\langle N \rangle_{max}$ represents the expected number of down-stream initiated surface damage sites based on the propagated fluence and a measured probability density function (PDF) that characterizes the surface damage initiation density as a function of laser fluence for that particular surface when exposed to a specific laser wavelength and pulse shape, e.g. 351nm and 3ns FWHM Gaussian.[14] Arbitrary laser pulse shapes (*shaped pulses)* are time-sliced into square (*flat-in-time*) pulses and then scaled to the Gaussian equivalent pulse duration that was used to measure the damage initiation PDF.[38, 39]

An example shaped pulse is the *ignition pulse* used to implode the deuterium-tritium capsule by inertial confinement fusion.[40] The ignition pulse is ~20ns long, has a low power initial *foot*, and concludes with a high peak power pulse of 500 TW delivered from 192 beams. Failure thresholds at each optic surface are *tuned* empirically based on documented fratricide damage events that occurred during laser shots. Flaws that fail FOAQual are spot blocked parametrically depending on the damage potential of the requested shot. [19, 41]

3.3 FICS Tool

The FICS system, shown below in Figure 3.2, incorporates a precision motion control system with a large-travel XY-stage (~1200 mm x ~600 mm) used to align the optic to the LPDI and FADLiB cameras and the individual flaws on the optic to the PSDI camera. On either side of the XY-stage are two optical breadboards, on which the

diagnostic instruments are located relative to the stage to millimeter precision. The forward breadboard contains the PSDI fiber-pair launcher and the LPDI light source mounted to an *x*-axis linear stage. The LPDI and PSDI cameras mount to the reverse table located on the opposite side of the XY-stage. The FADLiB camera and light-box mount to a separate dedicated pedestal. The XY-stage, FADLiB camera pedestal, and the forward and reverse tables bolt to a 25 mm thick steel plate at cleanroom floor level. The steel plate is covered by a stainless steel skin and bolted to a strong steel *weldment* structurally engineered to withstand seismic loading while anchored to the concrete subfloor. The mechanical engineering of FICS was performed at LLNL by a team led by Daniel Mason. A transparent isometric view of the complete second FICS2 system commissioned in 2012 is in Figure 3.2, and photos are in Figure 3.3, 3.4, 3.5, and 3.6.

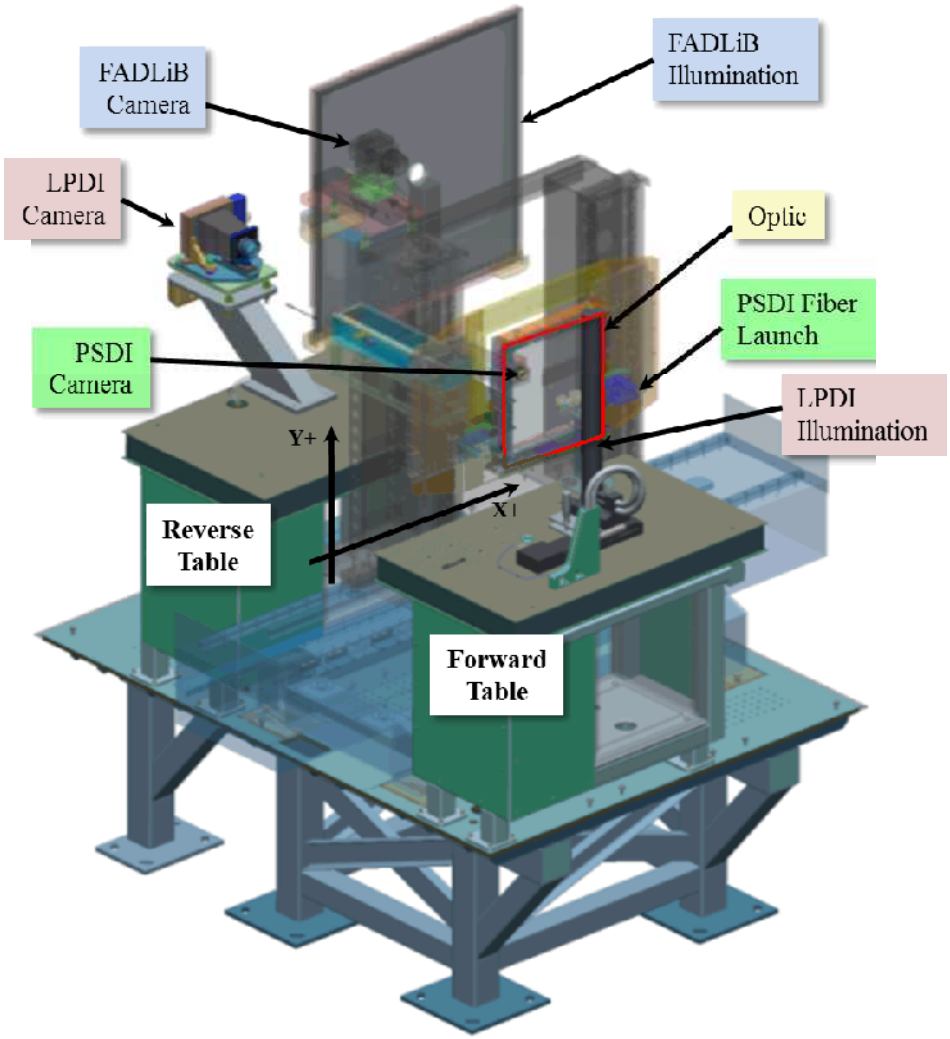

Figure 3.2: Integrated FICS2 system mounted to cleanroom subfloor

Engineering model of the integrated FICS2 system mounted to the seismically secure weldment anchored to the cleanroom subfloor. The optic undergoing inspection mounts to the motion carriage of a large travel XY-stages that straddles the forward and reverse tables, which contain the FICS imaging diagnostics.

The operator interfaces to the FICS hardware using a supervisory control software located at a work console a safe distance from the motion stages, see Figure 3.6. The FICS2 control software was created at LLNL by a team led by Michael Flegel using National Instruments Corporation LabVIEW™. The PSDI camera is mounted to a *z*-stage

with 300 mm of travel used to position the PSDI CCD to ~200 mm from the near surface of the optic. The PSDI fibers are fixed to the forward table. The LPDI sensor is fixed and the camera is focused by translating the lens between the optic plane and sensor. The FADLiB camera is mounted to its own *z*-stage to set focus.

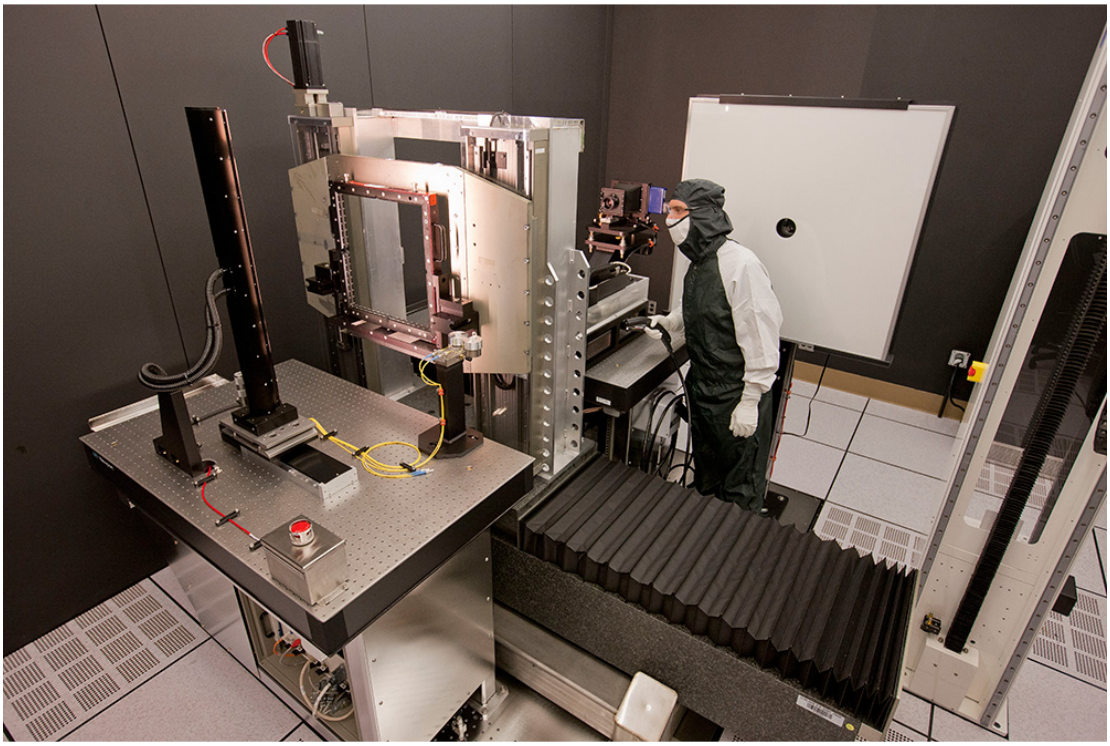

Figure 3.3: Photo of FICS2 system integrated around a large travel XY-stage

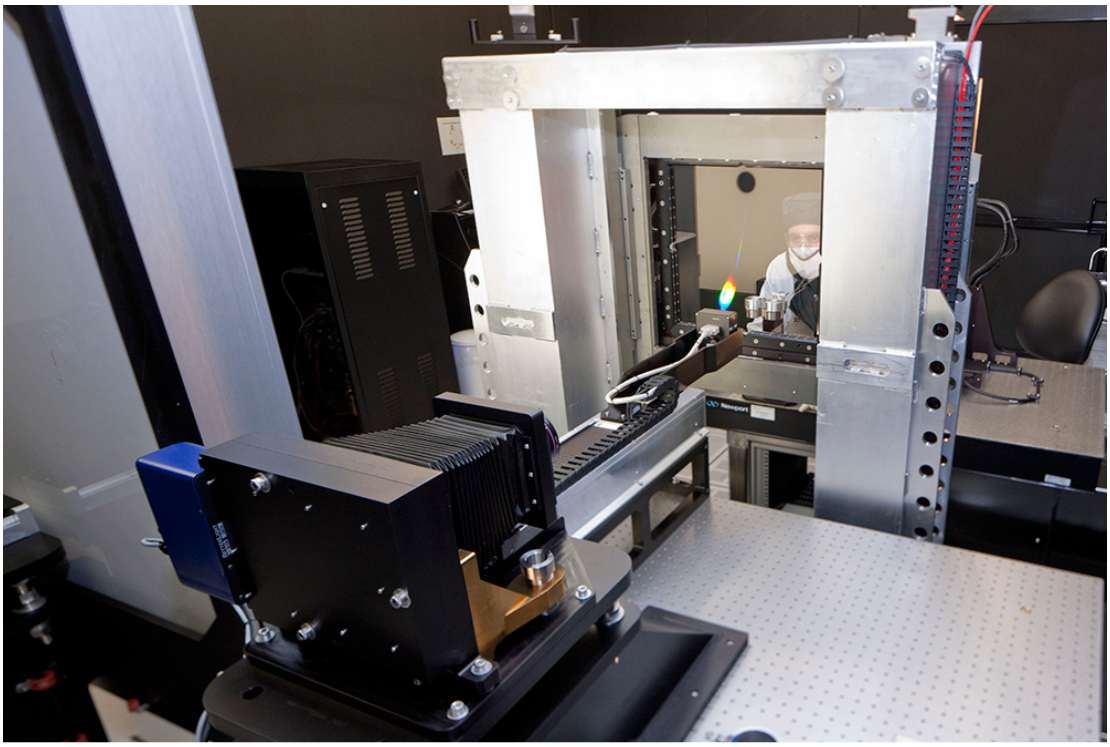

Figure 3.4: Reverse table showing LPDI and PSDI cameras

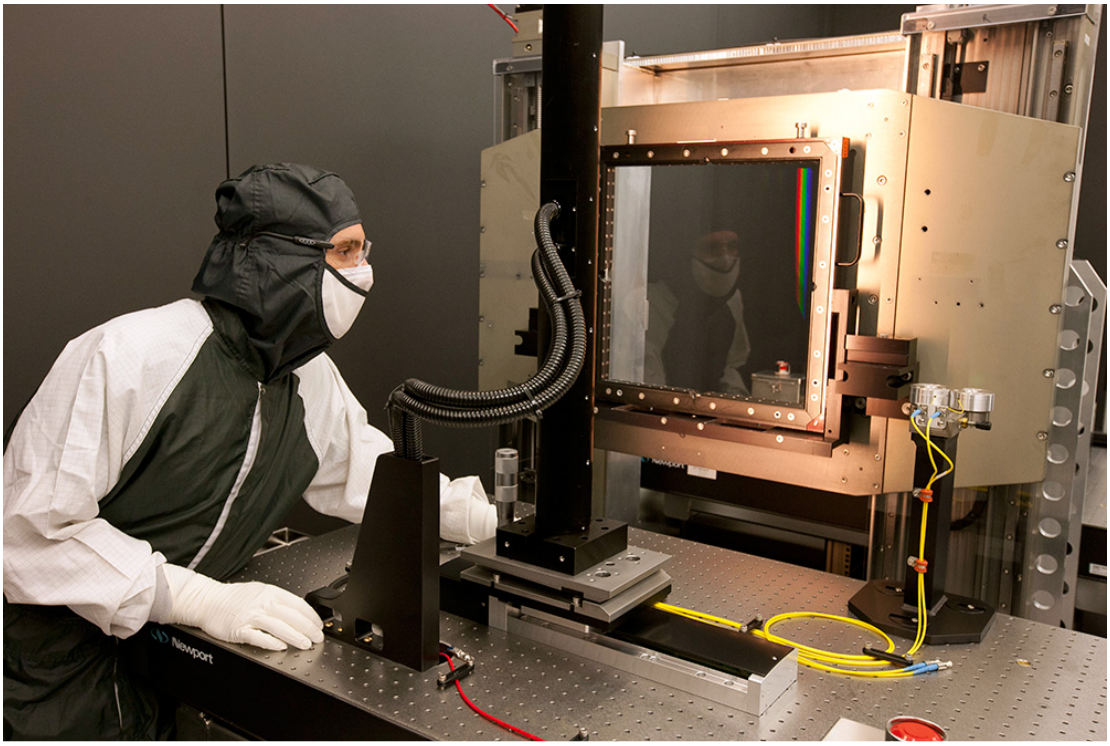

Figure 3.5: Forward table showing PSDI fibers and LPDI illumination source

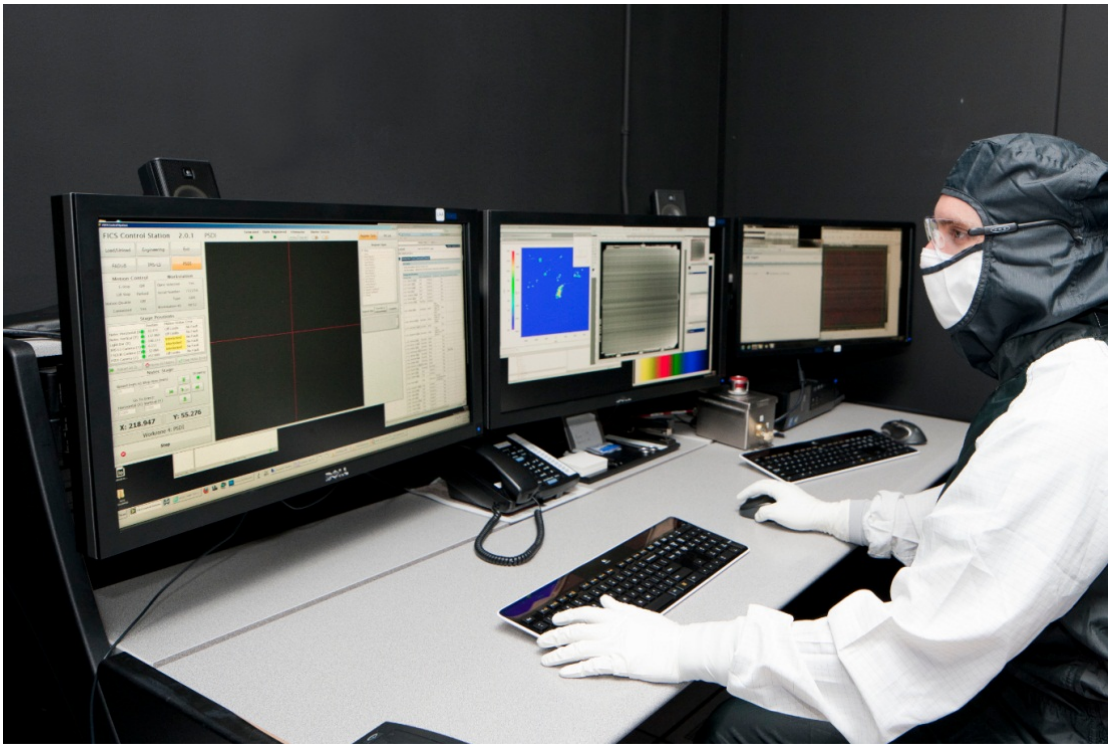

Figure 3.6: Photograph of the FICS2 operator console and control software

The left monitor shows the FICS control system LabVIEW™ software displaying the PSDI CCD used for flaw alignment. The center monitor shows the PSDI processing code LiteProp and an LDPI image of an oWFL. The far right monitor shows the OI software displaying an analyzed LPDI image.

3.4 FADLiB Coating Flaw Mapping

The Full Aperture Diffuse Light Box (FADLiB) was developed by Michael Nostrand and is a supplemental imaging diagnostic optimized to detect sol-gel coating flaws using a large diffuse white light box coaxially mounted to a standard photographic camera that front illuminates the optic, as in Figure 3.7. The FADLiB detects coating flaws as a localized change in Fresnel reflectance of the diffuse white front illumination. Since coating flaws are a build-up of sol gel coating around a precursory defect that was present during spin- or dip-coating of the sol-gel, they cause a localization reflectance

variance that is visible as a contrast variation in imaged optic surface. Both near and far surface are imaged in a single exposure. These coating flaws appear as halos in the FADLiB image and are detected by OI using a dedicated image analysis algorithm. Coating flaws are a common potential FPO so they require screening by FICS. The FADLiB mapping is necessary since LPDI cannot reliably detect all coating flaws that fail FOAQual. Some coating flaws that fail FOAQual can be removed using the Flaw Removal Tool integrated into the FICS1 system, by dispensing decane solvent on the flaw using a syringe followed by sucking away the dissolved sol with a coaxially mounted vacuum nozzle.[18]

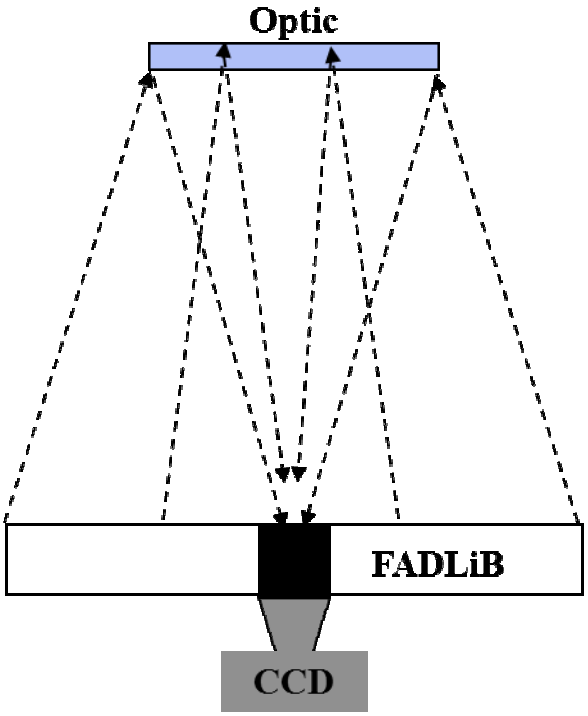

Figure 3.7: The FADLiB detects sol-gel coating flaws as a reflectance variance

3.5 LPDI Camera

The LPDI camera parameters are listed below in Table 3.1. They consist of the camera lens focal length, sensor pixel size, depth of focus, object space FOV, and system overall length. The largest aperture optic that FICS screens is the Target Chamber Vacuum Windows (TCVW). The TCVW is 440x450 mm^2 x 45mm thick fused silica window and dictates the required camera FOV and depth of field to resolve flaws on both surfaces in a single exposure. The LDPI camera lens must detect phase objects ~100µm in lateral size. Thus, the lens and sensor were selected based on that resolvability criteria. The FICS space could accommodate a maximum of 2.5m of overall LPDI system length. Based on these specifications, camera parameters such as depth of focus (F-number), image sensor size, lens magnification and focal length can be determined using first-order optics.[42]

Table 3.1: LPDI Imaging System Camera Parameters

Parameter	**Value / Calculation**
Object space Full FOV	450 mm
Linear sensor	72 mm, 8000 x 9µm pixels
Magnification	450 mm / 72 mm = 0.16
System overall length	<2500 mm
Focal length	210 mm
Lens performance	Detect ~0.1 mm phase object
Depth of field and f#	45mm thick object, f/16

Lens aberrations and diffraction determine the lens spot size and object resolving capability. The highest performance commercially available lens with a FOV compatible with a 72mm format linear sensor is the Rodenstock HR Digaron-S 180mm f/5.6, which has an 80mm image space FOV, large enough for the 72mm long linear image sensor.

This lens is advertised to have 50% MTF contrast at 80 lp/mm (12.5µm period) at f/5.6 across the field and is diffraction limited at f/8. This lens was tested in an LPDI system and demonstrated superior phase object resolution, even at f/16 compared to the Rodenstock Apo-Sironar-S 210mm f/5.6. However, the lower resolution Apo-Sironar-S was used in the FICS2 system because it had a large history of image data statistics since it was used in the original FICS1 system and was deemed to have adequate performance. The Apo-Sironar-S is a 6 element lens of the type Plasmat patented by Paul Rudolph in 1918[43]. MTF data for both lenses are shown below in Figure 3.8. Field dependent aberrations are apparent at the edge of the FOV, even at f/16.

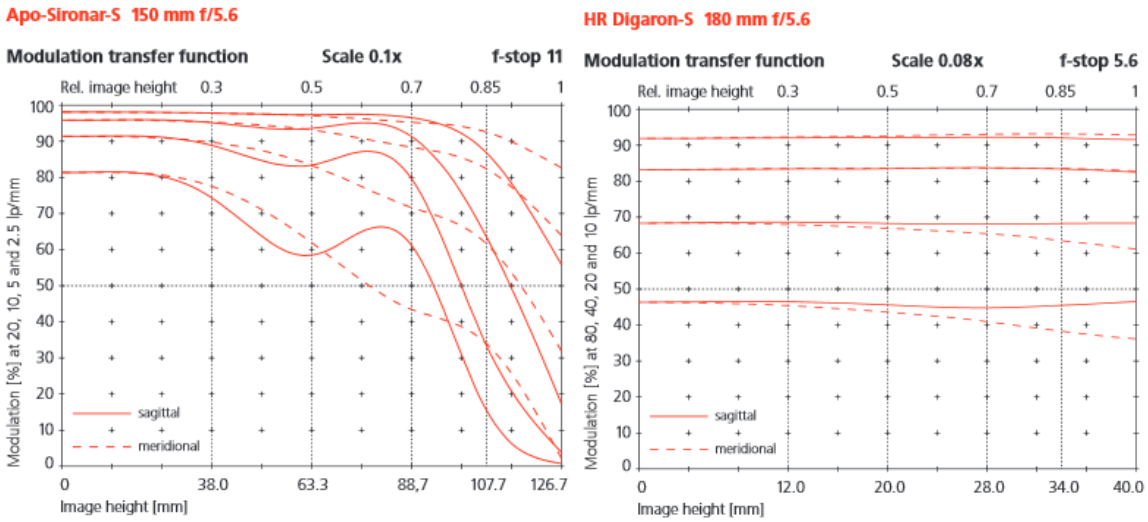

Figure 3.8: MTFs of two Rodenstock large format camera lenses used for LPDI

Lens manufacture provided MTF shows the relative performance of the two lenses tested in the LPDI system.

3.6 LPDI Linear Image Sensor

The LPDI image sensor is model KLI-8023 by Kodak (now TrueSense). The KLI-8023 is trilinear (3x8000 pixels) image sensor for color (RGB) imaging[44]. Better Light, Inc., located in Placerville, CA offers digital scanning back for large format view

cameras using the KLI-8083 in model Super8k-HS[45]. Photographs and micrographs of the RBG and monochromatic versions of this sensor are in Figure 3.9. In the LPDI system, the central green channel in the linear array of pixels in the RGB array effectively records a narrowband spectrally filtered image. The green channel filters the white light emitted by the halogen lamp into a roughly Gaussian spectral distribution, ~70nm FWHM.[46] A monochromatic (unfiltered) version of the BetterLight Super8k-HS using the monochromatic KLI-8083 with broad spectral response in the visible was accidentally installed in the LPDI camera. This monochromatic sensor had poor FPO detection performance. The reason a monochrome sensor has lower phase object contrast will be explained in Chapter 6.

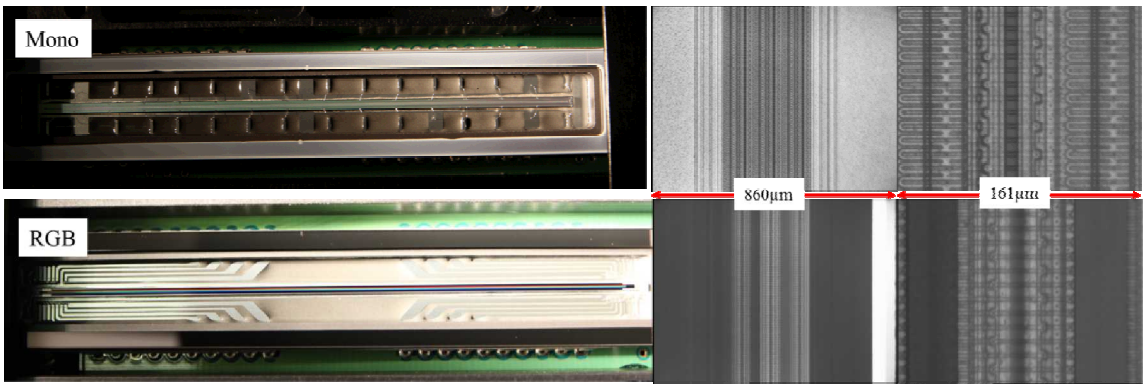

Figure 3.9: Photographs and micrographs of the LPDI image sensor

Photographs and micrographs of the monochromatic (top) and RGB (bottom) versions of the TrueSensor KLI-8023 image sensors. The micrograph of the RGB device appears blurrier than the device in the monochromatic version because of the additional RGB optical filter placed in front of the active region in the CCD.

3.7 LPDI Motion Control

To image optics with variable thickness (e.g. lenses, wedges), a minimum of two closed-loop motion axes are required: 1) a stage to translate the object through the illumination field and, 2) a stage to translate the linear source during linescan imaging to

track the refraction of the illumination source. Tracking of the gross refraction caused by the gross refraction in the object variable thickness effectively removes the gross background phase gradient from the LPDI image caused by the variable thickness object.

The variable thickness optic that FICS frequently screens is the off-axis Wedge Focus Lens (oWFL). The oWFL is an asphere lens with a focal length of ~8m and effective wedge angle of 4.5° that focuses 3ω light onto the target. The oWFL's off-axis asphere produces an effective wedge that is designed to disperse residual unconverted 1ω and 2ω light away from the target. Refraction tracking coefficients for the oWFL are generated by measuring the light source stage position when the source is aligned on-axis (described in Section 1.3) in several locations across the oWFL aperture. These points are then fit by a second-order polynomial. Fit coefficients are then input into the stage programmable logic controller to execute closed-loop parabolic motion tracking between the optic scanning stage and the light source with the light source position acting as a slave to optic position.

3.8 LPDI Illumination Source

The LPDI linear illumination source is a Schott Lightline fiber optic bundle illuminator.[47] The Schott Lightline consists of a bundle of multimode optical fibers dispersed into a narrow channel (~800mm x ~0.4mm). White light is coupled into a 32" long Schott Lightline generated by a halogen lamp (Schott DCRIII[48]). The width of the fiber distribution has been shown empirically to strongly influence FPO sensitivity. Generally, a narrower fiber distribution has superior phase object sensitivity and better

correction between the LPDI image analysis metric P_{max} and FOAQual failure probability, see Figure 3.13.

Images of the two types of Schott Lightlines are shown in Figure 3.10. These images were used to measure the fiber distribution width and their individual core diameters, see Figure 3.11. These measured values were used as parameters in the LPDI image simulation code, described in Chapter 6. The micrographs in Figure 3.10 show the fibers to be randomly distribution and vary in light output. This random variation in light output results in visible horizontal streaking in the image background. However, there is no indication that this random variation in fiber output affects the phase object signal. The FICS1 system employs a 32” linear source by connecting two 16” Lightlines. The two separate Lightlines are visible in FICS1 LPDI image background as a region of discontinuity split in the horizontal direction. Despite the visible discontinuity in the image background, there is no discernable difference in FPO sensitivity across the two regions, because the two lightlines are aligned sufficiently parallel. However, to eliminate this region of possible discontinuity and simplify the mechanical system needed to align to separate 16” Linelines parallel, the FICS2 system employs a single continuous 32” Lineline.

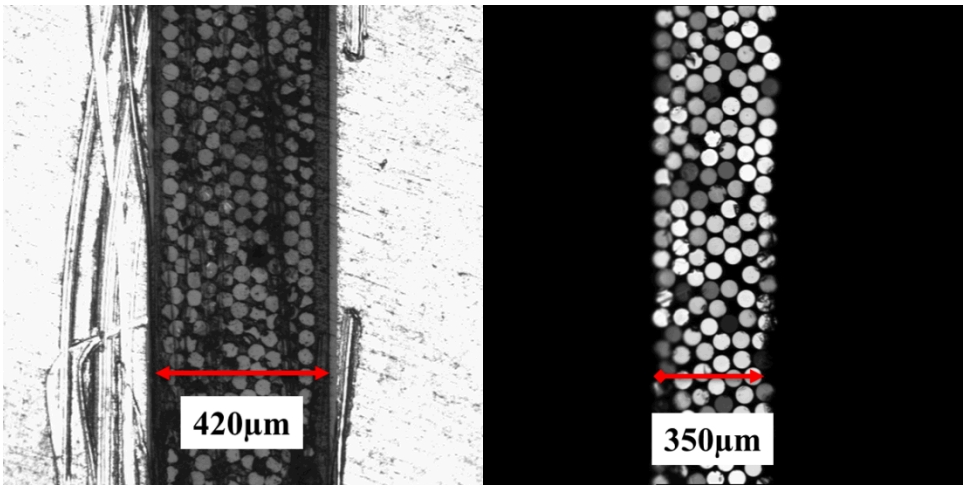

Figure 3.10: Microscope image of the Scott Lightline apertures

Micrograph image of 16" Lightline (left) illuminated by the microscopes built-in coax light. The aperture width of the 16" Lightline was measured to be 420µm. The right image is a micrograph of the 32" Lightlight with fibers emitting light coupled from a Schott DCRIII, and shows its distribution width as 350µm.

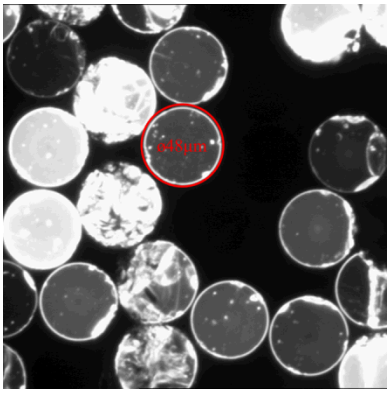

Figure 3.11: Microscope image of the Schott Lightline fiber core

Cladding diameter of the multimode optical fiber was measured as 48µm.

3.9 Image Analysis and Hit List Ranking

Defects identified in the image are assigned a serialized *Defect Name ID* (DNI) so each flaw can be individually tracked in FICS, in OMF, and in the beam line by FODI, over the entire lifetime of the optic. The LPDI image is analyzed by a Local Area Signal to Noise Ratio (LASNR) image segmentation algorithm developed by Laura

Kegelmeyer[49]. This algorithm is integrated into image analysis software called Optics Inspection (OI), which has a GUI that overlays the location of each identified Defect in the image. A screen-shot of an LPDI image of an oWFL analyzed by OI is shown in Figure 3.12. A pattern of *fiducial* markings burned into the corners of the optic using a tightly focused CO2-laser outside the optic clear aperture serves as a coordinate system reference. A pattern recognition algorithm optimized by Joshua Senecal locates these markings in the LPDI and FADLiB images.

The operator must manually detect some types of *low spatial frequency* FPOs in the LPDI. These low frequency phase objects are visible in the LPDI image as a low-contrast change to the background illumination. Due to the low contrast of these objects, the LASNR algorithm used by OI fails to detect them, thus manual detection by human eye is required. The most common type of low spatial frequency phase object appearing on oWFL optics are introduced to the optic surface following hydrofluoric acid etching, using the *acid mitigation process*[50] (AMP). The mechanisms responsible for the generation of low-frequency AMP phase objects are unknown, but it is conceivable they are caused by a differential etch rate, possibly driven by regions of residual stress in the silica material, chemical impurities, or other compositional heterogeneities.

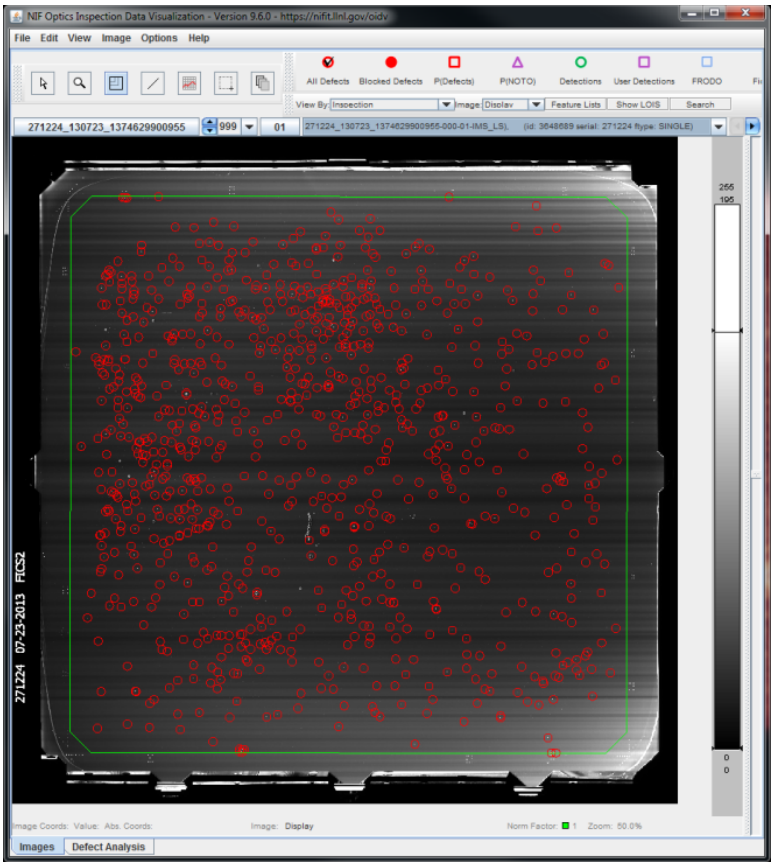

Figure 3.12: Optics Inspection software displaying analyzed oWFL LPDI image

In addition to the Defect's coordinates, OI also reports image analysis metrics. The most important of these is P_{max}, which is the maximum pixel value of the detection in the LPDI image. The OI software reports Defects in an image database. These *hit list* values are downloaded and rank ordered by P_{max}, from largest to smallest P_{max} value. The P_{max} metric correlates best with FOAQual failure probability. The correlation between P_{max} and FOAQual failure probability is shown in Figure 3.13. Defects in the hit list represent potential FPOs that require characterization by PSDI and FOAQual. This characterization step is time consuming. Therefore, the number of Defects for PSDI measurement is reduced by imposing a P_{max} noise floor value at less than 2700 for FICS1

(1900 for FICS2), since defects at this value have a near zero failure probability and therefore do not require PSDI characterization. The hit list length is capped at 96 defects for oWFL, and 48 defects for GDS. Additional PSDI data can be captured if the flaw set indicates inadequate PSDI sampling, i.e. failing flaw at high rank.

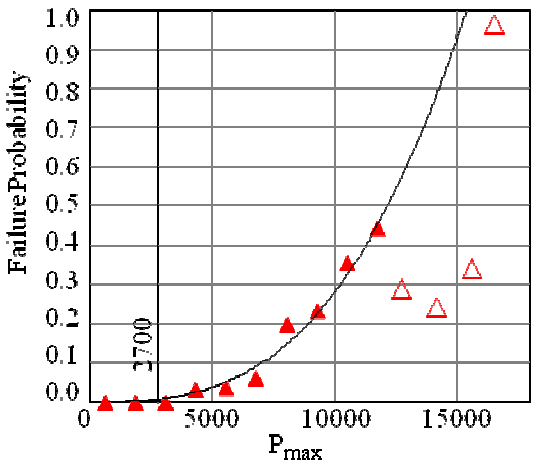

Figure 3.13: Pmax vs. FOAQual failure probability

The OI image analysis metric P_{max} (maximum detection pixel value) vs. FOAQual failure probably shows monotonically increasing failure probability as a function of P_{max}. Open triangles represent data bins with poor sampling—these points did not participate in the power fit. LPDI image hit lists are filtered by a Pmax threshold set empirically based on this data at 2700—this P_{max} value represents the LPDI FPO noise floor.

3.10 Phase Shifting Diffraction Interferometry

The amplitude and phase of the flaws identified in the LPDI and FADLiB images are measured in transmission using a unique two-fiber configuration of the phase shifting diffraction interferometer (PSDI).[51, 52] This two-fiber configuration of PSDI was developed at LLNL by Michael Johnson for the FICS application using PSDI technology capable of 100 pm surface figure accuracy on Extreme Ultraviolet Lithography mirror substrates[53]. However, within the noisy OPF cleanroom environment, the two-fiber

PSDI system is capable of measuring the phase of flaws to an accuracy of ~3nm OPD. The two-fiber PSDI has a FOV at the object plane of ~4 mm and achieves ~10 μm spatial resolution. The spatial resolution of the two-fiber PSDI is determined by the numerical aperture of the CCD, as defined by its lateral dimensions and distance to the object.

The two-fiber PSDI as configured in Figure 3.14 uses a pair of single-mode optical fibers horizontally separated by ~4mm to launch a *reference* and *measurement* spherical wavefront through the optic. The measurement and reference waves transmit through the optic and interfere ~300mm downstream on a bare CCD sensor. Their interference is visible on the CCD as vertical fringes. Flaws identified on the optic are aligned to the CCD with respect to the measurement fiber such that the flaw's diffracted shadow (visible as diffraction rings) is roughly centered in the CCD image. The reference fiber also generates a second shadow on the CCD but is horizontally offset from the measurement shadow to prevent the flaw diffraction rings from overlapping. The fiber-pair must be separated enough so that the two diffracted shadows do not overlap, yet not so far apart that the vertical fringe frequency approaches the CCD sensor Nyquist frequency.

The separation of the two shadows is important for another reason. Since the reference wavefront transmits through an adjacent pristine region in the optic, it interferes with the measurement wave on the CCD, which records an interference pattern of the wavefront diffracted through the flaw from which we can extract the flaw's amplitude and phase using the common principal of direct phase measurement. The PSDI uses a twelve bucket phase-shifting algorithm (3π total phase-shift of the reference wave) and

custom software called Lick (named after the Lick observatory) developed by Don Phillion.[54] In post-processing, piston, focus, and a large tilt term (the vertical fringes) are removed to result in the recovered raw amplitude and phase of the light diffracted through the flaw. However, note this flaw will be out of focus.

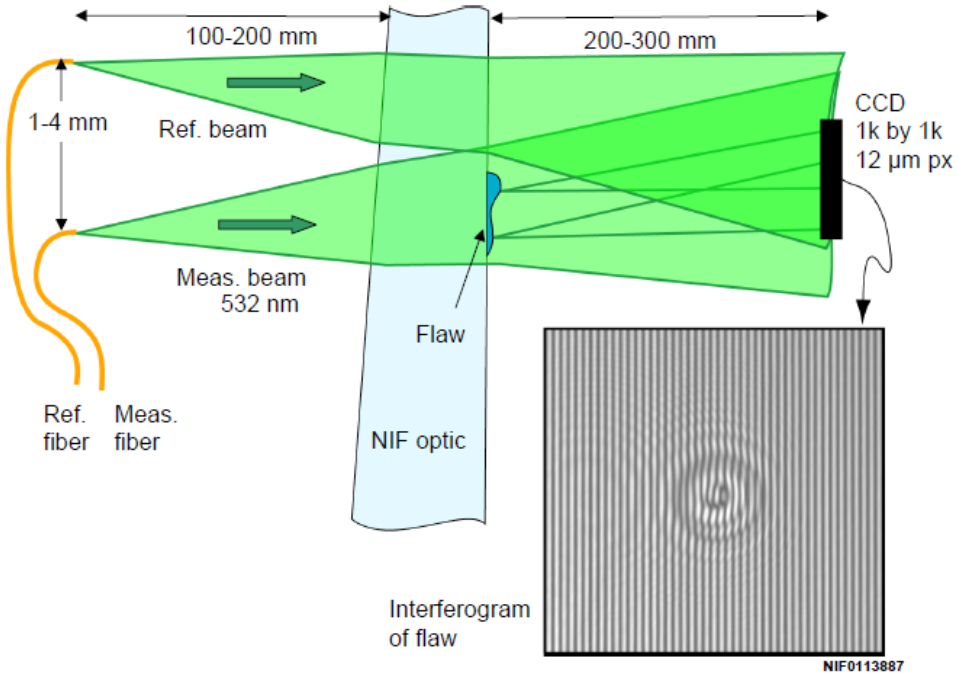

Figure 3.14: Two-fiber PSDI measures the flaw's transmitted amplitude and phase

Next, the amplitude and phase of the each flaw are loaded into a PSDI post-processing code created Michael Johnson called *LiteProp*, written in WaveMetrics, Inc. IGOR Pro™, which focuses each out-of-focus flaw in an automated batch mode. The LiteProp software outputs the PSDI images for damageability modeling by FOAQual. In the first post-processing step, a spatial filter removes the background fringes that *printed-through*. In the second step, the optical field of the flaw is constructed from the measured amplitude and phase extracted from the interferograms recorded by Lick so it can be

auto-focused by numerically propagating it back to the optic surface. The LiteProp autofocus algorithm in action resembles racking the focus of a virtual microscope. Finally, a small subsection of each focused flaw's amplitude and phase (typically 1.4mm FOV) is saved to disk in separate auxiliary files (AUX files) that can be read by Prop92, so FOAQual can calculate the downstream damageability as described previously in Section 3.2.

One constraint to PSDI is the flaws on the optic must be sparse and well-spaced (>12mm), otherwise the focused PSDI image of the measured flaw will be contaminated by out-of-focus diffraction rings produced by the adjacent reference fiber. The CCD used is a Dalsa 1M30 with 1024 x 1024, 12 μm square pixels with 12-bits of digitization. The PSDI light source wavelength is 532 nm and requires a relatively short temporal coherence length of ~2 mm. This short coherence length is necessary to mitigate the appearance of ghost images of the flaw caused by double-bounce reflections created between the optic's front and rear surfaces, which vary between 10 and 45 mm. The source coherence function must also not repeat over this interval, or double-bounce interference artifacts will be generated on the CCD and contaminate the PSDI image background. Thus, a source with a long effective cavity (>100 mm) is desirable to extend the coherence function interval.

CHAPTER 4. SPATIAL COHERENCE AND IMAGING

Waves can explain many light phenomena, one of them being interference. The term *coherence* refers to the analysis of how light waves interfere. Light waves are a sinusoidally varying electromagnetic field oscillation that self-propagates as it travels through space while obeying Maxwell's equations [55-59]. Electromagnetic waves cover a wide continuous spectrum of oscillation frequencies, from extremely low frequency radio waves (3 Hz) to gamma rays (>10^{19} Hz). The light humans see with our eyes only covers a small sliver of the electromagnetic (EM) spectrum, called *visible light*. Visible light lies between the infrared and ultraviolet spectrums, roughly between the wavelengths of 400 and 700nm (in air), or oscillation frequencies between $7.5\text{x}10^{14}$ and $4.3\text{x}10^{14}$ Hz. Although, a precise definition of visible light is somewhat ambiguous because perception can vary slightly from person-to-person. The term *physical optics* refers to the analysis of light as an EM wave and its related phenomena.

Electromagnetic waves interfere due to the interaction of their electric fields. When EM waves cancel, we call it *destructive interference*. When they add together to increase in amplitude, we call it *constructive interference*. In order for EM waves to interfere, some component of their electric fields must align in the same direction. We describe the direction of the electric field in EM waves the *state of polarization* (or simply *polarization*). Polarization is described with respect to a reference plane. When the electric field direction is perpendicular to the reference plane it is called *S-polarized*, and when it is parallel it is called *P-polarized* (think plane polarized). If the relative states

of polarization are orthogonal, e.g. one wave is P-polarized and the other is S-polarized, interference does not occur since their electric fields will not interact.

Whether constructive or destructive wave interference occurs depends on the relative phase of the waves. Phase describes the relative position of the electric field as it oscillates between positive and negative values following a sinusoidal path. We describe phase as an angle (degree or radians) since the up and down oscillation of the electric field repeats continuously, as if it were following a circular path. Constructive interference occurs when the relative phase angles are *in-phase*, meaning they are different by an even integer factor of 2π, e.g. 0, 2π, 4π, 6π, etc. Destructive interference occurs when the relative phase angles are *out-of-phase,* meaning they are different by an odd integer factor of π, e.g. π, 3π, 5π, 7π, etc. When their phase difference is some other value, they combine to some state between constructive and destructive interference.

4.1 The Phasor Describes Light Oscillation

The *phasor* is an invaluable mathematical tool that describes the oscillation of light waves.[60-63] Imagine the phasor as a vector (an arrow) with the tail end fixed to the origin while the head rotates in a circle—like the hand of a clock. The rotation of the phasor represents the electric field wave oscillation. Each complete rotation signifies a complete cycle of electric field oscillation, as it accumulates a phase angle of 2π radian. The phasor vector lies on the complex plane, which has a real horizontal axis and an imaginary vertical axis, see Figure 4.1. The length of this phasor vector represents the amplitude of the electric field.

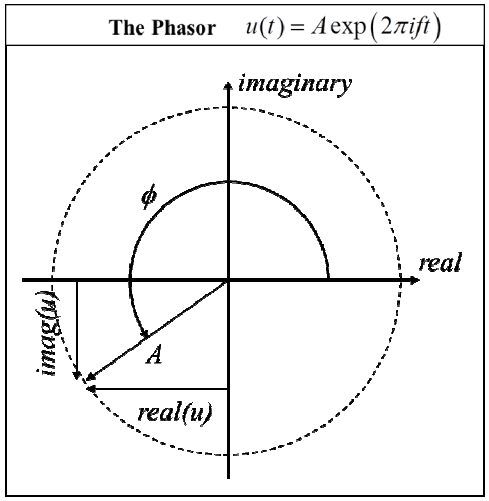

Figure 4.1: The phasor on the complex plane describes wave oscillation

The phasor is written mathematically as a complex exponential, thanks to Euler's famous equation: $\exp(i{\cdot}t) = \cos(t) + i{\cdot}\sin(t)$, where i is the imaginary number and t represents time. The sine and cosine in Euler's equation acts to project the length of the vector (the phasor) onto the real and imaginary axis respectively. The length of the arrows projected on the real axis describes the strength of the electric field through a complete oscillation cycle. Constants (or functions) added to the exponents in phasor describe the phase of the oscillation as it varies in time and/or space. For example, the phasor: $A\exp(2\pi if{\cdot}t)$ represent a wave with an electric field amplitude equal to A, that oscillates at frequency f (rotations per second), or a period $1/f$ (seconds per rotation). The phasor will be used extensively later in Chapters 5 and 6 to diffract the EM wave field (the illumination) through the object and through the lens to form an image.

4.2 Spatial Coherence and Illumination

Spatial coherence describes the interference potential of illumination depending on its size and shape.[63-66] The interferometer is a tool that records the 2D pattern

generated by interfering light waves on a viewing screen, which appear as alternating bright and dark lines called *fringes*. The resulting *contrast* of these fringes is defined as the ratio between the bright and dark regions in the pattern. Fringe contrast characterizes the coherence of the source. For example, a contrast of 80% indicates the fringes are well defined and easily visible since the ratio between the bright and dark regions is relatively high, while a contrast of 8% indicates a relatively low contrast, indicating the fringes may only be faintly visible. For this reason, fringe contrast is also referred to as *visibility*.

The double pinhole interferometer is a simple tool that can measure fringe contrast and demonstrate the relationship between source spatial coherence and fringe visibility. The double pinhole interferometer consists of a light source plane and an observation screen separated by an opaque screen that contains two pinholes. The source plane and interferometer screen are separated from the interferometer screen by roughly the same distances, which is much greater than the pinhole separation.

A point source cannot physically exist, since it is by definition infinitely small. However, the point source provides a convenient description of illumination, since temporally incoherent light sources (like the LPDI halogen source) can be decomposed into a collection of point sources. Thus, in the proceeding example, the illumination source will be described as a collection of point sources. The electric fields of the waves emitted by each of these points in the source oscillate independently of each other. This means the waves emitted by these point sources will not be observed to interfere with each other because their phases vary randomly and independently—too fast for the detector to record interference fringes over its exposure duration. Each point source

generates an expanding spherical wave at a single wavelength that propagates to the pinhole screen. After arriving to the pinhole screen, a small portion of each wavefront transmits through the two pinholes, which effectively generates two new expanding spherical waves that continues to propagate to the interferometer screen while preserving the phase of the source wave. This means that the phases of the two pinhole waves are correlated. Therefore, the two pinholes waves can be observed to interfere with each other, since the electric fields of the two pinhole waves oscillate together since they originated from the same source oscillation.

Figure 4.2 shows the resultant interference patterns for four different types of sources: A) a single point source, B) a pair of point sources, C) a continuous distribution of point sources, and D) an infinitely long continuous distribution of point sources. We observe that none of the pinhole screens show fringes, while three out of the four interferometer screens (A, B, and C) display sinusoidally varying interference fringes, but with decreasing fringe contrast of 80%, 50%, and 8%, respectively. Strictly speaking, each fringe pattern on the interferometer screen follows hyperbolic lines. However, when viewed over a small patch the fringe lines appear to be parallel. The shape of these interference fringes we observe on the screen is governed by the relative phase of each wave as a function of position of the wave interaction on the viewing screen. The pattern produced varies sinusoidally between constructive and destructive interference, which we call fringes. It might be easier to conceptualize the relative phase difference between the two waves as an optical path difference (OPD) between the two pinholes, since distances are more easily visualized. Fringes were not observed on any of the pinhole screens

because the phases of the waves produced by each point source in the illumination field were uncorrelated. The relative phases of each point source varied randomly and too fast for our detector to observe any interference effects. Conversely, the two pinholes waves were phase correlated, since their phase is governed by the phase of a singular point source in the source plane. Thus, interference between the two pinhole waves could be observed as fringes on the interferometer screen.

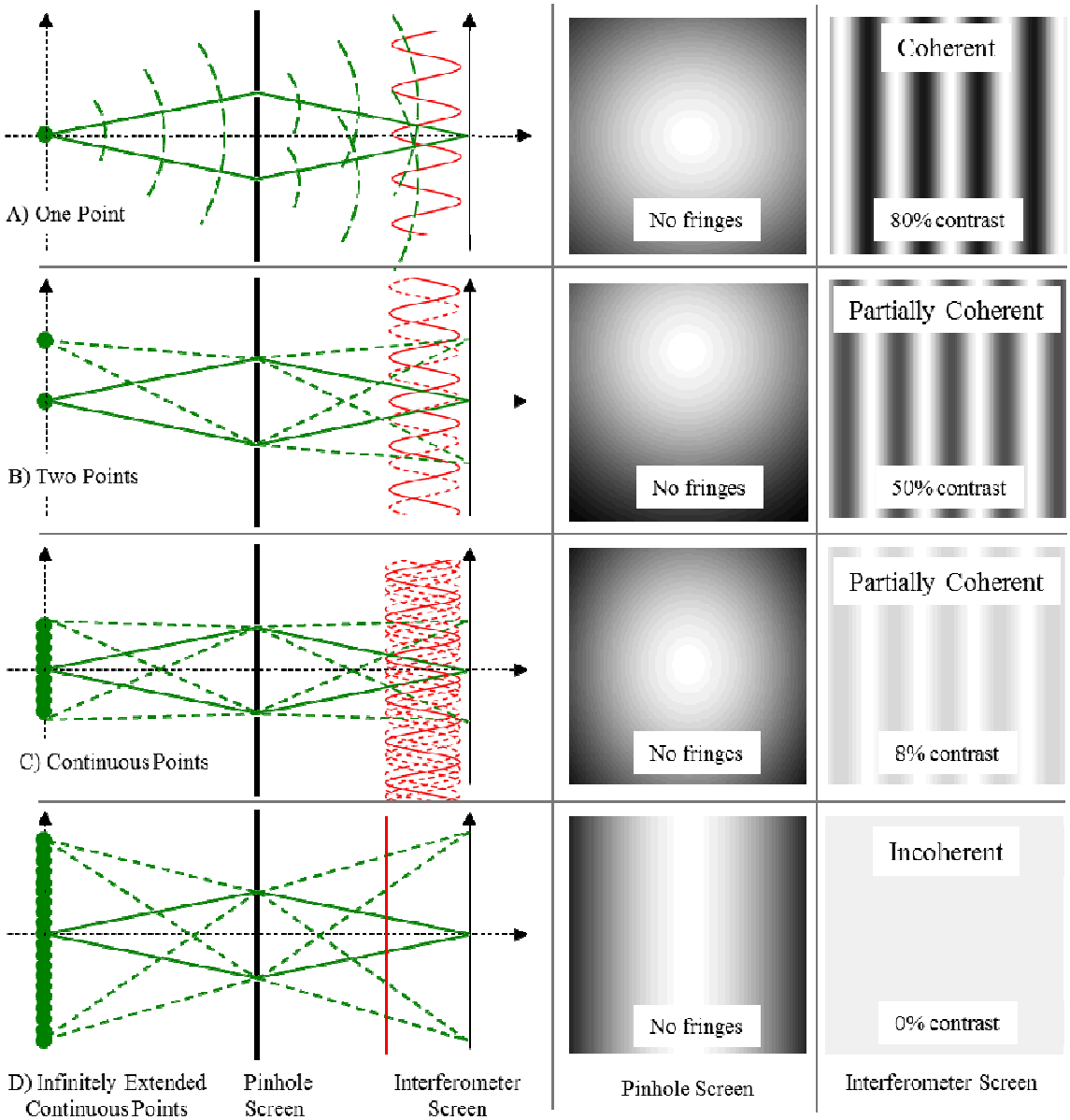

Figure 4.2: Double pinhole interferometer demonstrating spatial coherence

The double pinhole interferometer demonstrating the effect of spatial coherence using four types of point source distributions. The green lines represent the optical path lengths of between the point sources, pinholes, and interferometer screens. The top source is a single point source emitting a spherical wave that diverges as it propagates to the pinhole screen where it is divided into two new expanding spherical waves (one for each pinhole) that propagates to the interferometer screen. Interferences fringes were not observed on the pinhole screen because the phase of each point source are temporally uncorrelated. Interference was observed on the interferometer screens because each pinhole divided the wavefront of each source wave to produce a pair of temporally correlated waves that can

interfere. Fringe contrast is seen to decrease as the extent of the source increases due to the washing-out effect caused by the summation of the shifted independent fringe patterns produced by each pinhole wave—one for each point source in the distribution. Thus, more point sources results in lower spatial coherence, which we observe as lower fringe contrast.

Fringe contrast was lower for the pair of point sources (B) and the continuous source distributions (C and D) because those sources had lower spatial coherence. Recall, that any source behaves as a collection of point sources. Thus, the interference patterns produced by B, C, and D, forms as the sum of individual fringe patterns generated by each individual point source in the source plane. Each of these individual fringe patterns looks nearly identical to the fringe pattern produced by the single point source (A). However, each fringe pattern is shifted vertically relative to each other according to the height of the source point that generated it. The detector sums the irradiance of this collection of individual shifted fringe patterns, washing them out to result in reduced fringe contrast.

This example demonstrates the cause and effect of spatial coherence—larger light sources have lower spatial coherence. We observe lower spatial coherence as a reduction in fringe contrast. Source A is classified as fully spatially coherent because the source consisted of a single source that generated a single fringe pattern, which produced the highest possible fringe contrast. Sources B and C are classified as *partially coherent*, because they consisted of more than one point source, which reduces spatial coherence. Source D was classified as fully *incoherent*, because it was large enough to completely wash out the fringe pattern.

4.3 Spatial Coherence in Imaging Systems

Source spatial coherence can affect the appearance of images produced by imaging system in a similar way to what we just observed in the double pinhole interferometer. Imagine a lens aperture as just two very large overlapping pinholes that can also generate interference patterns on the observation screen. However, lenses are different from pinholes, so their interference effects appear different. Instead of interference fringes, interference effects in imaging system appear as artifacts in the image. The visibility of these image artifacts are governed by source spatial coherence, in a similar way to fringe visibility in the double pinhole interferometer. The visibility of interference artifacts in images are described by the *degree of spatially coherence*. The Köhler illumination system is a widely used method of illuminating specimens in optical microscopes and demonstrates the effect of spatial coherence in imaging systems.

4.4 The Köhler Illumination System

Köhler illumination was invented by August Köhler in the 1890s[67, 68] to improve image quality of optical microscopes. Prior to Köhler illumination, optical microscopes employed *critical illumination*, which imaged the light source directly on to the object plane. Thus, detail in the specimen could be masked by visible structure in the light source in the image since the source, object, and image shared common planes. Köhler illumination instead images the light source into the pupil of the objective, thereby maximally blurring any visible structure in the illumination. The Köhler illumination system and its many derivatives are widely employed in optical microscopes and lithographic systems today largely because of the following characteristics:

1) Complete defocus of the light source so its structure is not visible in the image

2) Restriction of illumination coverage to within the objective field of view to mitigate contrast reducing stray light

3) Complete fill of the numerical aperture of the microscope objective, thereby maximizing imaging system resolution while eliminating interference artifacts caused by source spatial coherence

The Köhler system in Figure 4.3 consists of a sequence of six planes, the source, field aperture, condenser aperture, object, objective pupil, and the image plane. The source, condenser aperture, and objective pupil planes share common focal planes, while the field aperture, object, and image planes share common focal planes. The objective lens images the object on to the image plane. The source consists of a disk shaped light source that is imaged by the field lens through the field aperture to the condenser aperture plane. The front focal point of the condenser lens is placed near the condenser aperture plane so that collimated light is sent through the object plane. The condenser lens also images the field aperture plane to the objective pupil plane, such that any structure in the illumination source is defocused on the image plane. In the Köhler system, the diameters of the field and condenser apertures can be changed to optimize imaging system performance. The diameter of the condenser aperture in effect controls the spatial coherence of the illumination.

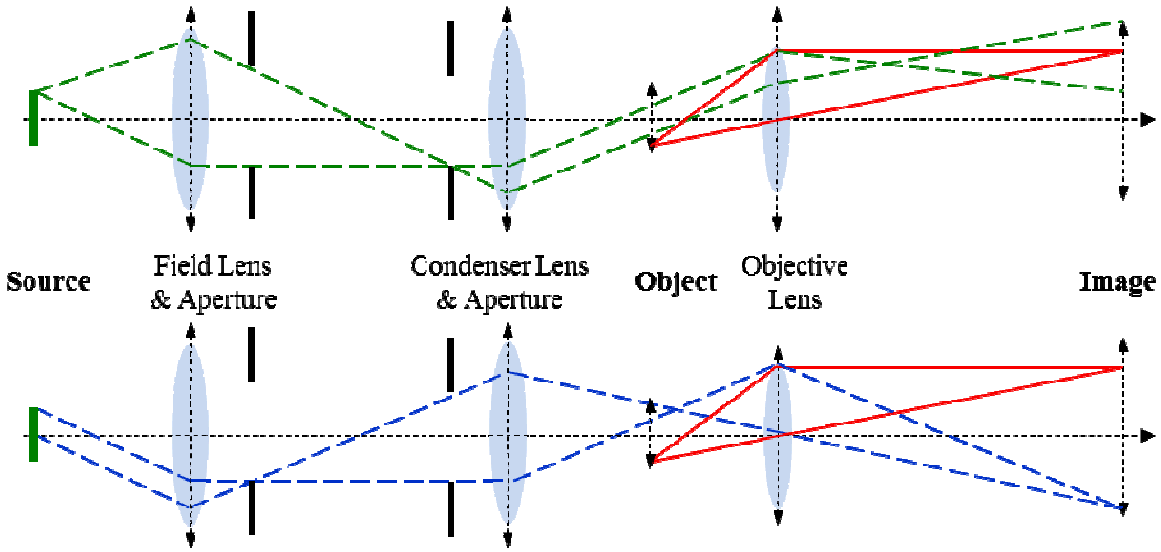

Figure 4.3: Köhler illumination system source and object conjugate planes

The Köhler illumination system, from left-to-right, consists of the six planes containing the following components: 1) Source, 2) Field Lens & Field Stop, 3) Condenser Lens & Stop, 4) Object, 5) Objective, and 6) Image. The top-half illustrates the path of the source rays (green-dashed lines) to show the source conjugate planes. The solid red rays represent the marginal and chief rays between the object and image conjugate planes. The green and blue dashed rays show the illumination system conjugate planes respectively. The source rays are imaged by the field lens to the condenser aperture plane, and then collimated by the condenser lens to illuminate the sample before being focused by the objective lens short of the image plane. Thus, the source is fully defocussed. The bottom-half illustrates the path of the illumination field rays to show the object conjugate planes.

4.5 Spatial Coherence of the Köhler Illumination

In the double pinhole interferometer example from Chapter 4, we saw that increasing the extent of the illumination source had the effect of lowering spatial coherence by reducing fringe contrast. The four example sources were composed of one or more point sources, and each point source in these source distributions generated its own independent fringe pattern on the interferometer screen. Each of these fringe patterns were shifted with respect to each other according to the height of the source point. When more than one of these shifted fringe patterns were summed by the detector we saw that

the resulting fringe pattern washed out. The washing-out effect of the fringe pattern was caused by a reduction in source spatial coherence.

The field lens in the Köhler system serves to collect light from the source and relay it to the condenser aperture plane. The light in the condenser aperture plane can be described as collection of independent point sources, each of which can interfere with itself but not with each other, just like the sources in the double pinhole interferometer in Figure 4.2. By placing the condenser lens at the front focal point of the condenser aperture plane, it acts to collimate the light emitted by each point source in the condenser aperture plane, in effect making each source behave as if it were illuminating the object from far away. Notice in Figure 4.3, that if we increase or decrease the diameter of the condenser aperture the spatial extent of the point source distribution will increase or decrease, thereby increasing or decreasing the spatial coherence of the illumination.

If we restrict the diameter of the condenser aperture such that it is very small, the illumination will behave as a single point source that illuminates the object with a single plane wave. Thus, when the object is illuminated with a single plane wave, it is called a coherent imaging system. The visibility of interference artifacts in the coherent image will be maximally visible, as was the case with the fringes produced by Source A in Figure 4.2. As we begin to increase the diameter of the condenser aperture, the source becomes larger, reducing the spatial coherence since the object is illuminated by multiple plane waves, as we saw with Sources B and C in Figure 4.2. Thus, the Köhler system becomes a partially coherent imaging system as we open the condenser aperture, which reduces the visibility of interference artifacts in the image. The system becomes fully

spatially incoherent when plane waves completely fill the NA of the objective, like Source D in Figure 4.2.

4.6 LPDI and the Köhler System

The LPDI illumination consists of a random distribution of fiber optics, as shown in Section 3.8. These fibers emit light that behaves as a linear array of point sources. The phase of each point source varies independently like the sources from the double pinhole interferometer example in Figure 4.2. Since these points sources are located a relatively far distance from the object, the spherical waves they emit become plane waves by the time they illuminate a small phase object in the optic.

The LPDI illumination source is analogous to placing a narrow off-axis slit in the condenser aperture plane of the Köhler system, like the illumination configuration used by the Hoffman Modulation Contrast microscope described in Section 2.3. If this Köhler system images the object with a low NA like the LPDI lens, most of the illumination will fall outside the objective NA to result in a dark-field image. Thus, another way to describe the LPDI system is as an “LPDI like” Köhler illumination system. The illumination in the Köhler system consists of a collection of point sources. The condenser lens converts each point source into a plane wave that illuminates the object. Each plane wave diffracts through the object and is collected by the objective lens to produces a collection of coherent image of the object on the image plane. As was the case with the fringe patterns produced by the double pinhole interferometer, this collection of independent coherent images are summed together by the detector such that interference

effects are washes-out as more and more independent patterns are added, which decreases the spatial coherence of the illumination.

4.7 Purpose of LPDI Image Simulation

An accurate image simulation code is a useful tool to study imaging system performance. Imaging system performance is best evaluated based on its intended application. The application pertaining to LPDI is the detection of small phase objects, specifically FPOs contained in large-aperture optics. Detection of such phase objects near the imaging system resolvability and sampling limits is a challenging problem that demands an imaging system capable of rendering small phase objects with substantial contrast since their signal will occupy just a few pixels. The LPDI system was designed to detect small phase objects in the optic in a few bright pixels against a dark background. Such an image is ideal for an automated image analysis algorithm to identify potential FPOs and transform their relative location in the image into a coordinate map (hit list) for high-resolution characterization, as previously described in the FICS process in Section 3.9. The contrast of phase objects in the LPDI image requires can be maximized through optimization of the imaging system parameters. Such an optimization task is best performed by an image simulation code, since doing so experimentally on the physical system may be prohibitively time consuming. Thus, in the following chapters, we shall describe an LPDI imaging system model that generates simulated LPDI images to optimize phase object contrast.

4.8 LPDI Image Simulation

The linescanning nature of LPDI allows us to break-up a large phase object, like a 400 x 400 mm^2 aperture NIF optic, into a collection of small transparent phase objects. We can do this because the linescan imaging method maintains the illumination geometry across the optic during a scan. Each microscopic phase object in the optic under inspection is effectively illuminated by an identical set of plane waves. Recall, Figure 1.2 showed the active FOV of the each linear LPDI frame was defined by the linear sensor width in object space, which can be calculated as the pixel width divided by lens magnification. In the FICS LPDI system, the sensor pixel width is 9 µm and the magnification is 0.16. Therefore, the active FOV in object space for each linear frame represents a very narrow slit, 56 µm wide and 448 mm tall, for the linear image sensor containing 1x8000 pixels. The signal recorded by each of these linear frames is the fraction of plane wave illumination diffracted by the object and redirected into the lens NA and onto the pixels on the CCD. Thus, light in the LPDI system is spatial filtered in two places: firstly, by the lens pupil, and secondly by the active region of each pixel. The key concept to realize is that the LPDI system spatially filters all light diffracted through the object the same way. Accordingly, we can treat the LPDI system as generically as a *Köhler like* imaging system, which illuminates the object with an identical set of set of plane waves. We defined such a system previously in Section 4.5 as a partially coherent imaging system. In general, a partially coherent imaging system is one that illuminates an object by multiple plane waves, as illustrated in Figure 4.4.

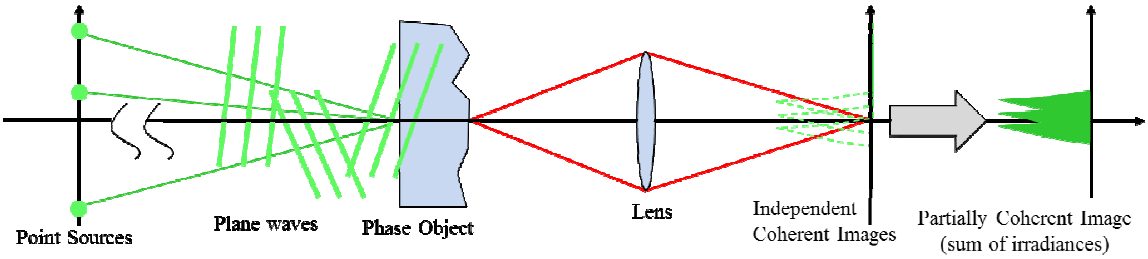

Figure 4.4: LPDI imaging system model for partially coherent imaging

The above illustrates a generalized model of the partially coherent illumination in the LPDI imaging system. Plane waves are generated by a collection of point sources located a relatively large distance from the object. The lens forms a collection of coherent images on the image plane produced by each plane wave diffracted through the object. Each of these independent coherent image irradiances are summed together by the detector to result in the final recorded image.

In the two chapters that follow, an LPDI imaging model will be constructed from the ground-up, starting in Chapter 5 with the mathematics needed to generate simulated coherent images using a physical optics approach. In Chapter 6, the mathematics of coherent image simulation will be expanded to a partially coherent image system that can generate simulated LPDI images. In Chapter 7, the accuracy of this LPDI image simulation code will be evaluated by comparing simulated and measured images of many different types of real FPOs of interest. Finally, concluding with a discussion of this model of LPDI in Chapter 8.

CHAPTER 5. COHERENT IMAGE SIMULATION

In this Chapter, we describe the mathematics needed to generate coherent images using a physical optics approach. As was described previously in Chapter 4, physical optics describes light as an electromagnetic wave. Physical optics as opposed to geometrical optics, which describes light as a collection of lines called rays that define the path of light as it undergoes refraction and reflection from point-to-point through an optical system. Thus, light waves in physical optics are said to *diffract* instead of *refract*, like the rays in geometrical optics.

5.1 Derivation of Physical Optics based Imaging

The mathematics that describe the propagation of light waves through free-space and optical component are quite complex. However, following some simplification, wave propagation through an imaging system can be reduced to a simple two-dimensional spatial filter operation that transfers the spatial frequencies in the light field on the object plane directly to the spatial frequencies on the image plane. The derivation of the mathematics used in this imaging method is quite elegant, but lengthy, so it will not be derived here. However, we will describe the general process of its derivation starting from first principles of Maxwell's equations: [62, 63, 69, 70]

1) Maxwell's equations in vacuum

2) Homogeneous time-independent wave equation

3) Rayleigh-Sommerfeld diffraction theory (ensemble of spherical waves)

4) The Fresnel approximation (paraboloidal approximation of spherical waves)

5) Canceling quadratic phase factors between the parabolic waves and lens

6) Finally, imaging by transfer function (2D spatial filter)

Since the Fourier transform is invaluably and used extensively, this method of imaging is referred to as *Fourier Optics*. One of the fundamental principal of Fourier optics is that any arbitrary light field on a plane can be decomposed into a spectrum of plane waves. These plane waves can be individually propagated to a downstream plane and summed together to produce the diffracted light field. The proceeding analysis of the LPDI imaging system omits the time dependence of the electric field oscillation, so the light field will only have spatial dependence in the object and image planes.

5.2 Coherent Imaging Model

We shall define a coherent imaging system as one in which the object plane is illuminated by a single monochromatic plane wave. Our coherent imaging system is located in air (index of refraction equal 1). As illustrated in Figure 5.1, it consists of four planes containing: 1) a point source, 2) the object, 3) an imaging lens, and 4) the image. The object is thin and is described as a function of spatial coordinates $[x, y]$ and is illuminated by a plane wave generated from a single point source located a distance z_s behind the object. The point source emits an expanding spherical wavefront at wavelength λ that diverges as it propagates to the object from coordinates $[x_s, y_s]$. The distance between this point source and the object plane is very large in comparison to the spatial extent of the object, i.e. $z_s >> \max(\mathrm{sqrt}(x^2 + y^2))$. Thus, the radius of curvature of this spherical wavefront becomes very large by the time it reaches the object—large enough to treat it as a single plane wave. The sag of the wavefront within the spatial

extent of the object is less than a few λ. The source coordinates govern the slope of incidence of this plane wave with respect to the object plane, as defined by $\alpha = x_s/z_s$, in the xz-plane, and $\beta = y_s/z_s$, in the yz-plane.

Located a distance s to the right of the object is an imaging system that we shall refer to generically as a *lens*. The lens is defined by its entrance pupil diameter D, and magnification m, and forms an image on the object by focusing the plane wave diffracted through the object onto the image plane, which is located a distance p to the right of the lens. The numerical aperture of the lens is defined as $NA = \sin\square$, where $\square$ represents the half-angle of its light acceptance cone (or its marginal ray angle). After applying the small angle approximation, which is valid for small numerical apertures, the above equation simplifies to $NA = D/(2s)$, which is the slope of the marginal ray angle.

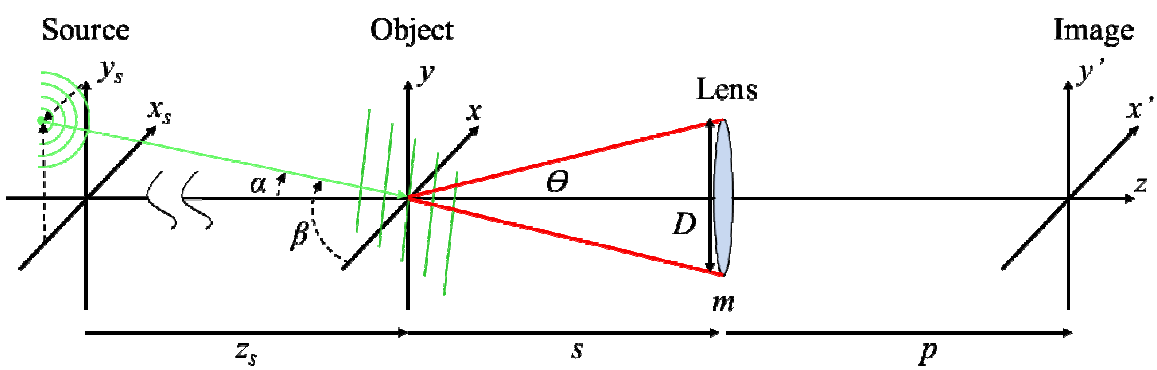

Figure 5.1: The imaging system model

Shown above is the imaging system model consisting of a z-axis and three planes. From left-to-right, these three planes contain the source, object, and image. The imaging lens is defined by its numerical aperture NA and magnification m, and forms an image of the object on the image plane. The source plane contains a single point source located a distance z_s from the object plane and illuminates the object plane with a single plane wave. The object coordinates are [x, y], while the image coordinates are *primed* [x', y'].

5.3 Plane Wave Field

The point source position is defined by the vector, $\mathbf{r}_s = [x_s, y_s]$. The plane wave that this point source generates is defined by the spatial frequency of its oscillation in the *xy*-plane, which depends on the point source position vector and the wavelength of light λ, and is written in vector form as

$$\boldsymbol{\rho}_s = \left[\xi_s = \frac{x_s}{z_s \lambda}, \eta_s = \frac{y_s}{z_s \lambda} \right], \tag{5.1}$$

where ξ_s and η_s are the spatial frequency of the plane wave projected on to the *x*- and *y*-axes respectively. The point source coordinate and plane wave spatial frequency vectors are illustrated in their respective planes are shown below in Figure 5.2.

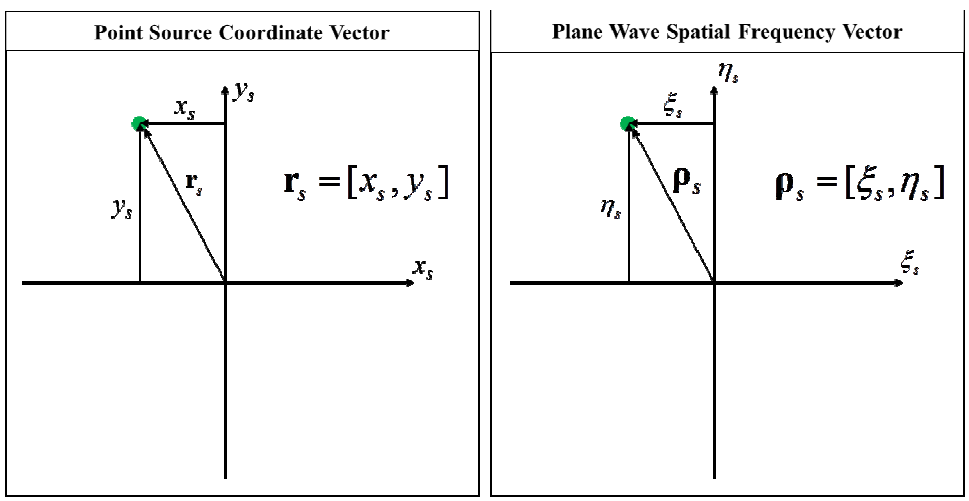

Figure 5.2: Point source and plane wave coordinate axes

The point source vector (left) lies in the Cartesian plane, and produces a plane wave defined by its spatial frequency vector (right).

The field representing the plane wave oscillation illuminating the object is now constructed using the phasor (described in Chapter 4). The time dependence of the plane wave oscillation is omitted, thus it has only spatial dependence in the object plane

$$u_{pw}(\mathbf{r}) = A\exp[-2\pi i\boldsymbol{\rho}_s \cdot \mathbf{r}], \tag{5.2}$$

where A is the amplitude of the light field, and $\mathbf{r} = [x, y]$ is the object coordinate vector.

5.4 Object Transmittance Function

The object diffracts the incident plane wave in transmission. Diffraction of the plane wave depends on separable amplitude and phase components in the object, defined as a function of object position vector $\mathbf{r}$. The phase component in the object delays the phase of the incident plane wave, while the amplitude component attenuates its amplitude. The phasor also describes the object transmittance function

$$\mathfrak{t}_{obj}(\mathbf{r}) = a(\mathbf{r}) \cdot \exp[ikh(\mathbf{r})], \tag{5.3}$$

where $a(\mathbf{r})$ is a 2D map that describes the object amplitude transmittance in the xy-plane, and $h(\mathbf{r})$ is another map that describes the object's phase in transmission. The amplitude transmittance map has values that vary between zero (no light is transmitted) and one (all light is transmitted), while the phase map $h(\mathbf{r})$ describes the phase delay imparted to the plane wave in units of phase angle (radians). It is common to convert phase angle into a physical length, called an optical path difference (opd). In phase objects, an opd occurs whenever there is a change in the physical thickness of the object or a change in its index of refraction.

For a pure phase objects, the transmittance function only has phase dependence, thus the amplitude component $a(\mathbf{r})$ is set equal to one. This means pure phase objects transmit 100% of the incident plane wave. Each xy-component in a phase object redirects the incident plane wave in a new direction. For a pure amplitude object, the complex exponential term can be set equal to one since it only has amplitude dependence.

5.5 Field Transmitted through the Object

The field transmitted through the object u_{out}, is computed simply by multiplying the plane wave field and object transmittance together (Eq. 5.2 and 5.3)

$$\begin{aligned} u_{out}(\mathbf{r}) &= u_{pw}(\mathbf{r}) t_{obj}(\mathbf{r}) \\ &= A \exp[-2\pi i \boldsymbol{\rho} \cdot \mathbf{r}] \exp[2\pi i h(\mathbf{r})] \end{aligned} . \tag{5.4}$$

The exponents of these two functions are now combined

$$u_{out}(\mathbf{r}) = I \exp[2\pi i \{h(\mathbf{r}) - \boldsymbol{\rho} \cdot \mathbf{r}\}] . \tag{5.5}$$

In this form, the effect of the plane wave is to shift the phase of the object transmittance function. After invoking the Fourier shift theorem (described in Appendix A), the plane wave effectively shifts the spatial frequency components of the object according to the plane wave spatial frequency vector $\boldsymbol{\rho}_s$

$$\begin{aligned} U_{out}(\boldsymbol{\rho}) &= \mathbf{F}_{\mathbf{r}} \left\{ t_{obj}(\mathbf{r}) u_{pw}(\mathbf{r}) \right\} \\ &\quad \mathbf{F}_{\mathbf{r}} \left\{ A \cdot t_{obj}(\mathbf{r}) \exp[-2\pi i \boldsymbol{\rho}_s \cdot \mathbf{r}] \right\} . \\ &= A \cdot T_{obj}(\boldsymbol{\rho} - \boldsymbol{\rho}_s) \end{aligned} \tag{5.6}$$

where $\mathbf{F}_{\mathbf{r}} \{ \ \}$ denotes forward Fourier transform as described in Appendix A, and T_{obj} represents the frequency components of the object, explicitly the Fourier transform of Eq. 5.3.

5.6 Imaging as a Spatial Filtering

An image of the light diffracted through the object is now produced by multiplying the lens system transfer function $H(\boldsymbol{\rho})$, with the spatial frequency components transmitted through the object

$$U_{img}(\boldsymbol{\rho}) = H(\boldsymbol{\rho})U_{obj}(\boldsymbol{\rho}). \tag{5.7}$$

The transfer function $H(\boldsymbol{\rho})$, represents a spatial filter that filters the spatial frequency components in $U_{out}(\boldsymbol{\rho})$ to yield the plane wave spatial frequency components collected by the lens entrance pupil. Visualize Eq. 5.7 to represent the spatial frequency components in the lens pupil. The spatial frequencies in pupil are now transformed into the resulting field on the image plane by performing an inverse Fourier transform of Eq. 5.7

$$u_{img}(\mathbf{r}') = \mathsf{F}_{x,y}^{-1}\left\{U_{img}(\boldsymbol{\rho})\right\}. \tag{5.8}$$

where $\mathbf{r}' = m\mathbf{r}$, is a coordinate transformation that accounts for the rectilinear scaling and inversion of the object as produced by an ideal lens.

5.7 The Transfer Function

We just described the imaging system transfer function (TF) as a spatial filter. The lens entrance pupil defines the shape of this spatial filter for an ideal aberration-free imaging system. The entrance pupil acts to collect the planes transmitted through the object that fall within a specific range of spatial frequencies. Increasing the diameter of the lens entrance pupil allows it to collect higher spatial frequency planes waves. Typically, imaging lenses have circular pupils, thus we shall use a circular TF as an example, which can be described mathematically as

$$H(\boldsymbol{\rho}) = \mathrm{circ}\left(\frac{2\sqrt{\xi^2+\eta^2}}{\rho_{cutoff}}\right), \tag{5.9}$$

where ρ_{max} is the magnitude of the maximum spatial frequency collected by the lens entrance pupil, which represents the radius of the entrance pupil. The function circ() as defined by Gaskil, is a circular region equal to 1 when the numerator is less than the

denominator, and equal to ½ when the numerator and denominator are equal, and 0 everywhere else.[62] Thus, the denominator in the argument of the circ() function in effect defines the radius of the circular spatial filter. In Eq. 5.9, the radius of the circular region is ρ_{max}, which is the spatial frequency cut-off of the lens TF as computed as

$$\rho_{\max} = \frac{NA}{\lambda}. \tag{5.10}$$

Equation 5.10 illustrates shows that increasing *NA* increases the transfer function spatial frequency cut-off $\rho_{\max}$. A higher cut-off frequency allows the lens to collect higher spatial frequencies and resolve smaller objects. An example pupil transfer function, with a cut-off of 100 mm^{-1}, is shown below in Figure 5.3.

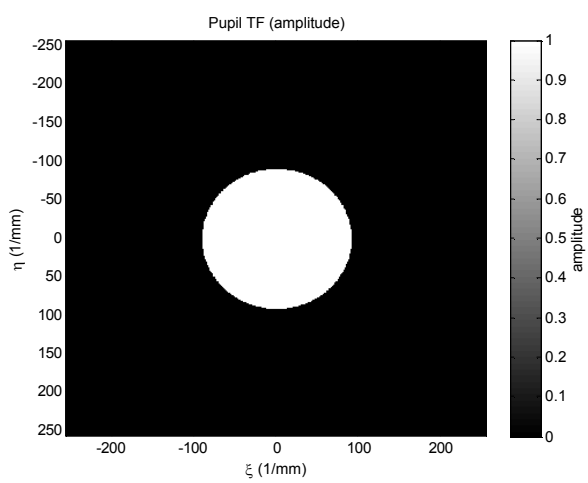

Figure 5.3: Example coherent imaging system transfer function

5.8 Linear Shift Invariance

The imaging operation defined by Eq. 5.8 is valid if the system transfer function H(**ρ**) is *linear shift-invariant* (LSI). The TF H(**ρ**), is linear if it obeys the following property[62]

$$H\left[au_1(\mathbf{r})+bu_2(\mathbf{r})\right]=aH\left[u_1(\mathbf{r})\right]+bH\left[u_2(\mathbf{r})\right], \tag{5.11}$$

where u_1 and u_2 are independent functions weighted by the complex constants a and b. One way to interpret linearity is the TF can act on each plane wave component independently. This is a foundational concept of Fourier optics.

Shift-invariance means the transfer function does not depend on the position of the object. Shift-invariance means a shifted object results in a shifted image, which can be stated mathematically as follows[62]

$$\begin{aligned} Hu_1(x)&=u_2(x)\\ Hu_1(x+x_o)&=u_2(x+x_0) \end{aligned}, \tag{5.12}$$

where H is the system transfer function that acts on a function $u_1(x)$ to produce $u_2(x)$. Thus, the transfer function H obeys shift-invariance if when it acts on a shifted version of u_1, i.e. $u_1(x+x_0)$, it produces a shifted version of u_2, i.e. $u_2(x+x_0)$.

5.9 Lens Aberrations

A perfect aberration-free imaging system can obey LSI. However, real imaging system have aberrations, which are imperfections in the imaging system lens that deviate the light transmitted through the lens from an ideal spherical wavefront. Recall in our imaging system model that the phase object transmits a collection of plane waves that propagate to the lens, which are collected by the entrance pupil. Imagine the lens as a *black box* that converts each plane waves into a spherical wavefront that converges to a spot on the image plane. Lens aberrations are thus described as the phase difference between this ideal perfect spherical wavefront and the actual wavefront shape output by the lens. Lens aberrations can be incorporated into our imaging system model by adding

this phase difference (the aberrations) to pupil TF, $H(\boldsymbol{\rho})$. Aberrations may violate the condition for LSI because they may depend on object position. The condition for LSI can be restored in aberated imaging systems by constructing the image from pieces of the object broken-up into a collection of small *isoplanatic patches*, defined over an appropriately small area where the condition for LSI is approximately valid.

Even ideal imaging systems violate the condition for LSI, but in trivial way. The ideal lens produces an image that is a scaled version of the object, i.e. the image is a facsimile of the object, but magnified or demagnified and inverted and reverted (upside down and backwards). Magnification and flipping of the object voids the condition for shift-invariance. However, LSI can be recovered by a trivial transformation of coordinates that scales the image coordinate vector by the magnification factor m, using the following substitution of variables, $\mathbf{r'} = m\mathbf{r}$, which acts to scale (magnify) and transpose the image as a real imaging system would.

5.10 Transfer Function Shift

Previously, we showed that the plane wave illuminating the object effectively shifts the object by spatial frequency $\boldsymbol{\rho}_s$. A mathematically equivalent operation is to instead shift the pupil transfer function (Eq. 5.7) by $\boldsymbol{\rho}_s$

$$\begin{aligned} U_{img}(\boldsymbol{\rho}') &= H(\boldsymbol{\rho})\mathbf{F}_{\mathbf{r}}\left\{\exp[-2\pi i\boldsymbol{\rho}_s\cdot\mathbf{r}]\exp[2\pi ih(\mathbf{r})]\right\} \\ &= H(\boldsymbol{\rho}-\boldsymbol{\rho}_s)\mathbf{F}_{\mathbf{r}}\left\{\exp[2\pi ih(\mathbf{r})]\right\} \end{aligned} . \tag{5.13}$$

This form of computing the image will be exploited later in Chapter 6 to simplify the partial coherent transfer function. This operation appears physically invalid. However, it does result in the same image.[66]

5.11 Image Irradiance

Image sensors detect the irradiance of the incident optical field. Irradiance has units W/m^2, which describe the integrated quantity of optical power illuminating a unit area. Thus, we must convert the field on the image plane to the proportional irradiance on the image plane E_{coh}, by multiplying the light field by its complex conjugate

$$\begin{aligned} E_{coh}(\mathbf{r}') &\propto u_{img}(\mathbf{r}')u_{img}^{*}(\mathbf{r}') \\ &\propto \left|u_{img}(\mathbf{r}')\right|^2 \end{aligned} , \tag{5.14}$$

where the * represents the complex conjugate. This calculation is also described as the *magnitude-squared* of the electric field. Additional constants need to be added to Eq. 5.14 to compute the exact irradiance to yield the correct units. However, proportional irradiance is sufficient for this image simulation.

5.12 Coherent Image Simulation Example

An image simulation code for coherent illumination was written in The Mathworks Inc. MATLAB™[71] by implementing Eq. 14 to compute image irradiance for an input phase object illuminated by a plane wave at spatial frequency $\boldsymbol{\rho}_s$ and imaged by a lens of numerical aperture *NA* and magnification *m*. To demonstrate this image simulation code, a real phase object found on the surface of a fused silica optic was used

in the following examples of coherent image simulation. The phase of this object was measured in transmission by PSDI. The object is ~500µm in diameter and has a PV opd of 250nm.

This example demonstrates the effect of two parameters in the coherent image: One, the plane wave spatial frequency $\boldsymbol{\rho_s}$, and two, the imaging system numerical aperture *NA*. The following four figures show simulated images of the same object produced by a relatively small or large NA described as *f*-numbers (*f*/16 and *f*/5.6), and illuminated by a relatively slow and fast plane waves (16.5 mm^{-1} and 3.3 mm^{-1}). These *f*-numbers and plane wave spatial frequencies are representative of the LPDI imaging camera (see section 3.4) and the linear illumination source offset. The *f*-number is standard method in photography to express the relative lens aperture, which describes the lens entrance pupil diameter as a factor of lens effective focal length.

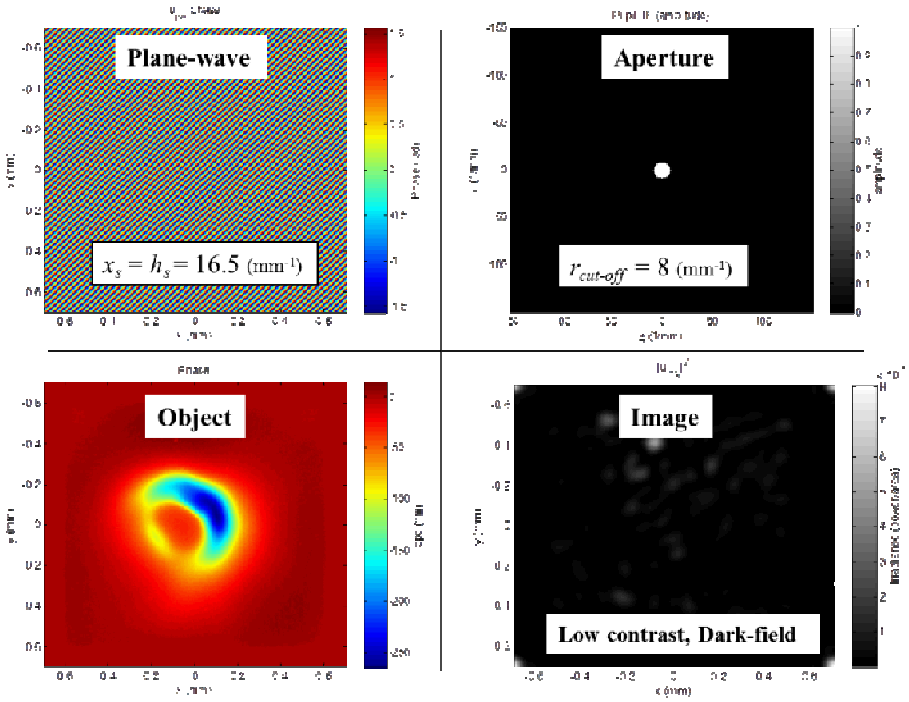

Figure 5.4: Fast plane wave, low NA (f/16) yields low contrast dark-field image

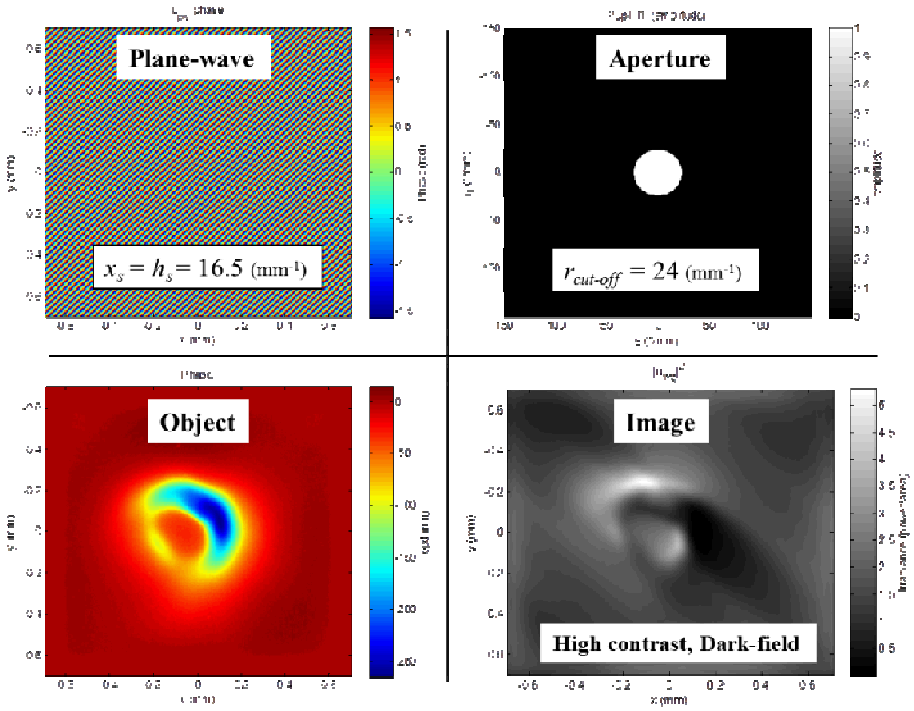

Figure 5.5: Fast plane wave, high NA (f/5.6) yields high contrast dark field image

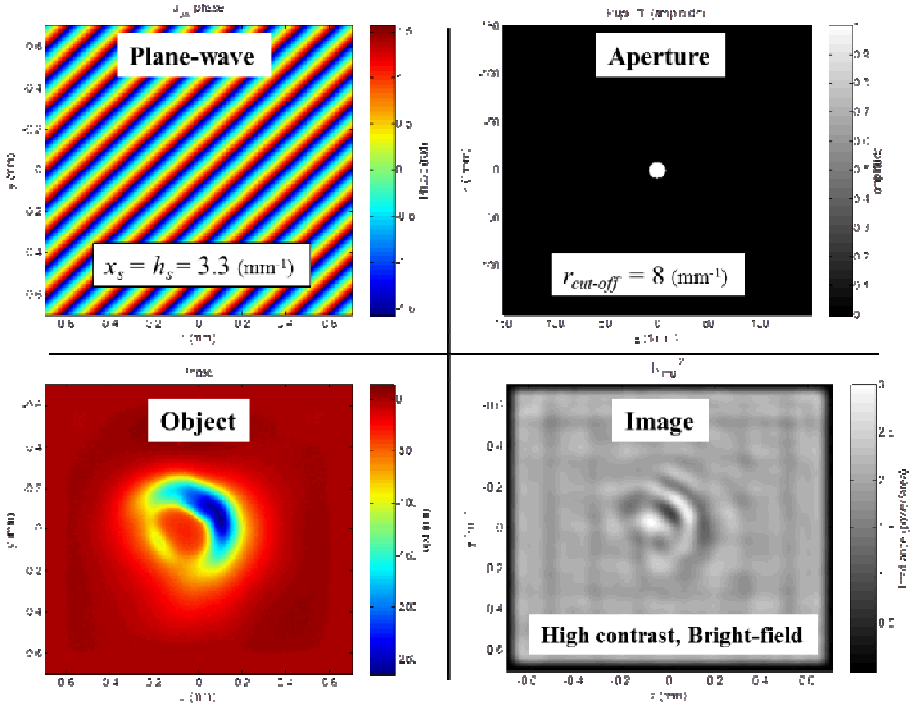

Figure 5.6: Slow plane wave, low NA (f/16) yields high contrast bright-field image

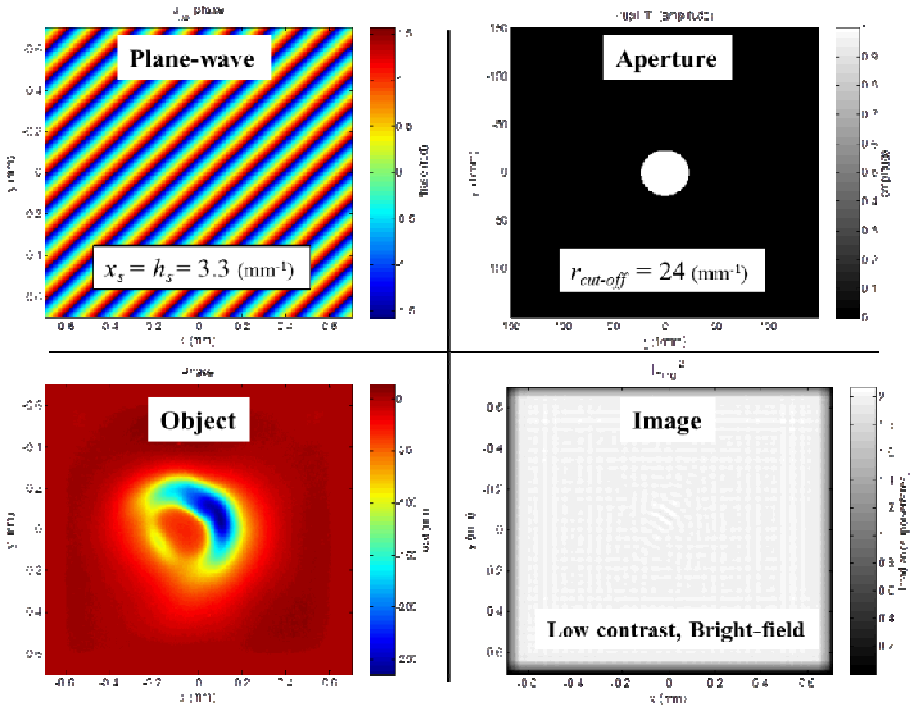

Figure 5.7: Slow plane wave, high NA (f/5.6) yields low contrast bright-field image

These examples demonstrate how the coherent image of phase objects can change dramatically depending on the plane wave illumination spatial frequency and numerical aperture. In the four examples, we saw very different levels of image contrast and background type (dark-field or bright-field). For phase object detection, contrast is the parameter we seek to optimize. It is apparent in these example that image contrast can be optimized by adjusting the NA and plane wave spatial frequency.

Dark-field images were produced for the imaging systems that were illuminated by relatively fast plane waves because the pupil acted as a spatial filter that blocked the background illumination since the plane wave spatial frequency exceeded the lens cut-off frequency, ρ_{max}. Conversely, bright-field images were produced for the slow plane wave cases, since the plane wave spatial frequency was less than the cut-off frequency of the

pupil. In these cases, bright-field images were produced because the background light was not blocked. We also see that *NA* and $\boldsymbol{\rho_s}$ are coupled parameters that determine image contrast. The larger *NA* systems had superior contrast in the dark-field case, while a low *NA* system had superior contrast in the bright-field case. Thus, the condition for optimal phase object contrast can be determined by selecting the correct balance between plane wave spatial frequency and numerical aperture.

CHAPTER 6. PARTIALLY COHERENT IMAGE SIMULATION

The previous chapter developed the required mathematics to simulate images of phase objects illuminated by a single plane wave. This was defined as *coherent image simulation* because the illumination contained a single plane wave at spatial frequency $\boldsymbol{\rho}_s$. A partially coherent imaging system is now defined as an object illuminated by more than one plane wave. In this chapter, we expand the imaging system model for a partially coherent system by generalizing the illumination field to N_s independent point sources. Each point source illuminates the object with a plane wave at the object plane and produces an independent coherent image on the image plane—just as each point source produced an independent fringe pattern on the interferometer screen in the double pinhole interferometer, see Section 4.2. Thus, the partially coherent image is calculated by summing each independent coherent image irradiance generated by each point source.

6.1 Partially Coherent Image Irradiance

As was the case with the source in the double pinhole interferometer examples from Chapter 4, the phases of these point sources vary independently of each other. This means that the individual plane waves produced by each point source can interfere with itself on the image plane, but not with each other. Thus, as was the case with the fringe pattern observed on the double pinhole interferometer screen, the partially coherent image is detected as the sum of the individual coherent image patterns, as computed by Eq. 5.14, to produce the proportional partially coherent image irradiance, E_{pcoh}

$$E_{pcoh}(\mathbf{r}') \propto \sum_{j=0}^{N} \left| u_{j,img}(\mathbf{r}') \right|^2 , \tag{6.1}$$

where $u_{j,img}$ represents the individual coherent image fields produced from each point source, which are indexed by the integer j. Each $u_{j,img}$ image in Eq. 6.1 is computed the same as was described in Chapter 5 using a shifted TF, as in Eq. 5.13. Thus, we substitute Eq. 5.13 into Eq. 6.1 to compute E_{pcoh} using a collection of $H_j(\boldsymbol{\rho}\text{-}\boldsymbol{\rho}_s^j)$ shifted pupil transfer functions

$$E_{pcoh}(\mathbf{r}';\boldsymbol{\rho}_s^j) \propto \sum_{j=0}^{N} \left| \mathsf{F}_{\boldsymbol{\rho}}^{-1} \left\{ H_j(\boldsymbol{\rho}-\boldsymbol{\rho}_s^j) T_{obj}(\boldsymbol{\rho}) \right\} \right|^2 , \tag{6.2}$$

where $\boldsymbol{\rho}_s^j$ is a vector representing the set of plane wave spatial frequencies from each point source. Thus, $H_j(\boldsymbol{\rho}\text{-}\boldsymbol{\rho}_s^j)$ represents a discrete set of shifted transfer functions, with each H_j representing a shifted TF as shifted by spatial frequency $\boldsymbol{\rho}_s^j$.

6.2 SVD Speeds Computation

Equation 6.2 is a valid algorithm to use in an incoherent image simulation. However, this form is computationally laborious since N_s inverse fast Fourier transforms (FFTs) are needed to compute the image. We can significantly speed computation by reducing the number of FFTs, by avoiding computing Eq. 6.2 explicitly by brute-force. We do this by evaluating Eq. 6.2 using a reduced version of $H_j(\boldsymbol{\rho}\text{-}\boldsymbol{\rho}_s^j)$, by decomposing it into a set of eigenfunctions and eigenvectors using Singular Value Decomposition (SVD). This method was described by Kenji Yakamozoe[72]. The SVD reduced form of H_j transforms it into N_s eigenfunctions $\boldsymbol{\Phi}_j(\boldsymbol{\rho})$ and eigenvalues $\boldsymbol{\mu}_j$, which are then used to compute the proportional partially coherent image irradiance

$$E_{pcoh}(\mathbf{r}') \propto \sum_{j=1}^{N} \boldsymbol{\mu}_j^2 \left| \mathsf{F}_{\boldsymbol{\rho}}^{-1} \left\{ T_{obj}(\boldsymbol{\rho}) \boldsymbol{\Phi}_j(\boldsymbol{\rho}) \right\} \right|^2, \tag{6.3}$$

where $\boldsymbol{\mu}^2_j$ is an exponentially decaying weight factor. The exponential decay of $\boldsymbol{\mu}^2_j$ means that only a few dozen eigenterms (e.g. N = 36) need to be evaluated in Eq. 6.3 to obtain a very good approximation of E_{pcoh}. By comparison, Eq. 6.2 would require 256 FFTs. Thus, reducing the number of FFTs to 36, greatly speed computation. Equation 6.3 was derived by substituting the SVD reduced form of the stacked pupil into Eq. 6.2, followed by linear algebraic manipulation. This derivation can be reviewed in Appendix A. In the next Chapter, Equation 6.3 will be used to compute simulated LPDI images.

6.3 Plane Wave Spatial Frequency Distribution

Micrographs of the LPDI linear illuminator in Figure 3.10 show that it consists of a collection of 50µm core diameter optical fibers. White light emitted from a halogen source is coupled into these fibers. However, an absorptive filter on the green channel in the linear sensor filters this light into a narrow spectrum before it reaches the CCD. Thus, the light recorded by the sensor is quasimonochromatic, meaning it behaves as if it were monochromatic light. Each fiber emitter is randomly distributed within a rectangular aperture, and is w_y = 800 mm tall by w_x = 0.4 mm wide. This distribution of point sources corresponds to a rectangular distribution of plane wave spatial frequencies, as computed by Eq. 5.1. This distribution is centered about spatial frequency vector

$$\boldsymbol{\rho}_{s0} = [\xi_{s0}, \eta_{s0}],$$

where $\xi_{s0} = x_s/z_s/\lambda$ and $\eta_{s0} = y_s/z_s/\lambda$ and has bandwidth as expressed by the vector

$$\boldsymbol{\rho}_{sw} = [\xi_{sw}, \eta_{sw}],$$

where $\xi_{sw} = \xi_{s,max} - \xi_{s,min}$ and $\eta_{sw} = \eta_{s,max} - \eta_{s,min}$, and where $\xi_{s,max} = (x_{s0} + w_x)/2/z_s/\lambda$ and $\xi_{s,min} = (x_{s0} - w_x)/2/z_s/\lambda$; and $\eta_{s,max} = (\eta_{s0} + w_y)/2/z_s/\lambda$ and $\eta_{s,min} = (\eta_{s0} - w_y)/2/z_s/\lambda$.

Since the source is very narrow in the x-axis (0.4mm), the spatial frequency distribution in the x-axis can be approximated as infinitely narrow, i.e. $\xi_{sw} \rightarrow 0$. Conversely, since the source in the y-axis is very tall (~800mm) it can be approximated to produce a spatial frequency distribution that is infinitely wide, i.e. $\eta_{sw} \rightarrow \infty$. Conceptualize the source distribution as a slit that is very narrow in x-direction and very tall in the y-direction. The source is similar to the source in a Hoffman Modulation Contrast microscope described in Chapter 2. In the LPDI image simulation code, the distribution is sampled discretely by a uniform random number generator using the MATLAB™ function rand(), to produce a N_sx2 dimensional matrix representing the spatial frequency coordinates of each plane wave illuminating the object, as shown by the example in Figure 6.1.

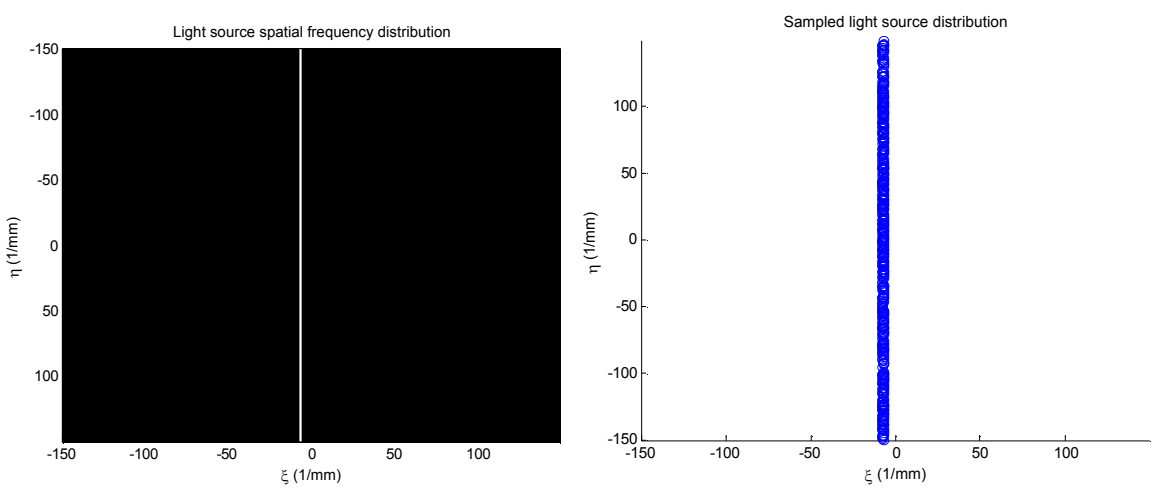

Figure 6.1: Continuous and discrete (sampled) plane wave distributions

The distribution on the left represents the continuous distribution of plane wave spatial frequencies in the LPDI imaging system as a narrow slit in frequency space. The

distribution on the right was derived from the distribution on the left by random sampling. This simulates the random spatial distribution of the physical fiber light source.

6.4 Polychromatic Plane Wave Distribution

For the case of a polychromatic source, the illumination spectral distribution can be incorporated into the sampled source spatial frequency distribution by adding a wavelength dependent sampling term to each plane wave slope

$$\xi_{s:j,k} = \alpha_j/\lambda \text{ and } \eta_{s:j,\,k} = \beta_j/\lambda_k,$$

where $\alpha = x_s/z_s$ and $\beta = ys/z_s$, and j denotes the slope geometry between the point source and object, and s represents a sampled wavelength weighted by the source power spectrum. Think of the sampled power spectrum as an additional wavelength dependent weighting term in sampled source spatial frequency distribution. Thus, a wider power spectrum has the effect of broadening the spatial frequency spectrum of plane waves in the illumination field. The illumination field of the physical system was assumed to behave as monochromatic, thus in proceeding LPDI image simulation examples the source is monochromatic at wavelength λ. A wider source spatial frequency distribution has been shown experimentally to have a significant effect on the resultant image by reducing phase object contrast. Simulated plane wave spatial frequency distributions for monochromatic, quasimonochromatic, and polychromatic cases are shown below in Figure 6.2.

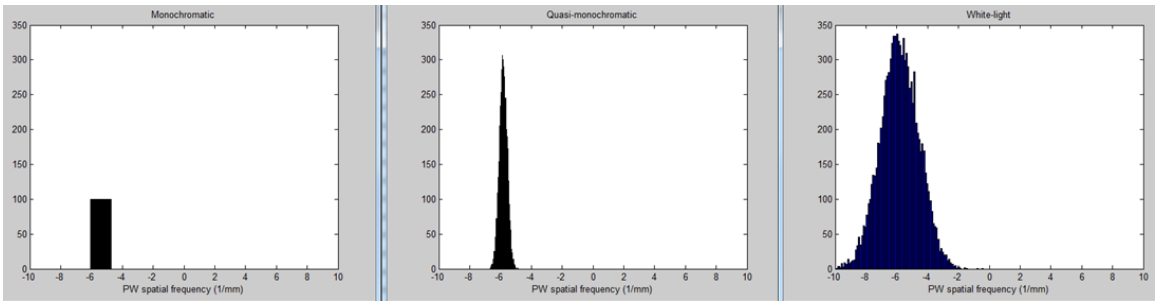

Figure 6.2: Plane wave distributions for three types of power spectrums

The left figure shows the spatial frequency distribution for a monochromatic source, the center figures shows the distribution for a quasimonochromatic (narrow spectrum) source, and the right figure shows the distribution for a white light source. Since the monochromatic distribution (left) does not have a spectral dependence, the plane wave distribution shape is defined by the geometric distribution of point sources, which is rectangular. The quasimonochromatic case has a spectral dependence, but has roughly the same bandwidth as the monochromatic case. However, the spectral dependence adds an additional weighting factor to the spatial frequency sampling governed by the source power spectrum, which influences the plane wave distribution causing it to take on the shape of the source power spectrum. The shape of the white light source distribution also takes the shape of the spectral distribution (white light halogen), but is much broader due to the broad power spectrum. The white light example shows how the power spectrum of the illumination makes the source effectively appear much broader.

The LPDI image simulation model led to the discovery of the primary differences between the new and old system LPDI systems (FICS1 and FICS2) that caused their disparate FPO sensitivities. The CCD installed in the FICS2 LPDI (the new system), was mistakenly switched to a monochromatic sensor. Thus, the source in FICS2 behaved with a much broader spatial frequency distribution, as shown by the white light distribution on the right in Figure 6.2 below. The broader source reduces FPO contrast because it requires a large x_{s0} to achieve the same 5% background level, which results in a spatial filter that renders phase objects with lower contrast.

6.5 Obtaining the Eigenterms Numerically

The P-operator is a 2D matrix that contains the collapsed set of discrete shifted transfer functions, $H_j(\boldsymbol{\rho}-\boldsymbol{\rho}_s^j)$. Recall that each plane wave in the source distribution shifts the pupil TF by spatial frequency $\boldsymbol{\rho}_s^j$. The P-operator is written as the matrix **P,** which contains $M{\cdot}N$ rows by N_s columns, where M and N are the number of rows and columns from the coherent pupil TF matrix. The P-vector is constructed numerically in three steps:

1) Shift the pupil matrix by $\boldsymbol{\rho}_s^j$

2) Convert the jth pupil matrix into a 1D vector with $M{\cdot}N$ rows using the stacking operator (described in Appendix A)

3) Insert this column vector in the jth row of the matrix **P**

Steps 1, 2, and 3, are repeated until $j = N_s$. Now, a numerical SVD[73, 74] function factors **P** into three matrices. This form of SVD is defined as $\mathbf{P} = \mathbf{UAV}^\dagger$, where **U** is an $M{\cdot}N$ x N_s unitary matrix, **A** is an N_s x N_s diagonal matrix with nonnegative real numbers along the diagonal (the singular values), and $\mathbf{V}^\dagger$ is an N_s x N_s unitary matrix with the symbol † (*dagger*) denoting complex transpose. The eigenvalues $\boldsymbol{\mu}_j$ are extracted along the diagonals of **A**, while the eigenvectors are extracted from each row of $\mathbf{V}^\dagger$. The inverse stacking operator (described in Appendix A) converts the eigenvectors into eigenmatrices, $\boldsymbol{\Phi}_j(\boldsymbol{\rho})$. In summary, the eigenvalues $\boldsymbol{\mu}_j$ and the eigenmatrices $\boldsymbol{\Phi}_j(\boldsymbol{\rho})$ were obtained by factoring the P-operator using the SVD function in MATLAB™, so they can compute the image using only a few dozen eigenterms by evaluation of Eq. 6.3.

6.6 LPDI Linescan Blurring

Linescan imaging has an additional blurring effect on the image that the partially coherent image simulation algorithm defined in Eq. 6.2 does not account for. This blurring effect can be added to the image simulation code by convolving the simulated image irradiance with an amplitude transmission mask slit, which represents the linear image sensor. The linescan blurred image is obtained using the following filter

$$E_{blur}(\mathbf{r}') = E_{pcoh}(\mathbf{r}') * \mathrm{rect}\left(x / w_x \right), \tag{6.4}$$

where rect() represents a rectangle function of infinite length in the y-direction with width equal to w_x, which is the image sensor pixel size in the image sensor in the x-direction. This convolution operation is analogous to a low-pass filter with sinc($w_x \cdot \xi$) amplitude transmission dependence.

CHAPTER 7. LPDI IMAGE SIMULATION RESULTS

In this Chapter, the LPDI image simulation code will be evaluated by comparing simulated and measured LPDI images. Simulated LPDI images were generated by directly inputting high-resolution PSDI phase measurements of actual phase objects into the simulation code. Two sources of phase objects participated in this evaluation:

1) Fabricated Gaussian surface bumps engineered in varying heights. The measured and simulated images are compared in Sections 7.3 through 7.5.

2) An assortment of FPOs found on NIF optics during production FICS inspection. Measured and simulated images are compared in Sections 7.6 through 7.9.

7.1 Simulation Inputs

The simulation code inputs are the LPDI imaging system parameters and the object's PSDI measured phase. The code outputs simulated images in two formats, a full-resolution image generated from the native PSDI pixel size, and a down-sampled image intended to mimic image sensor sampling based on the sensor's physical pixel size. Image simulation accuracy was evaluated by qualitatively comparing the measured and simulated 2D images with the aide of horizontal and vertical lineouts, and quantitatively compared using the image analysis metric P_{max} (image maximum pixel value). The image simulation code does not generate images in physical units of irradiance. It instead produces images in units of *relative* irradiance. Therefore, the pixel values of simulated images were scaled post facto, on a consistent relative basis to match the pixel values of measured images to facilitate qualitative comparison of their relative image contrasts.

A simulation code that outputs images in units of absolute irradiance is desirable (and may be pursued in the future). However, quantitative images were not required for this application since images of phase objects were compared relative to each other to optimize image contrast of known failing flaws. Simulated images were found to be in good agreement with the measured images. However, some notable differences warranted discussion. Relevant portions from the image simulation code written in MATLAB™ are available for review in Appendix B.

7.2 LPDI Image Simulation Parameters

Simulated LPDI images were produced by inputting the measured PSDI phase of each object into the simulation code. Image simulation parameters were set to match the physical system, as summarized below in Table 7.1. Distances are based on physical measurements of the real system. A heptagonal pupil shape was used for the imaging system transfer function to model the actual seven-bladed aperture in the physical lens. The code produces the P-operator by homogeneously random sampling a monochromatic source distribution in frequency space. In section 6.4, we showed that a monochromatic source produces roughly equal bandwidth to the actual narrow spectral bandwidth (quasimonochromatic) source, because the physical source width term (`wx`) dominates compared to the quasimonochromatic spectral bandwidth. The effects of the quasimonochromatic spectral weighting term on the shape of the spatial frequency distribution was evaluated and determined to be insignificant for this application and for this number of source samples (`Ns`=256). Thus, for this image simulation the source is

monochromatic, and the distribution was numerically generated based on a constant λ and the extent of the physical source area (wx and wy).

Source width were measured previously in Chapter 4 to be 0.4mm wide (wx) and 812mm high (wy). In the model, the source distribution was assumed to have infinite extent in the vertical direction. In the simulation, the source distribution extends between the positive and negative Nyquist frequencies in the vertical axis, and has finite bandwidth in the horizontal axis (as defined by parameter wx), as illustrated previously in Figure 6.1. The random sampling of the source distribution has the consequence of producing a slightly different P-operator for each simulation run, even if the imaging parameters in Table 7.1 are constant. This means the eigenterms and images do not repeat exactly from ideally set-up one simulation run to the next. For the number of sample used in this example, these random changes in the simulated image due to random sampling of the source distribution were evaluated and determined to be inconsequential.

Table 7.1: Image simulation parameters

Parameter	Value	Description
Ns	256	Number of sources
Neig	Ns	Number of eigenterms
xs0	-2.5	Source offset, x-direction
ys0	0	Source offset, y-direction
zs	550	Source to object
wy	∞	Height of source
wx	0.4	Width of source
lm	5.50E-04	Wavelength
fnum	16	F-number
feff	210	Effective focal length
D	feff/fnum	aperture diameter
p	1450	Object to lens
q	213	Lens to image plane

px	0.009	Pixel size
type	'hept'	Aperture shape

7.3 Gaussian Phase Objects

An array of Gaussian shaped amorphous silica surface bumps of various heights were fabricated onto a 2" diameter fused silica test sample by laser-assisted chemical vapor deposition (LVCD) of Tetraethyl orthosilicate (TEOS). The sample was prepared at the Advanced Optical Damage Mitigation Development Laboratory by Selim Elhjad. Details of the LVCD deposition process will be published elsewhere, but a brief description of this process is included in Appendix C.

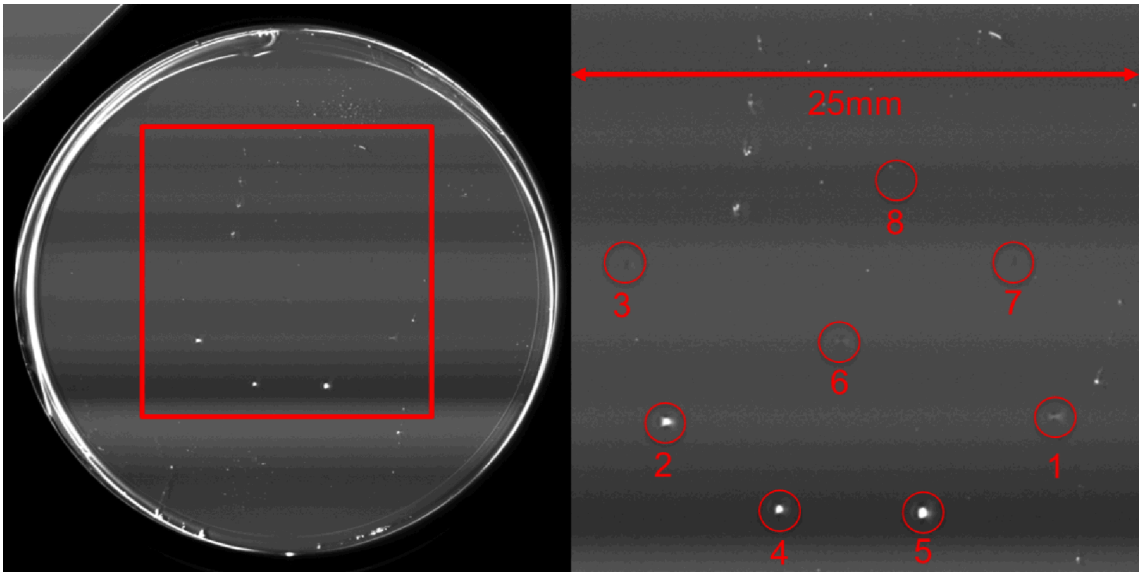

Figure 7.1: LPDI map of 2" Gaussian bump test sample showing 8 sites

Cropped LDPI image of the 2" diameter LCVD deposited Gaussian bump sample. The boundary of the optic and mount is visible in the 50mm FOV image (left). The 25mm FOV crop (right) labels the site locations (labeled 1 through 8). The red square in the 50mm crop correspond to the FOV of the 25mm crop.

The 2” Gaussian bump sample was imaged by LPDI on the production FICS system. Crops from this image are in Figure 7.1, along with numbered site names (1 through 8) labeled on the image. Following LPDI imaging, the phase of each bump was measured in transmission by PSDI. The measured phase of all sites are shown below in Figure 7.2. Peak-to-valley (PV) OPD varied between -20nm and 1532nm, and the full-width at half maximum (FWHM) of the bumps was consistently ~250µm.

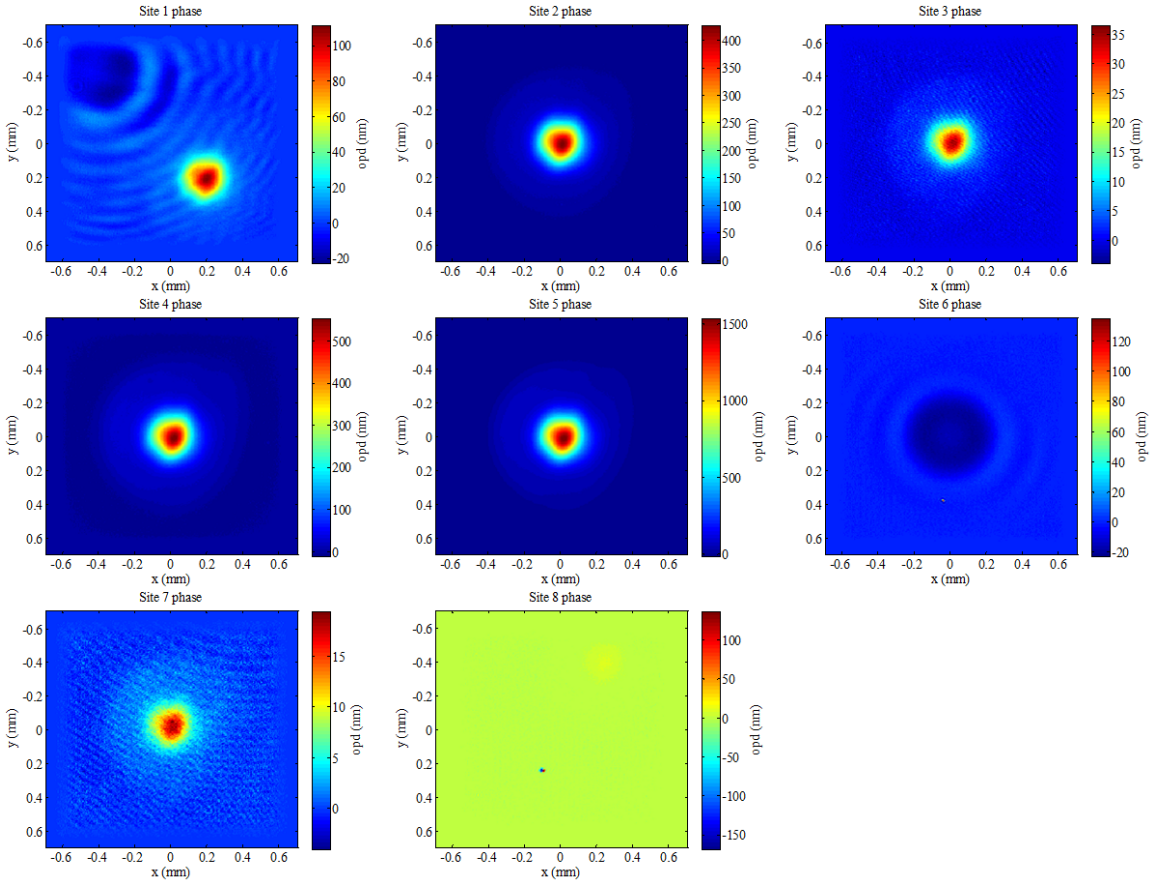

Figure 7.2: PSDI measured phase Gaussian objects

7.4 Gaussian Phase Object Imaging Simulation

Measured and simulated images of the Gaussian shape bumps are shown below in Figure 7.3 and Figure **7.4**, along with associated horizontal line profiles in Figure 7.5.

The image analysis metric, P_{max} for the measured and simulated images are listed in Table 7.2 and plotted in Figure 7.6. Modeled images are in units of relative pixel value. To aid relative comparison of the modeled and measured images, modeled image line profiles (in Figure 7.4), were scaled by a consistent multiplicative factor and background value was added to each image line profile.

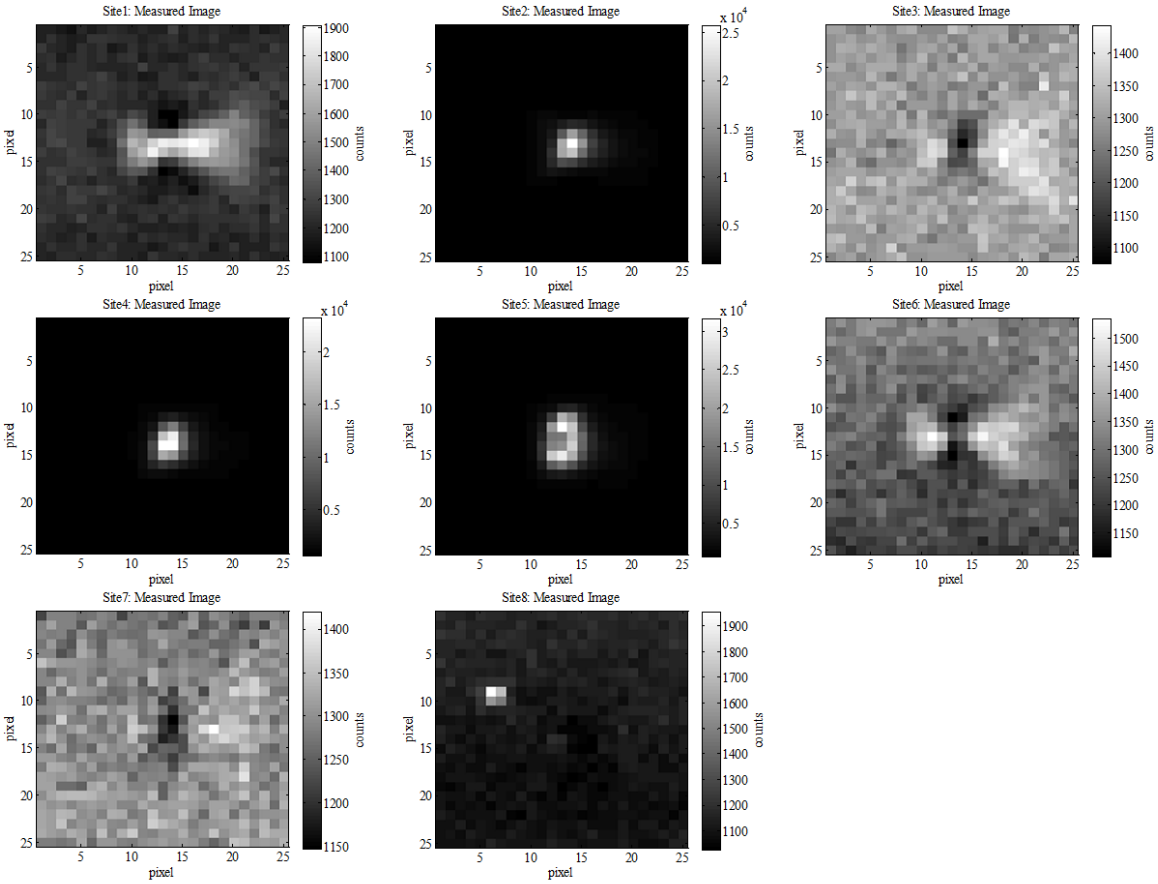

Figure 7.3: Measured LPDI image of Gaussian bumps

Weak phase objects are visible in the measured image as a slight deviation in the background.

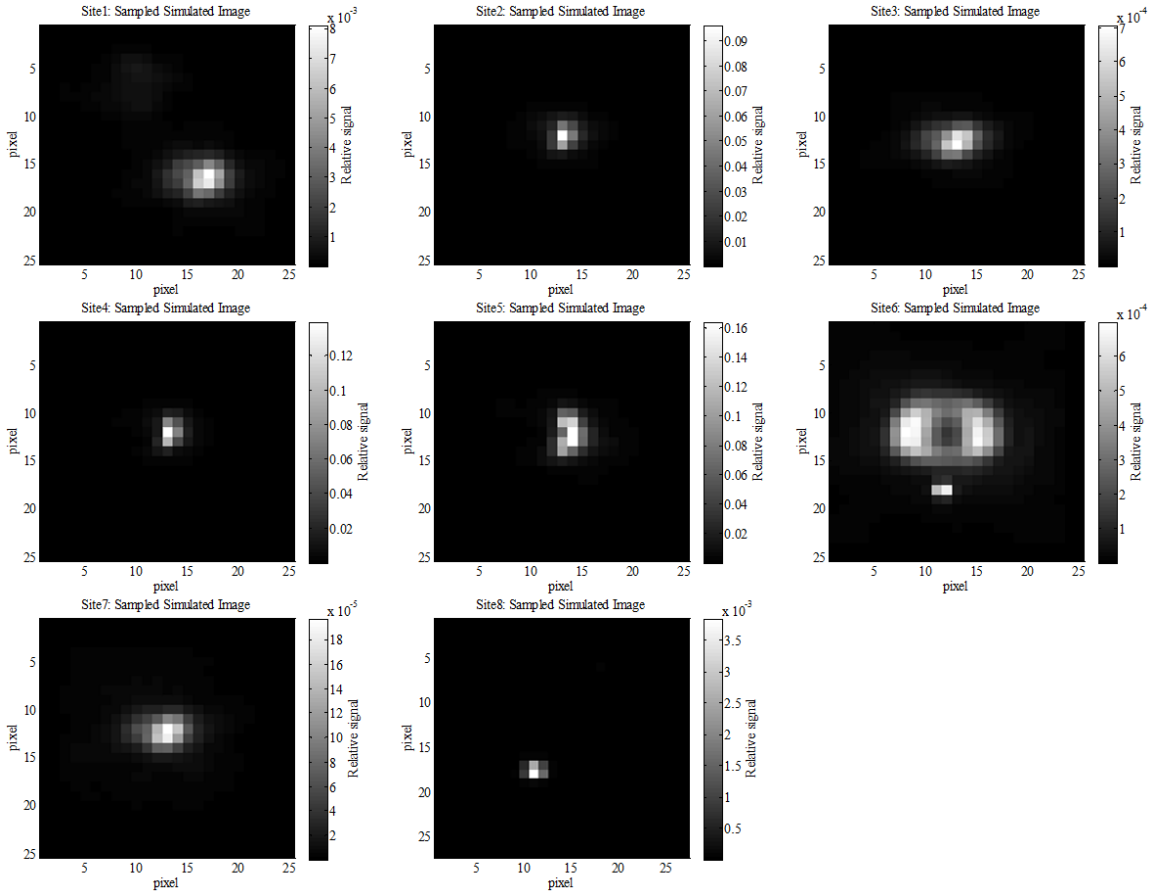

Figure 7.4: Simulated LPDI images of Gaussian bumps

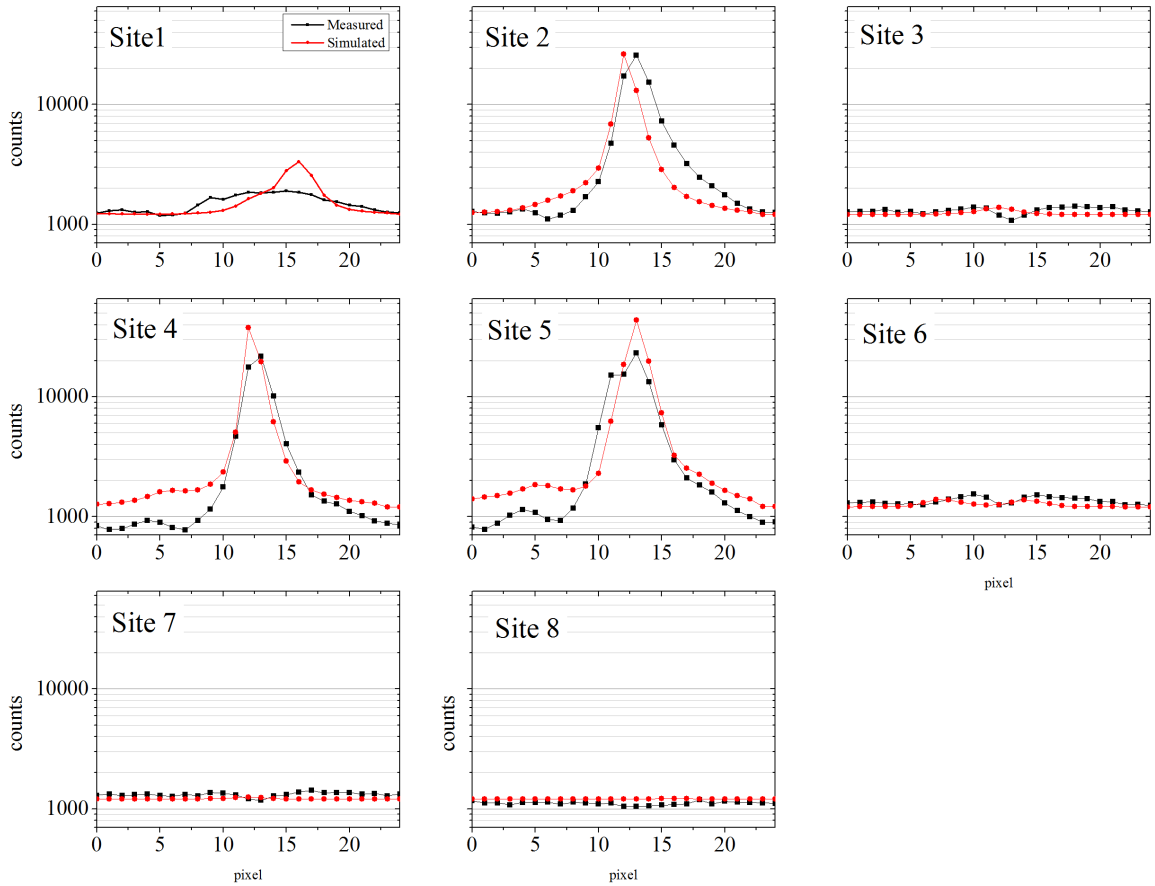

Figure 7.5: Gaussian bump line profiles, Measured vs. Simulated

Table 7.2: Gaussian Bumps, P-V opd, and P_{max} (measured vs. simulated)

Site Name	P-V opd (nm)	P_{max} (meas.)	P_{max} (sim.)
6	-20	1536	1384
8	10	1188	1216
7	23	1420	1252
3	46	1408	1384
1	133	1908	3324
2	428	25752	26372
4	557	21740	37792
5	1532	23228	43752

7.5 Gaussian Bump Comparison Discussion

Simulated and measured LPDI images of the Gaussian bump showed acceptable qualitative agreement. However, measured images exhibited more blurring, especially for P-V opd > 400nm, possibly due to lens aberrations. Aberration blurring was expected because the object was imaged at the edge of the field (~38mm image height), where blurring from field-dependent aberrations, coma, astigmatism, and field curvature—are significant. These aberrations are apparent in the lens manufacture published modulation transfer function (MTF) data, where object spatial frequency corresponds to ~30 lp/mm (image space), see Figure 3.8. Aberration blurring could be added to the image simulation code by incorporating a phase term in the pupil matrix[72], as described in Section 5.9. However, modeling a phase dependent pupil would require a complex floating-point pupil matrix, which requires significantly more computer memory and slows computation. For this reason, a numerical type *logical* (binary) P-operator matrix was used in MATLAB™. Figure 7.6 shows the P_{max} values of the measured and simulated images, and their ratios vs. P-V OPD. The P_{max} ratios are near one for OPDs equal to or less than 133nm (Site 1), meaning measured and simulated P_{max} values agreed. This close agreement occurred because these are low contrast phase objects, which are visible as a perturbation in the background illumination. The P_{max} ratio increased to ~1.75 for sites of OPD greater then 133nm, meaning the simulated images reported a greater P_{max} signal.

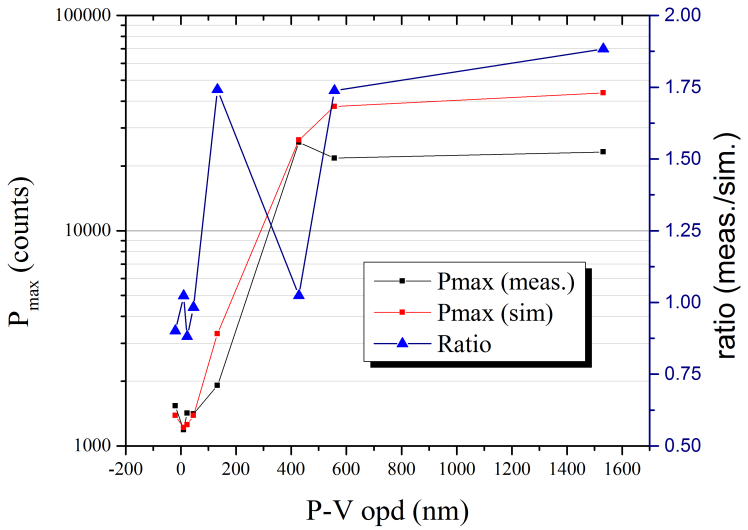

Figure 7.6: P-V opd vs. P_{max} & Ratio for Gaussian bump objects

7.6 FPO Flaw Set

To evaluate LPDI image simulation accuracy on real-life fratricidal phase objects (FPOs), a subset of 12 test flaws was assembled to represent a sampling of typical flaw morphologies from the set of 18,000+ failing FPOs identified by FICS since December of 2007. All 18 flaws were identified and characterized by FICS production processing consisting of LPDI mapping following by PSDI hit list imaging and propagation-based damageability calculation (FOAQual), as described in Chapter 3. Flaws were assigned capital letter names: A through L, see Table 7.3. PSDI phase maps of each flaw are in Figure 7.7, along with corresponding horizontal and vertical line profiles in Figure 7.8.

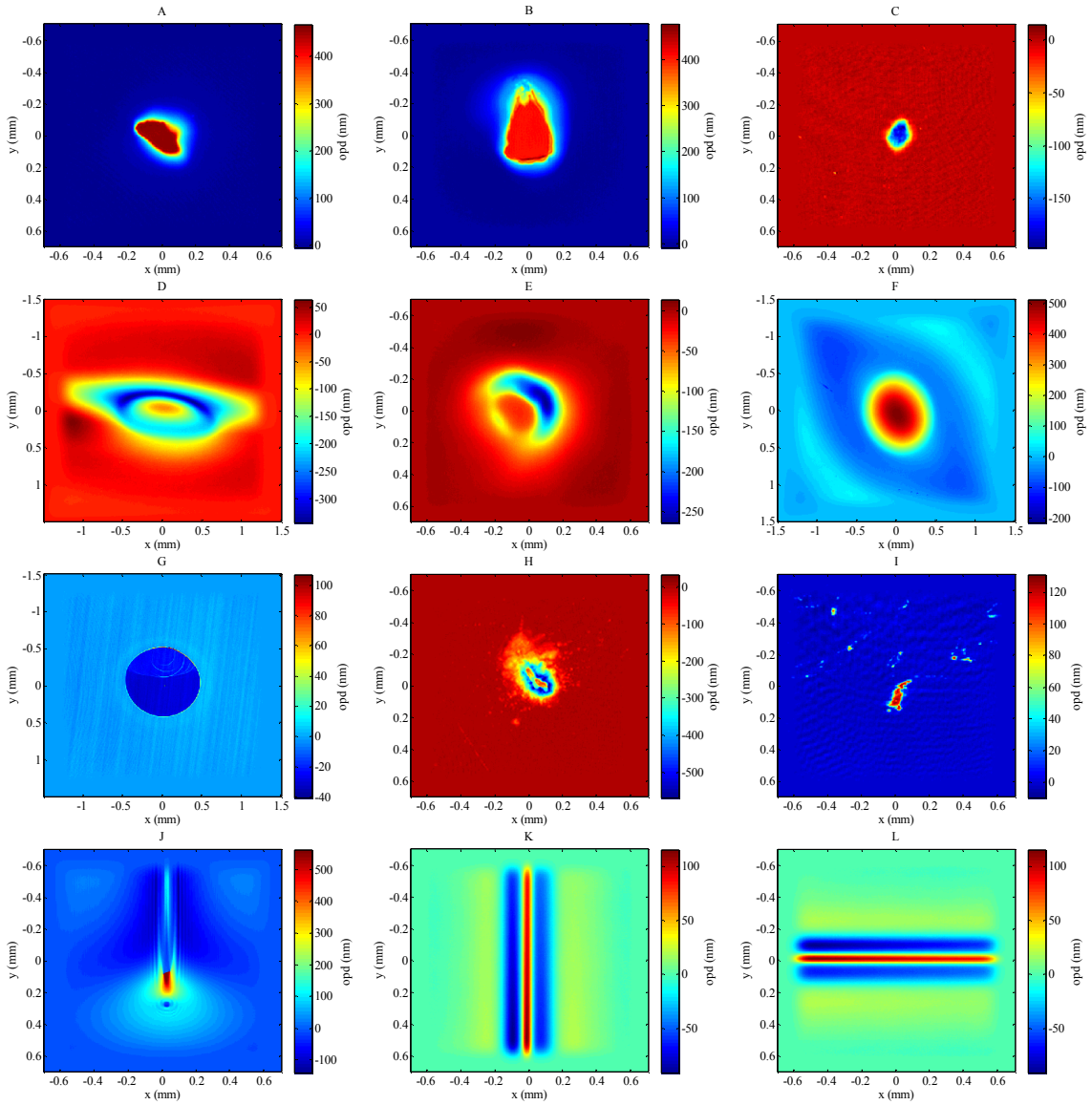

Figure 7.7: PSDI measured flaw phase (opd)

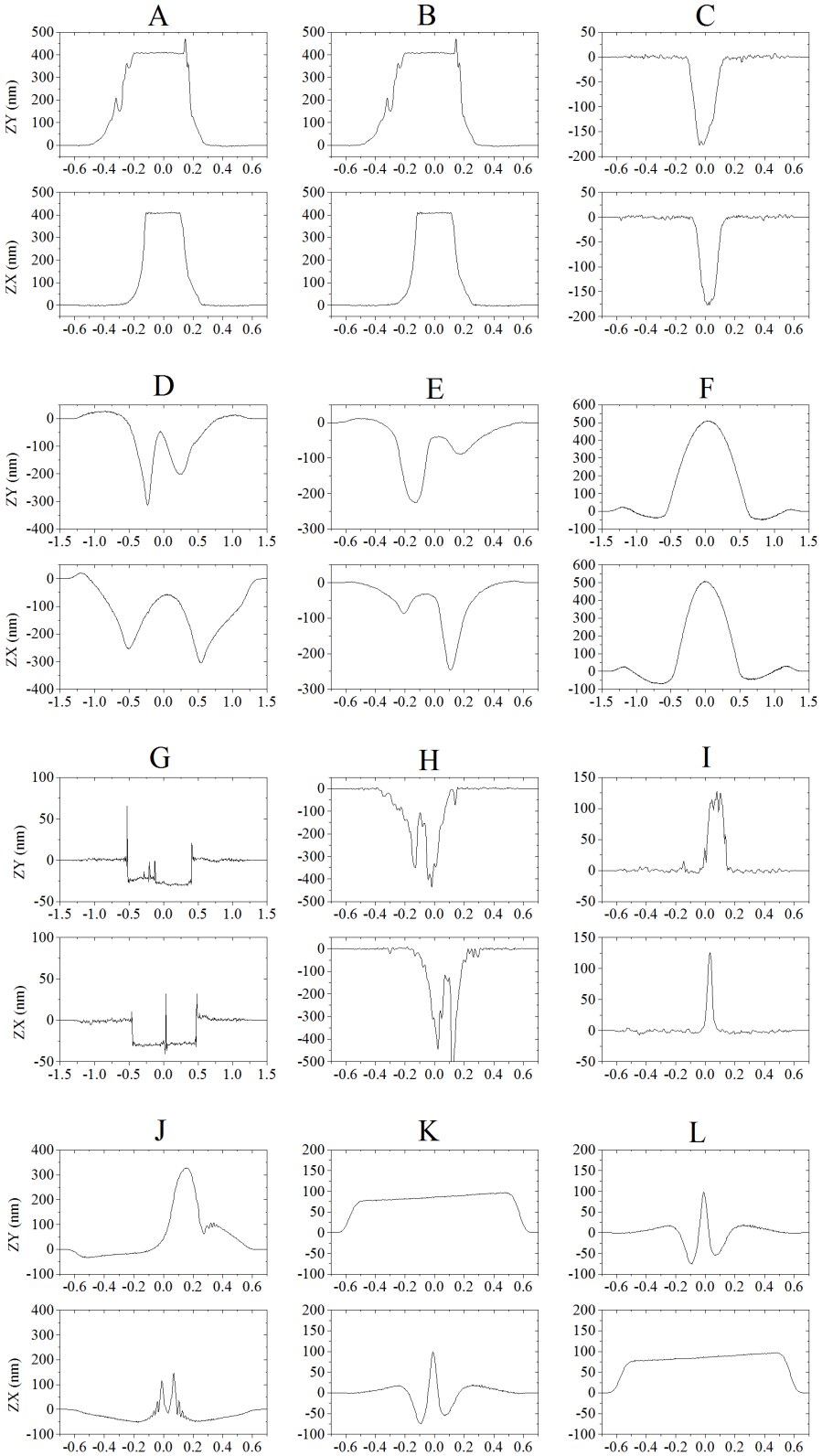

Figure 7.8: Flaw Horizontal (ZX) and Vertical (ZY) OPD Profiles

Table 7.3: Flaw descriptions and metrics

Name	Type	OPD	Description	Optic Type†	x (pixel)	y (pixel)	Pmax	SumInt	PV OPD (nm)	Vol. OPD (nm-mm^{-1})	<N>max	Ipk
A	Continuous and Discontinuous	Positive	mesa[1]	TCVW	2497	4704	19014	131178	461	26.7	0.365	37.57
B	Continuous and Discontinuous	Positive	mesa[1]	TCVW	2169	6931	17559	323662	481	56.7	1878.32	19.4
C	Continuous and Discontinuous	Negative	shallow site[2], exit	oWFL	3746	2602	7478	51268	210	-2.87	0	5.4
D	Continuous	Negative	AMP pit[3]	oWFL	4597	7497	10498	100284	463	-218	13.177	14.88
E	Continuous	Negative	AMP pit[3]	oWFL	804	6079	14375	28645	276	-30.4	1.933	72.12
F	Continuous	Positive	AMP pit[3]	oWFL	2034	4521	16375	331551	736	107	26.58	207.24
G	Discontinuous	Negative	FLRT[4]	THG	3299	4851	3732	N/A	146	-16.7	0	5.3
H	Discontinuous	Negative	Shallow site[2], input	oWFL	4369	5672	31870	238558	515	-1.63	2.4	23.6
I	Discontinuous	Positive	Stain[5]	GDS	6144	7134	9190	27373	140	1.45	0.322	12.2
J	Continuous and Discontinuous	Positive / Negative	MRF sleek[6]	CPP	2886	4656	31204	102310	665	10.6	0.106	12.15
K	Symmetrical, Continuous	Negative	MRF sleek[6]	CPP	3654	4261	36123	123191	240	-2.12	8.78	0.017
L	Symmetrical, Continuous	Negative	MRF sleek[6]	CPP	4752	5107	1204	10210	240	-2.12	8.78	0.017

1: Flat topped bump on the surface generated during ion figuring by surface contamination serving as resist
2: Phase object generated by laser interaction with metallic contaminant (e.g. plasma etch) [32]
3: Differential etch caused by material inhomogeneity, material stress, or chemical contaminant[50]
4: AR sol gel film removed by the flaw removal tool [18]
5: Flat topped bump on the surface generated by etchant resist (surface contaminant)[50]
6: Magnetorheological finishing (MRF) generated by fluid-particle interaction [75]
†: TCVW (Target Chamber Vacuum Window), oWFL (off-axis Wedged Focus Lens), THG (Third Harmonic Generator), GDS (Grating Debris Shield), CPP (Continuous Phase Plate

The flaws in Figure 7.7 and Figure 7.8 are grouped by row according to spatial frequency content. Low spatial frequency flaws require manual inspection, because they render as a low contrast variation in the LPDI image background, therefore the LASNR algorithm cannot detect them, see Section 3.9. In row 1 (**A**, **B**, **C**), the flaws are classified as hybrid phase objects, containing a mix of high and low spatial frequency content. In Row 2 (**D**, **E**, **F**), the flaws are classified as low spatial frequency phase objects due to their smooth continuous phase. In Row 3 (**G**, **H**, and **I**), the flaws are classified as high spatial frequency phase objects due to significant phase discontinuity. Finally, in Row 4 (**J**, **K**, **L)**, the flaws are classified as low spatial frequency phase objects with mirror symmetry. Note: Flaws K and L are the same—Flaw K is the same as Flaw L, but rotated 90° counter-clockwise. The rotated flaw will demonstrate the effect of object symmetry.

7.7 Measured LPDI Images

Measured LPDI images of the Flaws A through L are in Figure 7.9, cropped from images captured during production processing. Since these images were taken over a ~4 year span (December 2010 to September 2013), some image-to-image variability occurred. Their image backgrounds variability fell within the acceptable range (800 to 1200 pixel value or 1.2% to 1.8% grey value). Flaw L and K are the same, but for Flaw K, the entire optic was rotated 90° CCW.

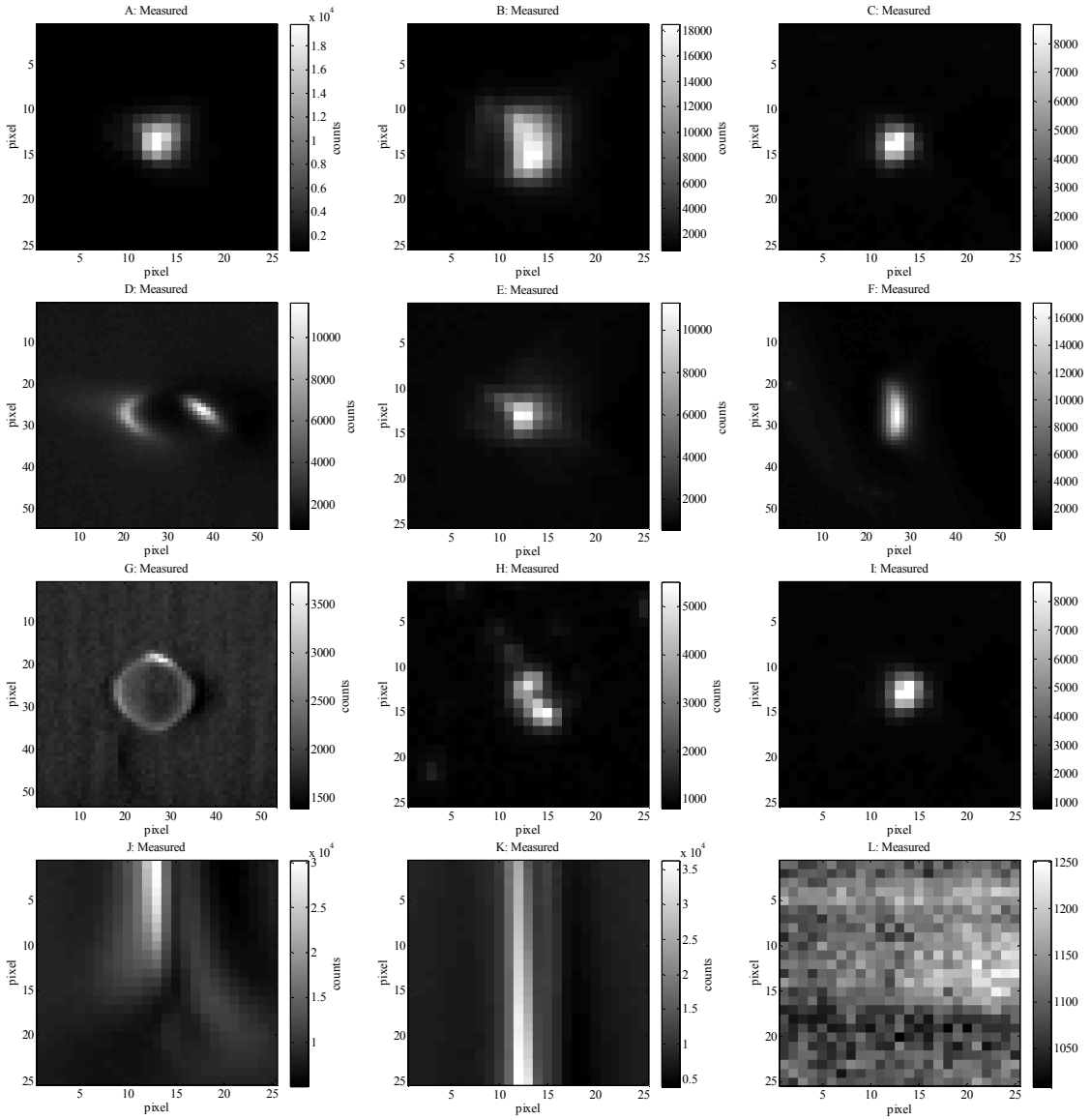

Figure 7.9: Measured flaw images

7.8 Simulated Images

Simulated LPDI images of Flaws A through L were generated using identical image simulation parameters as were used for the Gaussian bumps objects, see Table 7.1. Simulated images are in Figure 7.10. Flaws A through L were analyzed using a similar process to the Gaussian objects. Image line profiles were scaled to normalize them to the measured images for qualitative comparison by adding a constant background value and

scaling them with a multiplicative factor. These constants were allowed to vary for each image to track measured image variability. Horizontal and vertical profiles of measured and simulated images and plotted together below in Figure 7.11 for qualitative comparison. The image analysis metric P_{max} for measured and simulated images are listed below in Table 7.4 and plotted in Figure 7.12.

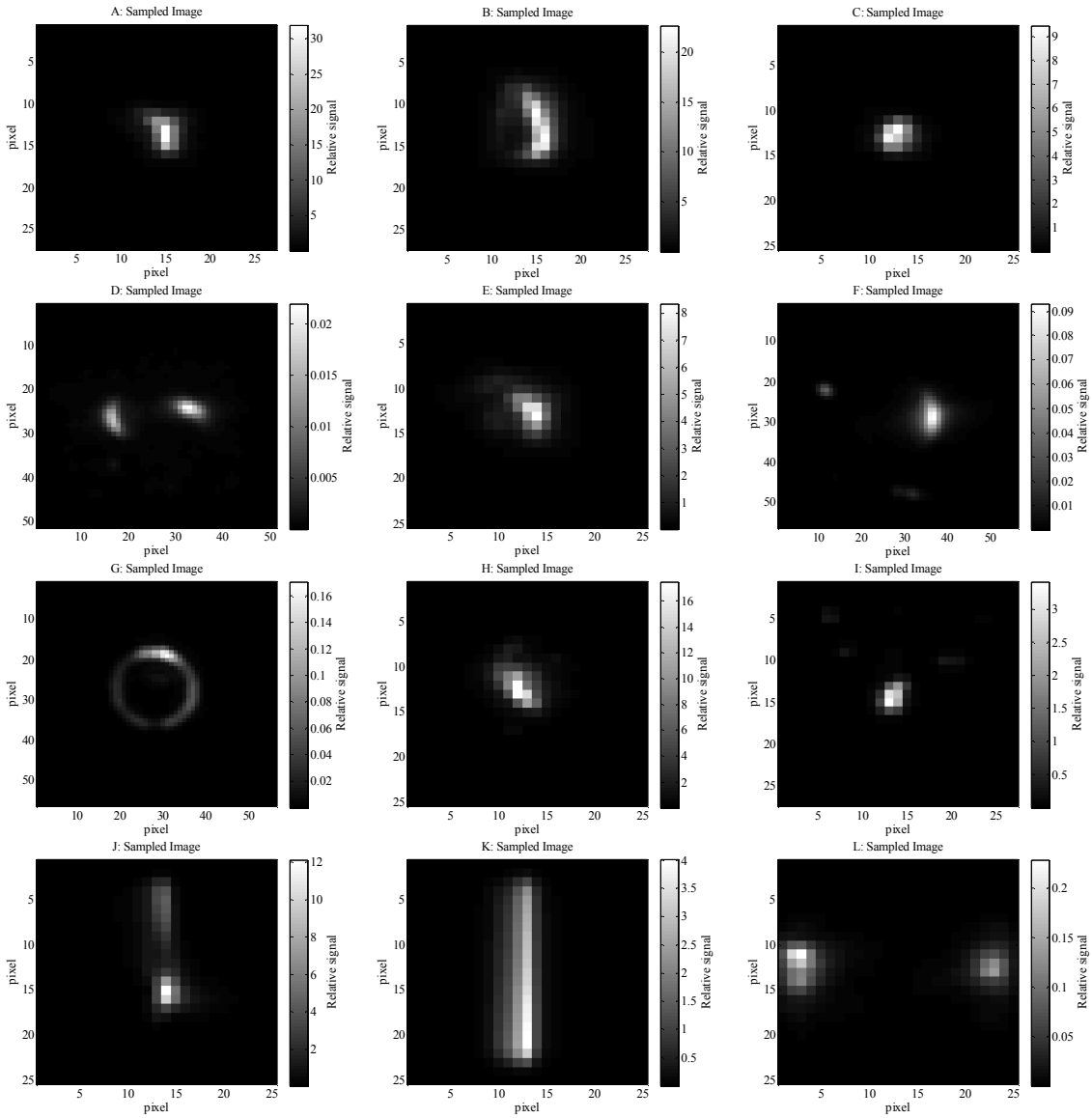

Figure 7.10: Simulated flaw images

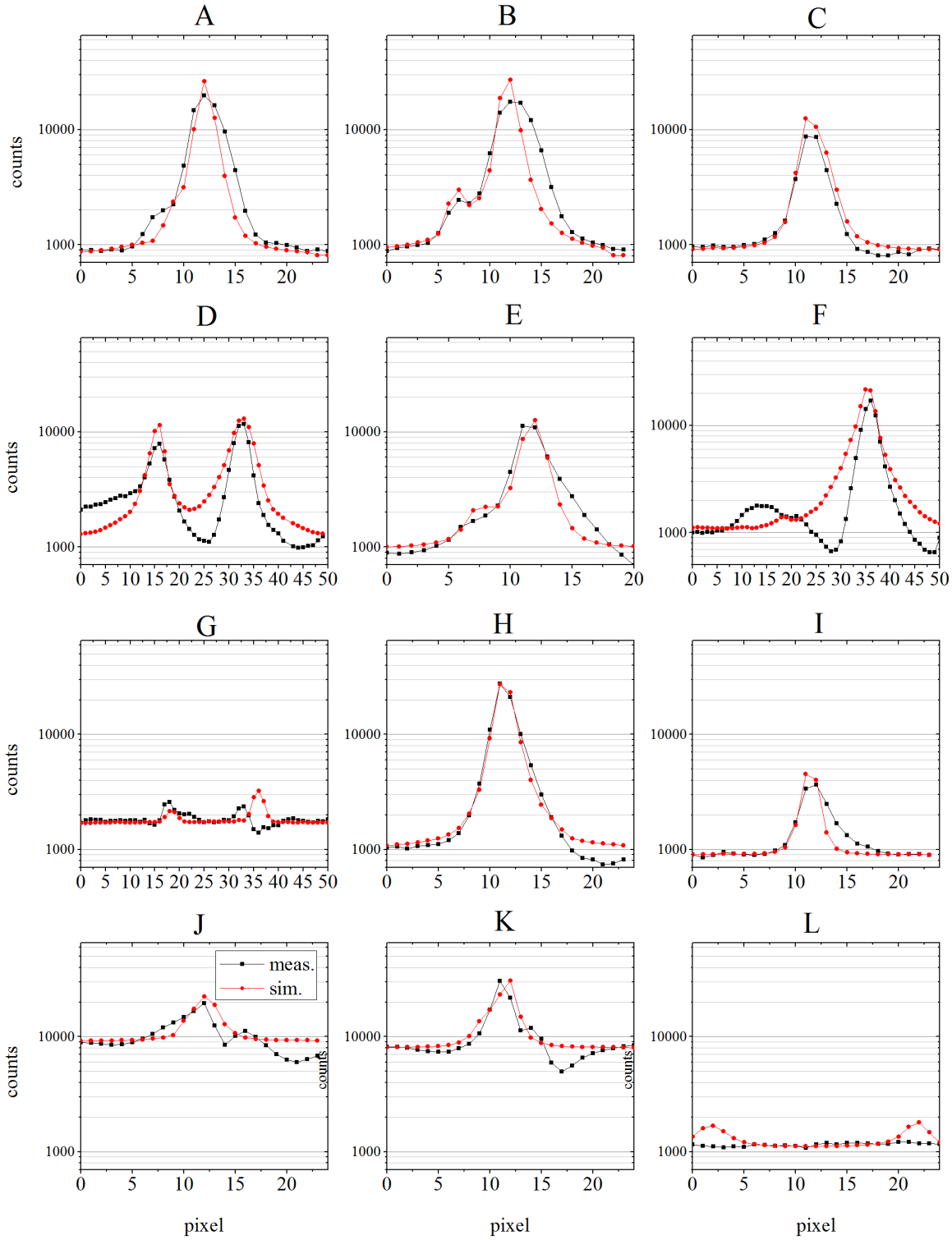

Figure 7.11: Horizontal profiles of measured and simulated flaw images

Table 7.4: Flaw Pmax: Measured vs. Simulated

Name	Measured Pmax	Simulated Pmax	% Error
A	19014	26325	38%
B	17559	27161	55%
C	7478	12470	67%
D	10498	12974	24%
E	14375	12582	-12%
F	16375	21670	32%
G	3732	3236	-13%
H	31870	27211	-15%
I	9190	4508	-51%
J	31204	22333	-28%
K	36123	30763	-15%
L	1204	1793	49%

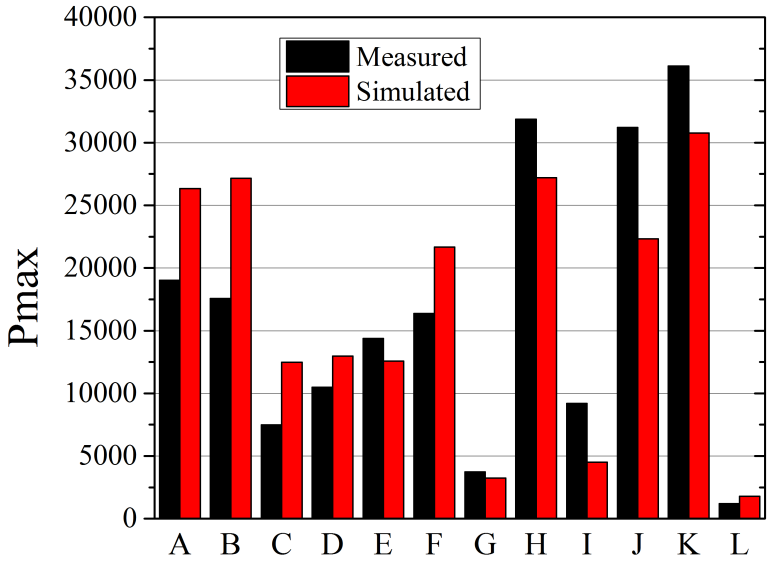

Figure 7.12: Flaw P_{max}, Measured vs. Simulated

7.9 Flaw Set Results Discussion

Simulated LPDI images show good qualitative agreement with the measured images as illustrated by the line profiles in Figure 7.11. The primary difference between

the measure and simulated images is at small signal level (near background). Measured images, particularly Flaws D and F decreased to below the background level, whereas the simulated images stay above image background. This difference indicates that this image simulation does not accurately model low spatial frequency phase objects that appear in the image background at the small signal level. However, at large signals the simulated images show excellent agreement as demonstrated comparison with the image analysis metric P_{max}. The P_{max} mean percent difference was 11% with a sigma of 38%. Simulated images had higher P_{max} on average. The magnitude of the mean P_{max} percent difference was 33%. This result of higher simulated P_{max} is consistent with the Gaussian bump result, and could be the result of lens aberrations in the measured system causing object blur, which is unaccounted for in the simulation code.

CHAPTER 8. DISCUSSION

8.1 Examination of LPDI Eigenterms

The eigenmatrices $\mathbf{\Phi}_j(\boldsymbol{\rho})$ represent the LPDI system transfer function, just like the coherent transfer function $H(\boldsymbol{\rho})$ example from Figure 5.3. We conceptualized this coherent transfer to represent the lens entrance pupil, which collects plane waves over a range of spatial frequencies as given by the geometry of the lens entrance pupil. However, when the LPDI eigenmatrices are displayed graphically, a casual glance at their chaotic shape reveals them to be nothing more than an abstraction. Yet they completely characterize the LPDI system and are able to calculate faithful simulations of LPDI images, as demonstrated by the examples from Chapter 7.

In the context of satisfying a curiosity, we attempted to find some semblance of order in these LPDI eigenmatrices, with the intention to develop some insights into their shapes so one could conceptualize the LPDI system transfer function similarly to the analogy drawn between the coherent TF and lens pupil. With this purpose in mind, eigenmatrices for an LPDI system with a square pupil were computed. A square pupil was used since the eigenmatrices produced from a circular or heptagonal pupil (see examples from Chapter 7) take on shapes that are more complex. However, the eigenmatrices produced by a square lens pupil would seem to collapse into a simple sinusoidally oscillation along in η-axis, which is masked by a slit η_{sw} wide and shifted by ξ_o (parameters defined in Section 6.3).

Figure 8.1 show the first four terms (j = 1, 2, 3, and 4) of the eigenmatrices ($\mathbf{\Phi}_1$, $\mathbf{\Phi}_2$, $\mathbf{\Phi}_3$, and $\mathbf{\Phi}_4$). These eigenmatrices represent amplitude transmission masks (transfer functions) that operate on the object transmission function T_{obj} independently in irradiance. Each mask $\mathbf{\Phi}_j$ is weighted by the square of the eigenvalue $\boldsymbol{\mu}_j$. Plotted below in Figure 8.2 is the first 25 eigenvalues normalized to a value of one, along with the non-zero part of the first 25 eigenmatrices, i.e. a line profile along the η-axis for each $\mathbf{\Phi}_j$, up to j = 25. The sinusoidal oscillation of the eigenmatrices means they contain negative amplitude values, which could be interpreted as a $\pi/4$ phase shift. Beyond some simplistic observations, it is unclear how to conceptualize these functions at this time.

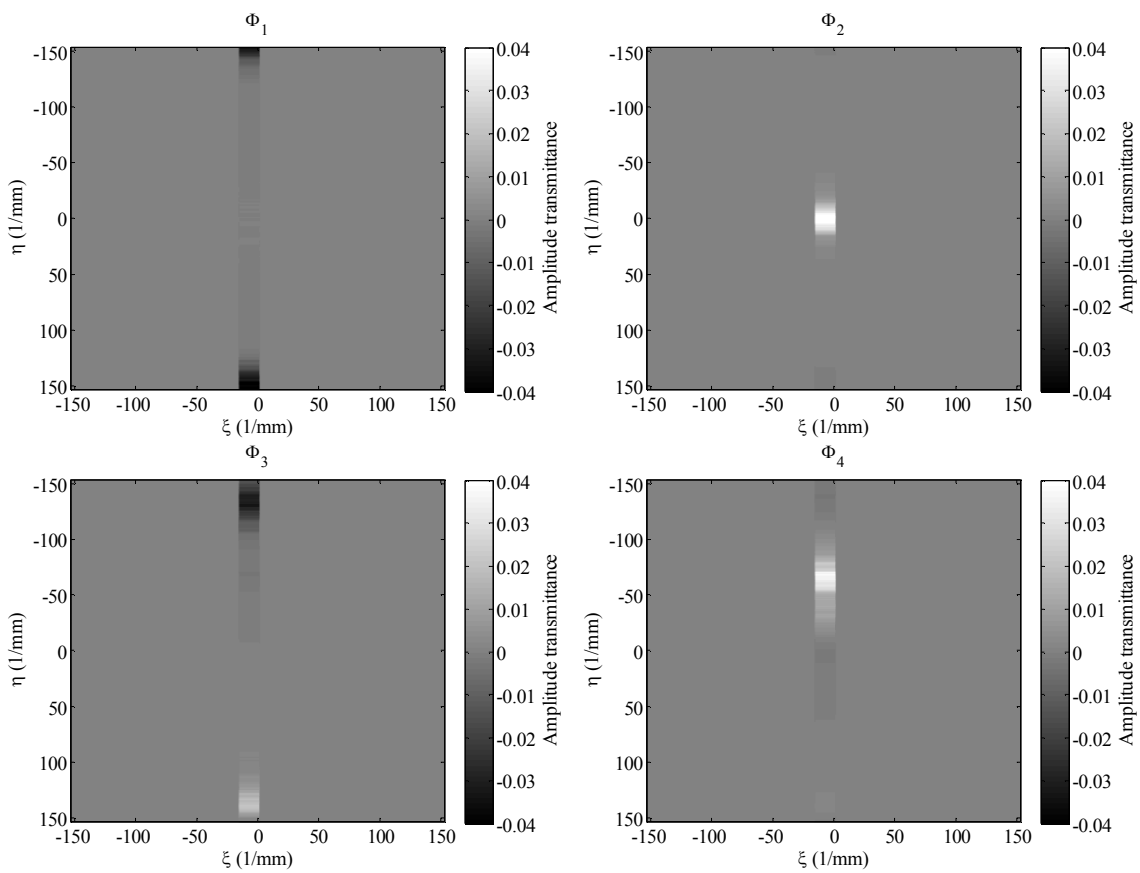

Figure 8.1: First four eigenmatrices of an LPDI system with a rectangular pupil

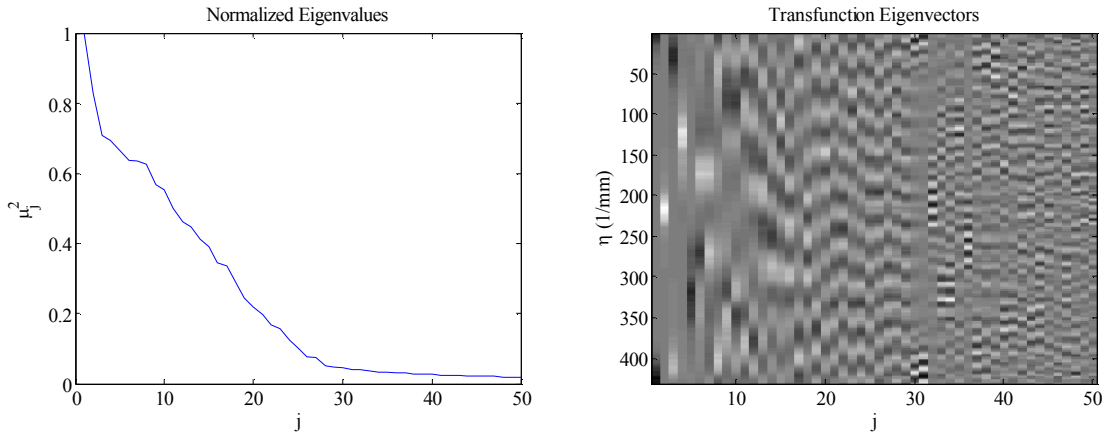

Figure 8.2: First 50 eigenvalues and non-zero part of the eigenmatrices

8.2 Singular LPDI Transfer Function

An attempt was made to simulate LPDI image from a single transfer function. This approximated transfer function was constructed by summing the eigenvalues squared multiplied by the magnitude of the eigenmatrices, i.e. $H(\boldsymbol{\rho}) \sim \Sigma|\boldsymbol{\mu}^2\boldsymbol{\Phi}(\boldsymbol{\rho})|$. The singular TF and the image it produced are shown below in Figure 8.3. The resulting image appears quite different from the measured image of Flaw A in Figure 7.9 and is also quite different from the simulated image computed by Eq. 6.3. Thus, this attempt at creating a singular transfer function of the LPDI system did not succeed. This suggests that the set of eigenmatrices must be evaluated independently to construct a simulated LPDI image.

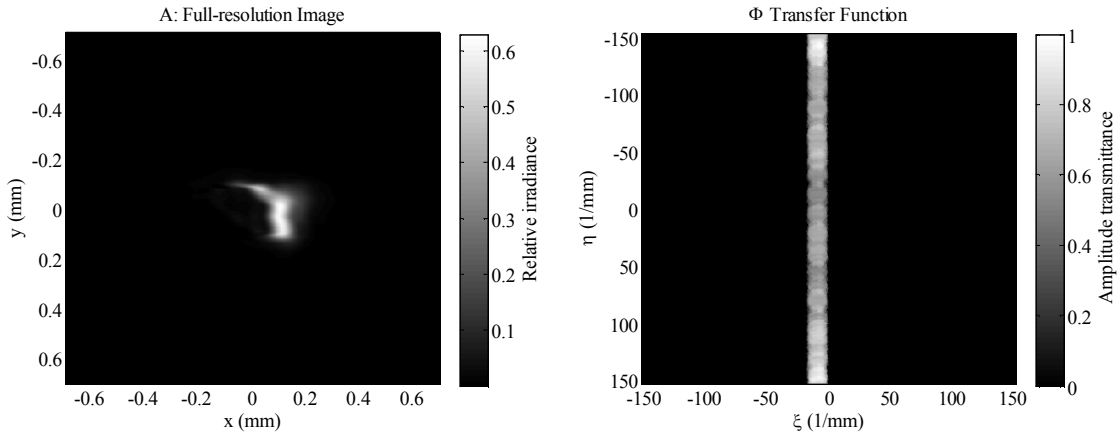

Figure 8.3: Simulated image of Flaw A produced from a single TF

8.3 Heuristic Phase Extraction

A phase extraction algorithm was developed as an attempt to extract phase information from an LPDI image by numerical integration of the image signal along the scan direction. This signal processing method was based entirely on the observation that the phase of the object appears to be proportional to the first derivative of the object's phase along the scanning direction (x-axis)—hence *heuristic phase extraction*. On this basis, numerical integration of the image may yield useful quantitative phase information in the object as performed in the frequency domain

$$t_{obj}(\mathbf{r}) \propto \kappa \mathbf{F}_{\boldsymbol{\rho}}^{-1}\left\{\frac{1}{i\xi}\mathbf{F}_{\mathbf{r}}\left\{E_{pcoh}(\mathbf{r})\right\}\right\}, \tag{8.1}$$

where the factor $-i/\xi$ multiplied by the forward Fourier transform of the LPDI image signal E_{pcoh} performs integration in the frequency domain. An inverse Fourier transform of this result is intended to recover the phase of the object $t_{obj}(\mathbf{r})$, after multiplication by an appropriately selected (but as of yet unknown) scaling factor or transfer function κ.

The Continuous Phase Plate (CPP) is a smoothly varying phase plate inserted into the NIF beam prior to the final focus element that shapes the laser spot. The smoothly varying phase of the CPP is an ideal object to test the phase extraction concept outlined by Eq. 8.1. The LPDI image of a CPP optic in Figure 8.4 clearly shows the smooth phase variation in the image background. This image was transformed into a phase signal using an algorithm based on Eq. 8.1. The resulting phase of this CPP extracted from the LPDI image can be compared with the interferometer measured result in Figure 8.5. The LPDI extracted phase compares favorably to the interferometer result—at least in the crudest qualitative sense, as indicated by the arrows pointing to corresponding structures in the two images. This comparison demonstrates the concept of quantitative phase extraction of an LPDI image. A different approach, such as numerical inverse transformation (e.g. Land-Webber iteration), may yield more accurate phase information. Regardless of the algorithmic approach, a more uniform LPDI illumination source is probably necessary to eliminate visible structure in the phase extraction.

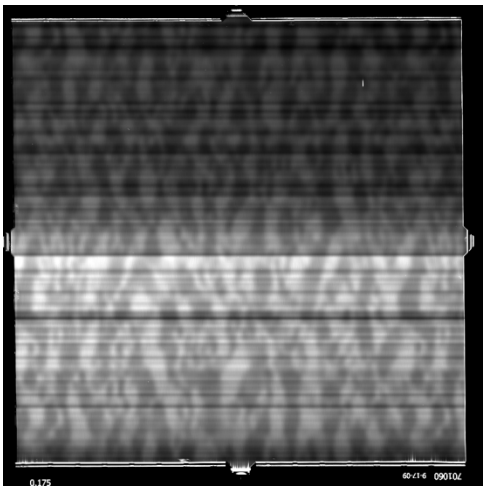

Figure 8.4: LPDI image of a Continuous Phase Plate (CPP)

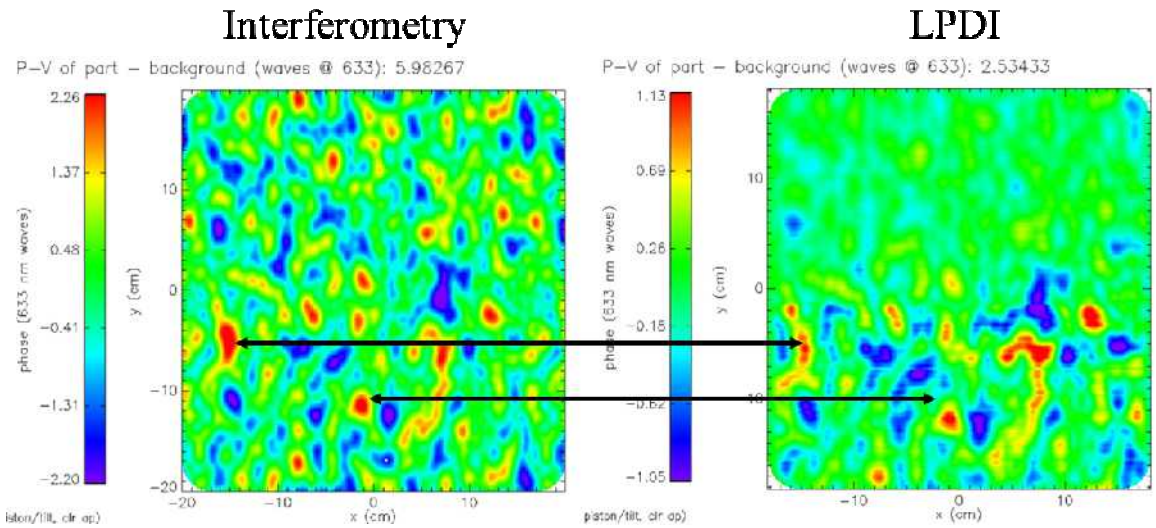

Figure 8.5: CPP phase maps as measured by Interferometry (left) and LPDI (right)

CHAPTER 9. CONCLUSION

In summary, screening of fratricidal phase objects on high-power laser optics is a challenging problem. We described a Linescan Phase Differential Imaging system that can detect phase objects in large-aperture optics in a single exposure. We compared LPDI to other types of phase object imaging systems. We developed an image simulation code for LPDI and described the optical physics behind it that can model LPDI's partially coherent illumination. We compared simulated LPDI images to measured images using two flaw sets consisting of fabricated fused silica Gaussian shaped surface bumps and FPOs found on production optics. We described a two-step production FPO screening process consisting of mapping flaws on the optic using the LPDI and FADLiB imaging diagnostics followed by characterization of their fratricide potential by measuring their transmitted amplitude and phase with PSDI.

In conclusion, the LPDI system offers many additional avenues to explore, for instance, developing a better understanding of its behavior and properties, quantitative image simulation, phase extraction, or use in other applications.

Appendix A Mathematics

Fourier transform

The variables x and ξ (y and η) are conjugate pairs in the spatial and frequency domains respectively, and $\mathbf{r} = [x,y]$ and $\boldsymbol{\rho} = [\xi, \eta]$ are conjugate vectors.

Forward Fourier transform $G(\boldsymbol{\rho}) = \mathbf{F}_{\mathbf{r}}\left\{g(\mathbf{r})\right\}_{\mathbf{r}\to\boldsymbol{\rho}} = \iint_{\infty} d\mathbf{r} g(\mathbf{r}) \exp[-2\pi i \mathbf{r}\cdot\boldsymbol{\rho}]$

Inverse Fourier transform $g(\mathbf{r}) = \mathbf{F}_{\boldsymbol{\rho}}^{-1}\left\{G(\boldsymbol{\rho})\right\}_{\boldsymbol{\rho}\to\mathbf{r}} = \iint_{\infty} d\boldsymbol{\rho} g(\boldsymbol{\rho}) \exp[2\pi i \mathbf{r}\cdot\boldsymbol{\rho}]$

Fourier shift theorem $\mathbf{F}_{\boldsymbol{\rho}}\left\{g(\mathbf{r})\exp[-2\pi i \mathbf{r}\cdot\boldsymbol{\rho}_s]\right\} = G(\boldsymbol{\rho}-\boldsymbol{\rho}_s)$

Derivation of Partially Incoherent Image Calculation (1D)

Reference: Yamazoe[72]

Dirac Bra-Kat notation is used in this derivation. A vector is constructed to represent the set of plane-waves that illuminates the object

$$\left|u_{pw}\right\rangle = [\exp(-2\pi i \xi_1 x) \quad \exp(-2\pi i \xi_2 x) \quad \ldots \quad \exp(-2\pi i \xi_N x)]^T \ .$$

These plane-waves are diffracted by the object as

$$\left|u_o\right\rangle = [t_x \exp(-2\pi i \xi_1 x) \quad t_x \exp(-2\pi i \xi_2 x) \quad \ldots \quad t_x \exp(-2\pi i \xi_N x)]^T ,$$

where T_ξ is the spatial frequency components (Fourier transform) of the object transmittance function. The pupil filters the transmitted plane-wave spectrum. For example, the pupil could be the 7 element vector (N=7)

$$\begin{array}{c} \mathrm{P} = (0 \quad 0 \quad 1 \quad 1 \quad 1 \quad 0 \quad 0) \\ \xi_i = (\xi_1 \quad \xi_2 \quad \xi_3 \quad \xi_4 \quad \xi_5 \quad \xi_6 \quad \xi_7) \end{array} .$$

Each index represents discrete frequency components x_i, where an element equal to 1 represents 100% transmission of the plane-wave amplitude at the indexed spatial

frequency. In the above example, indices 3,4,5 transmit while indices 1,2,6,7 block. The transmitted plane-waves (in the frequency domain) are filtered by the pupil

$$\left|U_{img}\right\rangle = \mathrm{P}\left|U_o\right\rangle.$$

Instead of the set of plane-waves frequency shifting the object, a set of shifted pupils (one for each point-source) will be used to calculate image irradiance. For example, image irradiance as filtered by pupil 1 is

$$E_1(x) \propto \mathbf{F}^{-1}\left\{\left\langle U_o\left|\mathsf{P}_1^{\dagger}\mathsf{P}_1\right|U_o\right\rangle\right\}, \text{ where } \mathsf{P}_1 = (0 \quad 0 \quad 1 \quad 1 \quad 1 \quad 0 \quad 0).$$

and the image irradiance as filtered by pupil 2 is

$$E_2(x) = \mathbf{F}^{-1}\left\{\left\langle U_o\left|\mathsf{P}_2^{\dagger}\mathsf{P}_2\right|U_o\right\rangle\right\}, \text{ where } \mathsf{P}_2 = (0 \quad 1 \quad 1 \quad 1 \quad 0 \quad 0 \quad 0).$$

Total image irradiance is then proportional to

$$E(x) \propto E_1(x) + E_2(x) = \mathbf{F}^{-1}\left\{\left\langle U_o\left|\mathsf{P}^{\dagger}\mathsf{P}\right|U_o\right\rangle\right\},$$

where P is the stacked shifted pupil matrix

$$\mathsf{P} = \begin{pmatrix} \mathsf{P}_1 \\ \mathsf{P}_2 \end{pmatrix} = \begin{pmatrix} 0 & 0 & 1 & 1 & 1 & 0 & 0 \\ 0 & 1 & 1 & 1 & 0 & 0 & 0 \end{pmatrix}.$$

Derivation of Partially Incoherent Image (2D)

Reference: Yamazoe[72]

The two-dimensional representation of the field transmitted through the object as illuminated by the plane-wave spectrum is

$$u_o(\boldsymbol{\rho}) = \begin{pmatrix} T_{\boldsymbol{\rho}}\exp[2\pi i(\xi_1 x+\eta_1 y)] & T_{\boldsymbol{\rho}}\exp[2\pi i(\xi_1 x+\eta_2 y)] & \cdots & T_{\boldsymbol{\rho}}\exp[2\pi i(\xi_1 x+\eta_M y)] \\ T_{\boldsymbol{\rho}}\exp[2\pi i(\xi_2 x+\eta_1 y)] & T_{\boldsymbol{\rho}}\exp[2\pi i(\xi_2 x+\eta_2 y)] & \cdots & T_{\boldsymbol{\rho}}\exp[2\pi i(\xi_2 x+\eta_M y)] \\ \vdots & & \ddots & \\ T_{\boldsymbol{\rho}}\exp[2\pi i(\xi_N x+\eta_1 y)] & T_{\boldsymbol{\rho}}\exp[2\pi i(\xi_N x+\eta_1 y)] & \cdots & T_{\boldsymbol{\rho}}\exp[2\pi i(\xi_N x+\eta_M y)] \end{pmatrix}.$$

This 2D matrix is reshaped into a 1D vector by reshaping operator **Y**

$$\left|U_o\right\rangle = \mathbf{Y}\left\{U_o(\xi,\eta)\right\}.$$

For example, the reshaping operator reshapes the 3x3 matrix A into a 1x9 vector

$$\mathbf{Y}\left\{\mathbf{A}\right\} = \mathbf{Y}\left\{\begin{pmatrix} a & b & c \\ d & e & f \\ g & h & i \end{pmatrix}\right\}^T = \begin{pmatrix} a & b & c & d & e & f & g & h & i \end{pmatrix}.$$

A two-dimensional pupil matrix can be written as

$$\mathbf{P}(\xi,\eta) = \begin{pmatrix} 0 & 0 & 0 & 0 & 0 & 0 & 0 \\ 0 & 0 & 0 & 0 & 0 & 0 & 0 \\ 0 & 0 & 1 & 1 & 1 & 0 & 0 \\ 0 & 0 & 1 & 1 & 1 & 0 & 0 \\ 0 & 0 & 1 & 1 & 1 & 0 & 0 \\ 0 & 0 & 0 & 0 & 0 & 0 & 0 \\ 0 & 0 & 0 & 0 & 0 & 0 & 0 \end{pmatrix}.$$

The pupil matrix is also reshaped into a 1D matrix by the reshaping operator

$$\mathsf{P}_1 = \mathbf{Y}\left\{\mathbf{P}(\xi,\eta)\right\}^T.$$

The 2D P-operator is then constructed as a stacked set of shifted pupils of dimension $N\,x\,M^2$

$$\mathsf{P} = \begin{pmatrix} \mathbf{Y}\left\{\mathbf{P}(\xi-\xi_1,\eta-\eta_1)\right\}^T \\ \mathbf{Y}\left\{\mathbf{P}(\xi-\xi_2,\eta-\eta_2)\right\}^T \\ \vdots \\ \mathbf{Y}\left\{\mathbf{P}(\xi-\xi_{Ns},\eta-\eta_{Ns})\right\}^T \end{pmatrix} = \begin{pmatrix} \mathsf{P}_1 \\ \mathsf{P}_2 \\ \vdots \\ \mathsf{P}_{Ns} \end{pmatrix},$$

where Ns is the number of point-sources, each producing plane-waves (or pupil shifts) of frequency x_j and h_j.

C-4: Reduction by SVD

A Singular Value Decomposition (SVD) of P takes the form

$$\mathsf{P} = \mathbf{U}\mathbf{A}\mathbf{V}^{\dagger},$$

where **U** and **V** are unitary matrices (i.e. $\mathbf{U}\mathbf{U}^{\dagger} = \mathbf{I}$) and **A** is a diagonal matrix with real and positive elements. The diagonal elements are the Eigenvalues. Substitution of the SVD of the P-operator into the irradiance operator yields

$$\langle U_o | \mathsf{P}^{\dagger}\mathsf{P} | U_o \rangle = \langle U_o | (\mathbf{U}\mathbf{A}\mathbf{V}^{\dagger})^{\dagger}\mathbf{U}\mathbf{A}\mathbf{V}^{\dagger} | U_o \rangle .$$

Following simplification the image irradiance is proportional to

$$E(\mathbf{r}') \propto \mathsf{F}_{\boldsymbol{\rho}}^{-1}\left\{ \langle U_o | \mathbf{V}\mathbf{A}^2\mathbf{V}^{\dagger} | U_o \rangle \right\}.$$

Finally, the image is computed using the sum of the eigenmatrix terms

$$E(\mathbf{r}') \propto \sum_{j=1}^{N} \mu_j^2 \left| \mathsf{F}_{\boldsymbol{\rho}}^{-1}\left\{ T_{obj}(\boldsymbol{\rho})\Phi_j(\boldsymbol{\rho}) \right\} \right|^2,$$

where the eigenvalues and the eigenmatricies are

$$\mu_j = \mathbf{A}_{j,j} \text{ and}$$

$$\Phi_j(\boldsymbol{\rho}) = \mathbf{Y}\left\{ \left(\mathbf{V}_j^{\dagger} \right)^T \right\}.$$

Appendix B MATLAB™ Code

Select portion of the LPDI image simulation code:

```
%Continuous source distribution parameters
    xis0 = xs0/zs/lm;                %Center x spatial frequency (pixel)
    pxis0 = xis0/dxi;                %Center x spatial frequency (pixel)
    xismin = (xs0-wx/2)/zs/lm;       %Min source x spatial frequency
    xismax = (xs0+wx/2)/zs/lm;       %Max source x spatial frequency
    yismax = N/2*dyi;                %Use for infinite extent along y
    yismin = -N/2*dyi;               %Use for infinite extent along y
%Generate source distribution (pixel coordinates)
    %Sample continuous source distribution in frequency space
    [xis,yis] = getlight(xi,yi,xismax,xismin,yismax,yismin,Ns);
    pxis = xis/dxi;        %Shift x-coordinate (pixels)
    pyis = yis/dyi;        %Shift y-coordinate (pixels)

%Stack the pupils
    P = logical([]);    %Initialize P-operator as binary matrix
    for j=1:Ns
       Pj = circshift(H,[round(pxis(j)) round(pyis(j))]);
       Pj = transpose(reshape(transpose(Pj),N^2,1));
       P = [P; Pj];
    end

%Perform SVD on P
    [U,L,V] = svd(single(P),'econ');  %Perform SVD of P-operator
    phi = diag(L);                   %Diagonal of L are  the eigenvalues
    Vdag = V';                       %Complex conjugate transpose of V
%Get eigen-matricies
        psi(:,:,j) = reshape(transpose(Vdag(j,:)),N,N);
%Generate object field
    u_obj = exp(2*pi*i*f/lm/1e6);   %f is in nanometers

%Compute image using eigenvalues and eigenvectors
    I = zeros(N,N); %Initialize irradiance array
  for j = 1:Neig
    Ij = phi(j)^2*abs(fftshift(ifft2(fftshift(U_obj.*psi(:,:,j))))).^2;
    I = Ij + I; %Build-up image irradiance one eigenterm at a time
  end

%Apply CCD blur
    g = linescan(x*-m,y*-m,I,px);   %Apply linescan image blur
%Sample simulated image, e.g. with CCD
    px_obj = px/abs(m);              %Pixel size at object plane
    scale = dx/px_obj;               %Scale to use to sample the
simulated image
    bin = round(1/scale);
    scale = 1/bin/scale;
    g_samp = blkproc(g,[bin bin],'mean2');
    g_samp = imresize(g_samp, scale,'box');  %Resample image
```

Appendix C Gaussian Bump Fabrication

Description of LVCD deposition process provided by Selim Elhjad:

A cw-CO_2 laser (λ=10.6 μm) is used to heat the surface to locally deposit silica from the pyrolitic decomposition of the silica TEOS gas phase precursor at ~1100K (Desu 1989)[76]. The source of the precursor is a bubbler containing liquid TEOS with a vapor pressure of ~0.3% at room temperature (Vanderdis 1993)[77]. TEOS gas precursor is then brought to the surface dispersed in an air carrier gas as an impinging jet from a Nozzle co-incident with the CO_2 laser beam heating. Deposition conditions were fixed for all sites except for the deposition times, which varied from 30 sec up to 10 min per site depending on the size of the bump desired, while the height of the sites were monitored in real time by PSDI interferometry during LCVD deposition. After deposition, the sites molecular structure and composition were characterized using confocal μRaman spectroscopy to determine the quality of the silica deposited, which had Raman spectra nearly indistinguishable from the surrounding silica substrate (data not shown). Further dimensional characterization was made for each site with a laser confocal microscope to derive 3D height and shape profiles. Because the decomposition of TEOS is thermally activated, the deposition profile will track the nearly Gaussian temperature profile to produce Gaussian deposition shapes in the temperature regime where the decomposition kinetics are much slower than mass transport (Han 1994)[78].

Appendix D First LPDI Image

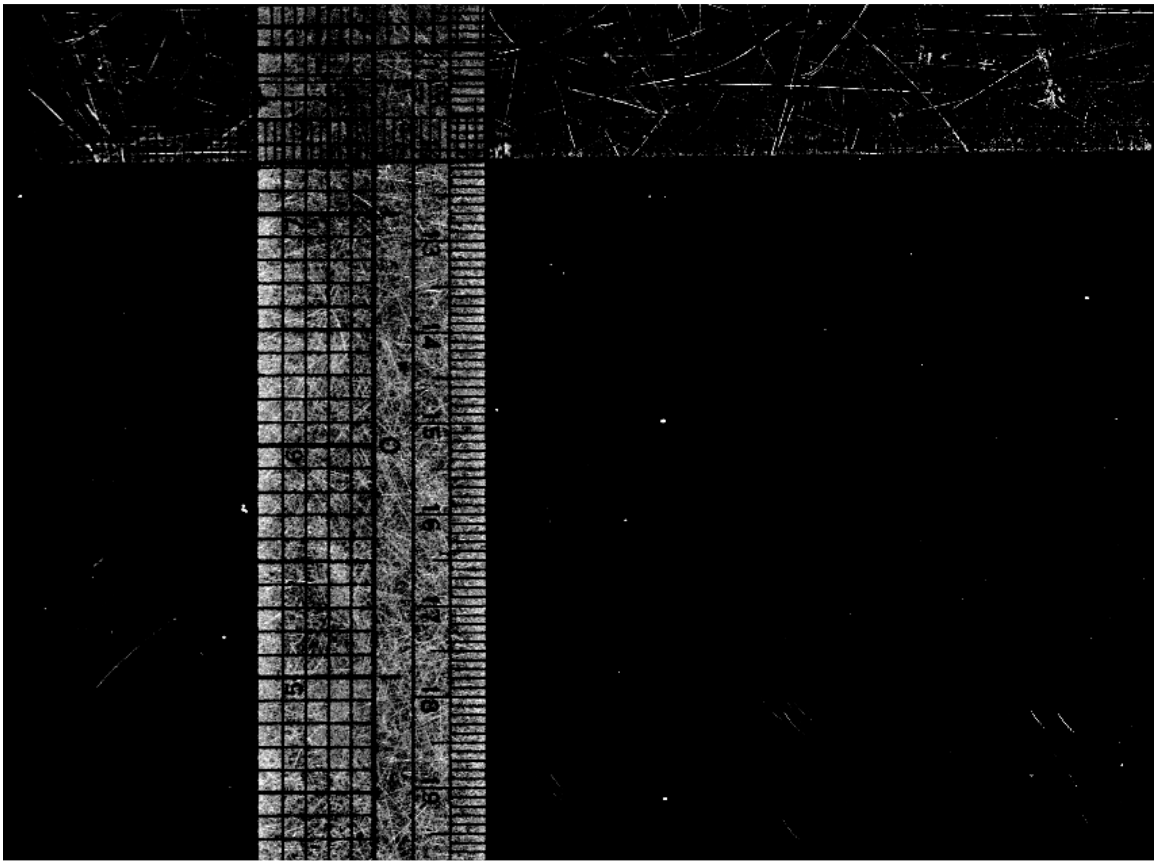

First LPDI image of a pair of transparent plastic rulers

References

1. Runkel, M., et al., *A system for measuring defect induced beam modulation on inertial confinement fusion-class laser optics - art. no. 59912H.* Laser-Induced Damage in Optical Materials: 2005, 2005. **5991**: p. H9912-H9912.
2. Matthews, M.J., et al., *Downstream intensification effects associated with CO2 laser mitigation of fused silica - art. no. 67200A.* Laser-Induced Damage in Optical Materials: 2007, 2008. **6720**: p. A7200-A7200.
3. Schmidt, J.R., et al., *Scattering-induced downstream beam modulation by plasma scalded mirrors - art. no. 67201H.* Laser-Induced Damage in Optical Materials: 2007, 2008. **6720**: p. H7201-H7201.
4. Honig, J., et al., *Experimental study of 351-nm and 527-nm laser-initiated surface damage on fused silica surfaces due to typical contaminants.* Laser-Induced Damage In Optical Materials: 2004, 2005. **5647**: p. 129-135.
5. Nostrand, M.C., et al., *A large aperture, high energy laser system for optics and optical component testing.* Laser-Induced Damage in Optical Materials: 2003, 2003. **5273**: p. 325-333.
6. Norton, M.A., et al., *Growth of laser initiated damage in fused silica at 351 nm.* Laser-Induced Damage in Optical Materials: 2000, Proceedings, 2001. **4347**: p. 468-468.
7. Negres, R.A., et al., *Growth behavior of laser-induced damage on fused silica optics under UV, ns laser irradiation.* Optics Express, 2010. **18**(19): p. 19966-19976.
8. Liao, Z.M., et al., *Predictive modeling techniques for nanosecond-laser damage growth in fused silica optics.* Optics Express, 2012. **20**(14): p. 15569-15579.
9. Hunt, J.T., K.R. Manes, and P.A. Renard, *Hot Images from Obscurations.* Applied Optics, 1993. **32**(30): p. 5973-5982.
10. Widmayer, C.C., M.R. Nickels, and D. Milam, *Nonlinear holographic imaging of phase errors.* Applied Optics, 1998. **37**(21): p. 4801-4805.
11. Conder, A., et al., *Final optics damage inspection (FODI) for the national ignition facility - art. no. 672010.* Laser-Induced Damage in Optical Materials: 2007, 2008. **6720**: p. 72010-72010.
12. Conder, A., et al., *Final Optics Damage Inspection (FODI) for the National Ignition Facility.* Optics and Photonics for Information Processing Iv, 2010. **7797**.
13. Nostrand, M.C., et al., *Identification and elimination of fluorescent surface-damage precursors on DKDP optics.* Laser-Induced Damage in Optical Materials: 2002 and 7th International Workshop on Laser Beam and Optics Characterization, 2002. **4932**: p. 192-201.
14. Carr, C.W., et al., *Techniques for qualitative and quantitative measurement of aspects of laser-induced damage important for laser beam propagation.* Measurement Science & Technology, 2006. **17**(7): p. 1958-1962.
15. Demos, S.G., et al., *Investigation of fluorescence microscopy as a tool for noninvasive detection and imaging of damage precursors at 351-nm.* Laser-Induced Damage in Optical Materials: 2001 Proceedings, 2002. **4679**: p. 347-359.

16. Adams, J.J., et al., *Results of applying a non-evaporative mitigation technique to laser-initiated surface damage on fused-silica.* Laser-Induced Damage in Optical Materials: 2010, 2010. **7842**.
17. Bass, I.L., et al., *An Improved Method of Mitigating Laser Induced Surface Damage Growth in Fused Silica Using a Rastered, Pulsed CO2 Laser.* Laser-Induced Damage in Optical Materials: 2010, 2010. **7842**.
18. Monticelli, M.V., et al. *The HMDS coating flaw removal tool*. 2008.
19. Heebner, J., et al., *Programmable Beam Spatial Shaping System for the National Ignition Facility.* High Power Lasers for Fusion Research, 2011. **7916**.
20. Haynam, C.A., et al., *The National Ignition Facility: Status and Performance of the World's Largest Laser System for the High Energy Density and Inertial Confinement Fusion.* 2008 Conference on Lasers and Electro-Optics & Quantum Electronics and Laser Science Conference, Vols 1-9, 2008: p. 204-205.
21. Wegner, P., et al., *NIF final optics system: frequency conversion and beam conditioning.* Optical Engineering at the Lawrence Livermore National Laboratory Ii: The National Ignition Facility, 2004. **5341**: p. 180-189.
22. Ravizza, F.L., et al. *Process for rapid detection of fratricidal defects on optics using linescan phase-differential imaging.* 2009.
23. Schardin, H., *Toepler's streak method.* Deutsche Medizinische Wochenschrift, 1934. **78**: p. 1351-1352.
24. Zernike, F., *How I Discovered Phase Contrast.* Science, 1955. **121**(3141): p. 345-349.
25. Zernike, F., *Phase contrast, a new method for the microsopic observation of transparent objects.* Physica, 1942. **9**: p. 686-698.
26. Zernike, F., *Phase contrast, a new method for the microscopic observation of transparent objects Part II.* Physica, 1942. **9**: p. 974-986.
27. *The Nobel Prize in Physics 1953*. 1953; Available from: http://www.nobelprize.org/nobel_prizes/physics/laureates/1953/.
28. Ockenga, W. *Phase Contrast*. 2011; Available from: http://www.leica-microsystems.com/science-lab/phase-contrast/.
29. Hoffman, R. and L. Gross, *Modulation Contrast Microscope.* Applied Optics, 1975. **14**(5): p. 1169-1176.
30. Nomarski, G., *New Theory of Image Formation in Differential Interference Microscopy (Dim).* Journal of the Optical Society of America, 1969. **59**(11): p. 1524-&.
31. Nostrand, M.C., et al., *Correlation of laser-induced damage to phase objects in bulk fused silica.* Laser-Induced Damage In Optical Materials: 2004, 2005. **5647**: p. 233-246.
32. Matthews, M.J., et al., *Phase modulation and morphological evolution associated with surface-bound particle ablation.* Journal of the Optical Society of America B, 2013. **30**(12): p. 3233-3242.
33. J. Folta, M.N., J. Honig, N. Wong, F. Ravizza, P. Geraghty, M. Taranowski, G. Johnson, G. Larkin, D. Ravizza, J. Peterson, B. Welday, P. Wegner, *Mitigation of*

Laser Damage on National Ignition Facility Optics in Volume Production. Proc. SPIE, 2013. **8885**.

34. R.A. Sacks, M.A.H., S.W. Haney, and J.B. Trenholme, *The PROP92 Fourier beam propagation code.* ICF Annual Report. **UCRL-LR-105821-96**.
35. M. Nostrand, C.W., M. Johnson, K. Manes, *Prop-based flaw specifications for FOA optics using the damage initiation integral and a bulk intensification limit.* 2007.
36. Widmayer, C.C., D. Milam, and S.P. deSzoeke, *Nonlinear formation of holographic images of obscurations in laser beams.* Applied Optics, 1997. **36**(36): p. 9342-9347.
37. Soileau, M.J., et al., *Laser-Induced Damage and the Role of Self-Focusing.* Optical Engineering, 1989. **28**(10): p. 1133-1144.
38. Carr, C.W., J.B. Trenholme, and M.L. Spaeth, *Effect of temporal pulse shape on optical damage.* Applied Physics Letters, 2007. **90**(4).
39. Trenholme, J.B., *Damage from pulses with arbitrary temporal shapes*, in *LLNL internal memo, LST-LMO 94-001 (L-18179-2)*. 1995.
40. Lindl, J., *Development of the indirect-drive approach to inertial confinement fusion and the target physics basis for ignition and gain.* Physics of Plasmas (1994-present), 1995. **2**(11): p. 3933-4024.
41. Heebner, J., et al., *A Programmable Beam Shaping System for Tailoring the Profile of High Fluence Laser Beams.* Laser-Induced Damage in Optical Materials: 2010, 2010. **7842**.
42. Greivenkamp, J.E., *Field guide to geometrical optics*. SPIE field guides. 2004, Bellingham, Wash.: SPIE Press. xii, 117 p.
43. Kingslake, R., *A history of the photographic lens*. 1989, Boston: Academic Press. xi, 334 p.
44. TrueSense Imaging, I. *TrueSense Imaging, Inc.*; Available from: http://www.truesenseimaging.com/.
45. Better Light, I. *Better Light, Inc.*; Available from: http://www.betterlight.com/.
46. TrueSense , I. *TrueSense KLI-8023 Datasheet*. 2013; Available from: http://www.truesenseimaging.com/all/download/file?fid=8.68.
47. Schott. *Schott Lightline Data Sheet*. 2013; Available from: http://www.us.schott.com/lightingimaging/english/download/04.27.09_lightlines_us.qxd.pdf.
48. Schott. *Schott DCRIII*. 2013; Available from: http://www.us.schott.com/lightingimaging/english/download/04.21.09_dcr_iii_plus_us.qxd.pdf.
49. Kegelmeyer, L.M., et al., *Local area signal-to-noise ratio (LASNR) algorithm for image segmentation - art. no. 66962H.* Applications of Digital Image Processing Xxx, Pts 1 and 2, 2007. **6696**: p. H6962-H6962.
50. Suratwala, T.I., et al., *HF-Based Etching Processes for Improving Laser Damage Resistance of Fused Silica Optical Surfaces.* Journal of the American Ceramic Society, 2011. **94**(2): p. 416-428.

51. Smartt, R.N. and J. Strong, *Point-Diffraction Interferometer.* Journal of the Optical Society of America, 1972. **62**(5): p. 737-&.
52. Smartt, R.N. and W.H. Steel, *Theory and Application of Point-Diffraction Interferometers.* Japanese Journal of Applied Physics, 1975. **14**: p. 351-356.
53. Sommargren, G.E., et al., *100-picometer interferometry for EUVL.* Emerging Lithographic Technologies Vi, Pts 1 and 2, 2002. **4688**: p. 316-328.
54. Phillion, D.W., *General methods for generating phase-shifting interferometry algorithms.* Applied Optics, 1997. **36**(31): p. 8098-8115.
55. Maxwell, J.C., *A Dynamical Theory of the Electromagnetic Field.* Philosophical Transactions of the Royal Society of London, 1865. **155**: p. 459-512.
56. Ulaby, F.T., *Fundamentals of applied electromagnetics*. 2004 Media ed. 2004, Upper Saddle River, NJ: Pearson. xviii, 433 p.
57. Inan, U.S. and A.S. Inan, *Electromagnetic waves*. 2000, Upper Saddle River, N.J.: Prentice Hall. xv, 507, 49 p.
58. Halliday, D., R. Resnick, and J. Walker, *Fundamentals of physics, 6/E CD-physics 3.0*. 2001, Wiley,: New York. p. 1 computer optical disc 4 3/4 in. + 1 user's guide.
59. Milster, T.D., *Diffraction and Interferometry Class Notes*. 2012.
60. Weisstein, E.W. *Phasor*. 2013; Available from: http://mathworld.wolfram.com/Phasor.html.
61. Born, M. and E. Wolf, *Principles of optics : electromagnetic theory of propagation, interference and diffraction of light*. 6th (corr.) ed. 1997, Cambridge, UK ; New York ;: Cambridge University Press. xxviii, 808 p.
62. Goodman, J.W., *Introduction to Fourier optics*. 3rd ed. 2005, Englewood, Colo.: Roberts & Co. xviii, 491 p.
63. Goodman, J.W., *Statistical optics*. Wiley classics library ed. Wiley classics library. 2000, New York: Wiley. xvii, 550 p.
64. Zernike, F., *The concept of degree of coherence and its application to optical problems.* Physica, 1938. **5**: p. 785-795.
65. Hopkins, H.H., *The Concept of Partial Coherence in Optics.* Proceedings of the Royal Society of London Series a-Mathematical and Physical Sciences, 1951. **208**(1093): p. 263-277.
66. Yamazoe, K., *Two models for partially coherent imaging.* Journal of the Optical Society of America a-Optics Image Science and Vision, 2012. **29**(12): p. 2591-2597.
67. Köhler, A., *Ein neues Beleuchtungsverfahren für mikrophotographische Zwecke.* Zeitschrift für wissenschaftliche Mikroskopie und für Mikroskopische Technik, 1893. **10**(4): p. 433-440.
68. Koehler, A., *New Method of Illimination for Phomicrographical Purposes.* Journal of the Royal Microscopical Society, 1894. **14**: p. 261-262.
69. Barrett, H.H. and K.J. Myers, *Foundations of image science*. Wiley series in pure and applied optics. 2004, Hoboken, NJ: Wiley-Interscience. xli, 1540 p.

70. Born, M. and E. Wolf, *Principles of optics : electromagnetic theory of propagation, interference and diffraction of light*. 7th expanded ed. 1999, Cambridge ; New York: Cambridge University Press. xxxiii, 952 p.
71. The Mathworks, I. *Mathworks*. 2013; Available from: http://www.mathworks.com/products/matlab/.
72. Yamazoe, K., *Computation theory of partially coherent imaging by stacked pupil shift matrix.* Journal of the Optical Society of America a-Optics Image Science and Vision, 2008. **25**(12): p. 3111-3119.
73. Mathworld. *Signular Value Decomposition*. 2013; Available from: http://mathworld.wolfram.com/SingularValueDecomposition.html.
74. Mathworks. *Singular Value Decomposition*. 2013; Available from: http://www.mathworks.com/help/matlab/ref/svd.html.
75. Menapace, J.A., et al., *MRF applications: On the road to making large-aperture ultraviolet laser resistant continuous phase plates for high-power lasers - art. no. 64030N.* Laser-Induced Damage in Optical Materials: 2006, 2007. **6403**: p. N4030-N4030.
76. Desu, S.B., *Decomposition Chemistry of Tetraethoxysilane.* Journal of the American Ceramic Society, 1989. **72**(9): p. 1615-1621.
77. Vandervis, M.G.M., E.H.P. Cordfunke, and R.J.M. Konings, *The Thermodynamic Properties of Tetraethoxysilane (Teos) and an Infrared Study of Its Thermal-Decomposition.* Journal De Physique Iv, 1993. **3**(C3): p. 75-82.
78. Han, J.S. and K.F. Jensen, *Combined Experimental and Modeling Studies of Laser-Assisted Chemical-Vapor-Deposition of Copper from Copper(I)-Hexafluoroacetylacetonate Trimethylvinylsilane.* Journal of Applied Physics, 1994. **75**(4): p. 2240-2250.